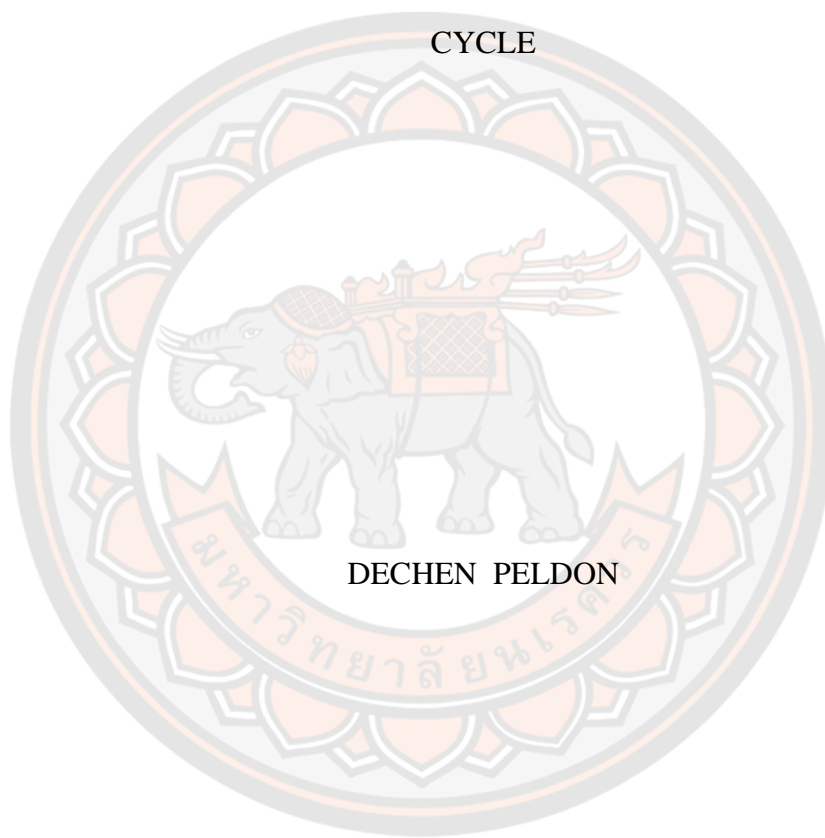




THE STUDY OF SPACE WEATHER AT THE BEGINNING OF THE 25TH SOLAR
CYCLE



A Thesis Submitted to the Graduate School of Naresuan University
in Partial Fulfillment of the Requirements
for the Master of Science in Physics
2022
Copyright by Naresuan University

THE STUDY OF SPACE WEATHER AT THE BEGINNING OF THE 25TH SOLAR
CYCLE



A Thesis Submitted to the Graduate School of Naresuan University
in Partial Fulfillment of the Requirements
for the Master of Science in Physics
2022
Copyright by Naresuan University

Thesis entitled "The study of space weather at the beginning of the 25th solar cycle"
By Dechen Peldon
has been approved by the Graduate School as partial fulfillment of the requirements
for the Master of Science in Physics of Naresuan University

Oral Defense Committee

..... Chair
(Assistant Professor Charuangrit Channok, Ph.D.)

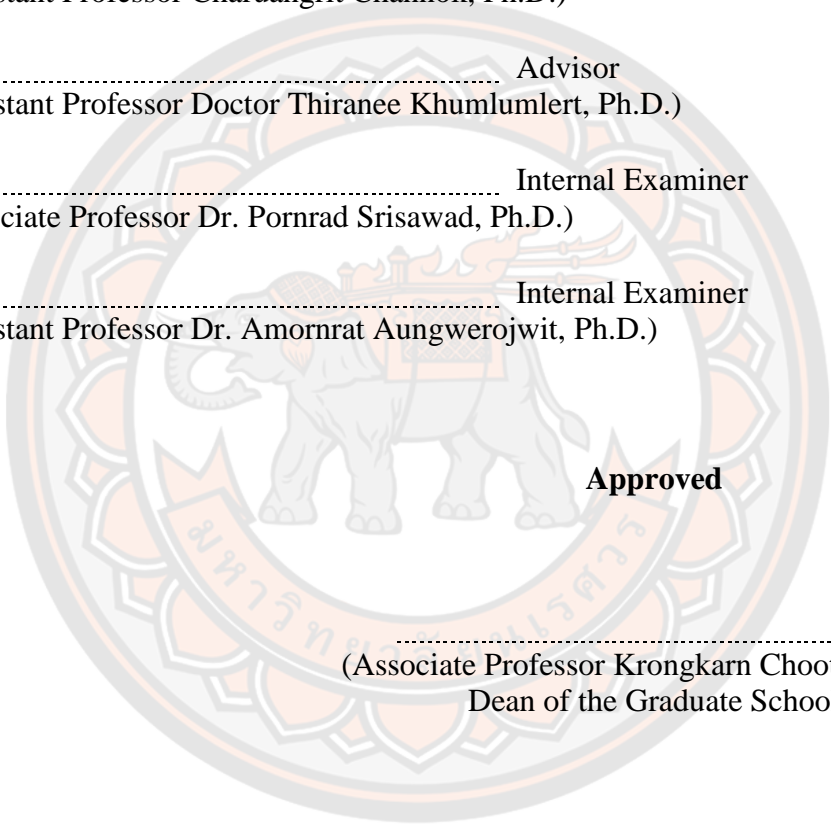
..... Advisor
(Assistant Professor Doctor Thiranee Khumlumlert, Ph.D.)

..... Internal Examiner
(Associate Professor Dr. Pornrad Srisawad, Ph.D.)

..... Internal Examiner
(Assistant Professor Dr. Amornrat Aungwerojwit, Ph.D.)

Approved

.....
(Associate Professor Krongkarn Chootip, Ph.D.)
Dean of the Graduate School



Title	THE STUDY OF SPACE WEATHER AT THE BEGINNING OF THE 25 TH SOLAR CYCLE
Author	Dechen Peldon
Advisor	Assistant Professor Doctor Thiranee Khumlumlert, Ph.D.
Academic Paper	M.S. Thesis in Physics, Naresuan University, 2022
Keywords	Space Weather Solar Cycle Coronal Mass Ejection (CME) Solar Flares Solar Energetic Particles (SEPs) Advanced Composition Explorer (ACE) spacecraft

ABSTRACT

The Sun is the primary driver of space weather, and on occasion, it can produce material eruptions accompanied by solar energetic particles and bursts of electromagnetic radiation (SEPs). This research studied the space weather at the beginning of the 25th solar cycle and its physical characteristics, including the eruptions on the Sun's surface, by analyzing the motion of high-energy particles from the Sun using the distribution data obtained from the Advanced Composition Explorer. The propagation of SEPs was studied using Ruffolo's transport equation, which was solved using the finite difference method. To locate the best solutions, we employed piecewise linear least-square fitting. Further, we examined the results in relation to the space environment by comparing the simulated solar flare injection time and the X-ray injection on the Sun. This study focuses on the two most potent solar events, M4.4 on 29 November 2020 and X1.59 on 3 July 2021. Higher X-ray intensity solar flares (X1.59) have a longer mean free path and arrive at Earth more quickly than solar flares with lower X-ray intensity (M4.4), which have a shorter mean free path and take longer to arrive at Earth. Because the simulation's injection time is far longer than the actual injection time on the Sun, the particles are weaker and have no impact on Earth. Although both events generated CMEs, there was no impact on Earth due to the eruption's location. The Kp-index for both events was no higher than two. Despite the fact that M-class and X-class solar flares erupted at the beginning of the 25th solar cycle, the eruption's location and timing resulted in modest space weather with little impact on Earth.



ACKNOWLEDGEMENTS

First and foremost, I would like to express my sincere gratitude to my advisor Asst. Prof. Dr. Thiranee Khumlumlert for the continuous support of my master's degree study and research, for her patience, motivation, enthusiasm, and immense knowledge. Her guidance helped me during my research and writing of this thesis. Her dynamism and sincerity deeply inspired me. She has taught me the methodology to carry out the research and to present the research works as clearly as possible. I could not have imagined having a better advisor and mentor for my study. I would also like to thank her for her friendship and empathy.

I am incredibly grateful to the Thailand International Cooperation Agency (TICA) and the Royal Government of Bhutan for their timely assistance and direction throughout the research process. Professor Dr. David Ruffolo, Department of Physics, Mahidol University, is to be thanked for the transport equation and programming used in this study. Furthermore, I would like to express my gratitude to the faculty of Naresuan University's Department of Physics for their invaluable assistance and encouragement.

Finally, I would like to thank my parents for their love, prayers, care, and sacrifices in educating and preparing me for my future. I am very thankful to my husband and daughter for their love, understanding, prayers, and continuing support in completing this study. Also, I express my thanks to my sisters, brother, sister-in-law, and brothers-in-law for their support and valuable prayers. My special thanks go to my friends for their keen interest in successfully completing this thesis.

Dechen Peldon

TABLE OF CONTENTS

	Page
ABSTRACT.....	C
ACKNOWLEDGEMENTS.....	E
TABLE OF CONTENTS.....	F
LIST OF TABLES.....	I
LIST OF FIGURES.....	J
CHAPTER I INTRODUCTION.....	1
1.1 Importance and background.....	1
1.2 Purpose of the Study.....	2
1.3 Scope of the Study.....	3
CHAPTER II LITERATURE REVIEW.....	5
2.1 The Structure of the Sun.....	5
2.1.1 Internal Structure of the Sun.....	5
2.1.1.1 Core.....	5
2.1.1.2 The Radiative zone.....	6
2.1.1.3 The Convective zone.....	6
2.1.2 The Atmosphere of the Sun.....	7
2.1.2.1 The Photosphere.....	7
2.1.2.2 The Chromosphere.....	7
2.1.2.3 The Corona.....	7
2.2 The Solar Cycle.....	8
2.3 The Space Weather.....	9
2.4 The Solar Flare.....	10
2.4.1 The Classification of solar flares.....	11
2.4.1.1 Impulsive Solar Flares.....	12
2.4.1.2 Gradual Solar Flares.....	12

2.5 The Coronal Mass Ejection	15
2.6 The Solar Wind.....	17
2.7 The Solar Energetic Particles.....	19
2.8 The Interplanetary Magnetic Field	20
2.9 Impact of Space Weather.....	20
2.10 The Advanced Composition Explorer Spacecraft	21
2.11 The Archimedean Spiral	25
2.12 Data analysis of solar eruption's high-energy particles	29
2.13 The Transport equation.....	30
CHAPTER III RESEARCH METHODOLOGY	51
3.1 Research Tools.....	51
3.1.1 The Data from the ACE spacecraft	51
3.1.2 Ruffolo's transport equation to simulate particle motion in a C program.....	51
3.2 The Numerical methods used in this research	53
3.2.1 The Explicit method	54
3.2.2 The Implicit methods.....	56
3.2.3 The Crank-Nicolson method	57
3.3 Selecting an event at the beginning of the 25 th solar cycle.....	59
3.4 Kp-index on the selected events	62
3.5 The collection of Data from ACE spacecraft through SIS instrument	64
3.6 Preparation of spacecraft data for simulation in the C program	68
3.6.1 Calculating errors in the data obtained from the spacecraft.....	70
3.6.2 Determination of the variables required for particle motion simulation ..	72
3.7 Simulation of motion of high-energy particle	76
3.8 Fitting data to compare	77
3.9 Determination of Injection Time	78
3.10 Space condition at the beginning of the 25 th solar cycle (in 2020 and 2021).....	81
CHAPTER IV RESULTS AND DISCUSSION.....	84
4.1 The simulation result of the propagation of SEPs	84

4.2 Simulation of the particle distribution over time using the best mean free path	85
4.3 Fitting comparison of simulation results and spacecraft data.....	86
CHAPTER V CONCLUSION.....	95
5.1 Discussion.....	95
5.2 Conclusion	98
REFERENCES	99
APPENDIX.....	111
APPENDIX A SPECTRUM GRAPH OF THE PARTICLES	112
APPENDIX B PARTICLE DENSITY AND TIME VALUE GRAPHS FOR THE 29 NOVEMBER 2020 EVENT FOR THE DATA COLLECTED FROM THE SPACECRAFT	113
APPENDIX C INTENSE GRAPH FROM THE SIMULATION OF THE DATA OF 29 NOVEMBER 2020 EVENT	114
APPENDIX D COMPARE GRAPH FOR THE 29 NOVEMBER 2020 EVENT	118
APPENDIX E GRAPH TO CALCULATE BEST MEAN FREE PATH OF THE ELEMENTS OF ALL ENERGY LEVELS OF 29 NOVEMBER 2020 EVENT	121
APPENDIX F GRAPH TO CALCULATE INJECTION TIME USING FWHM OF THE PARTICLES OF 29 NOVEMBER 20202 EVENT	122
APPENDIX G PARTICLE DENSITY AND TIME VALUE GRAPHS FOR THE 3 JULY 2021 EVENT FOR THE DATA COLLECTED FROM THE SPACECRAFT.....	123
APPENDIX H INTENSE GRAPH FROM THE SIMULATION OF THE DATA OF 3 JULY 2021 EVENT	124
APPENDIX I COMPARE GRAPH FOR THE 3 JULY 2021 EVENT	129
APPENDIX J GRAPH TO CALCULATE BEST MEAN FREE PATH OF THE ELEMENTS OF ALL ENERGY LEVELS 3 JULY 2021 EVENT	132
APPENDIX K GRAPH TO CALCULATE INJECTION TIME USING FWHM OF THE PARTICLES OF 3 JULY 2021 EVENT	133
BIOGRAPHY	134

LIST OF TABLES

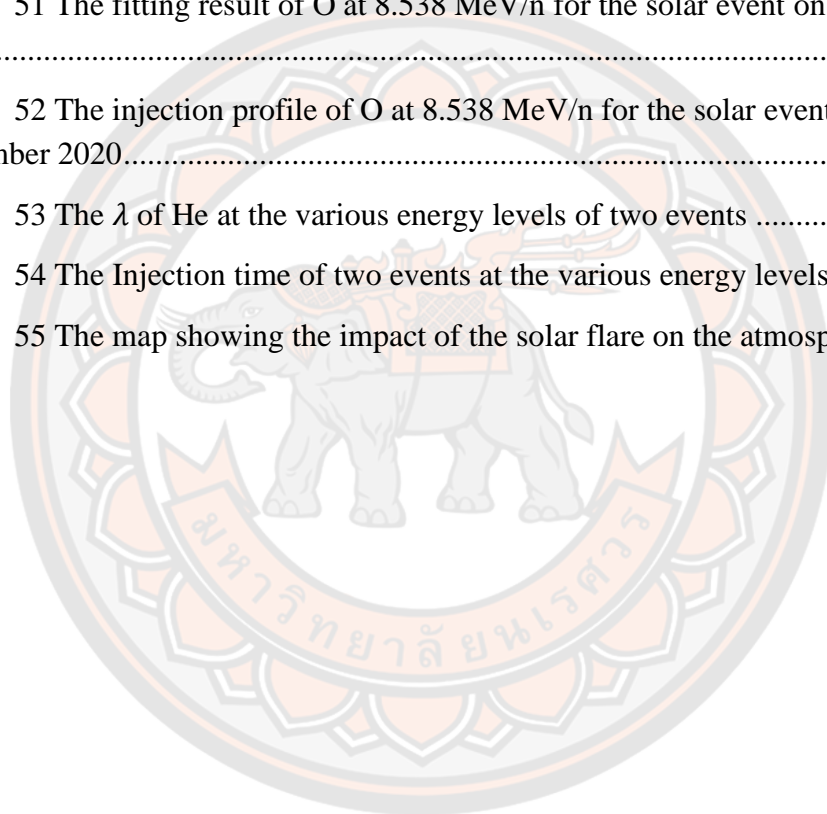
	Page
Table 1 Displays a Research Plan.....	4
Table 2 The Classification of solar flares at different intensities	14
Table 3 Description of terms in the transport equation.....	50
Table 4 The Physical characteristics of the event on 29 November 2020	59
Table 5 The Physical characteristics of the event on 3 July 2021	60
Table 6 Data sample collected for Helium particles at all energy levels.....	69
Table 7 Data samples for helium particles at 4.032 MeV/n energy level.....	70
Table 8 Helium's average energy value	72
Table 9 The values used in the He data preparation process	76
Table 10 The injection profile obtained from the ubuntu operating system of He1 released on 29 November 2020.....	79
Table 11 The potential impact of solar activity on the Kp-index	83
Table 12 The helium and oxygen simulation results of two different events.....	93

LIST OF FIGURES

	Page
Figure 1 Structure of the Sun	5
Figure 2 The current solar cycle	9
Figure 3 Showing solar flare eruption on 29 November 2020	12
Figure 4 Shows a series of solar flares as detected by NOAA satellites in July 2000	13
Figure 5 Shows how CME travels from Sun toward Earth	16
Figure 6 Showing solar radiation storm.....	17
Figure 7 Showing formation of auroras due to solar wind	19
Figure 8 The Line Drawing of Advanced Composition Explorer (ACE) Spacecraft.	22
Figure 9 The unit vectors in Spherical coordinates	25
Figure 10 Shows spherical coordinates of the properties of the magnetic field emitted by the Sun	27
Figure 11 Early phase of diffusion Figure 12 Later phase of diffusion.....	29
Figure 13 Examples of high-energy particle mean free paths that can move before scattering due to shifting magnetic field lines, with particle A having a shorter mean free path than particle B	30
Figure 14 The Systematic flux conduction Figure 15 The Random flux conduction.....	31
Figure 16 Shows the pitch angle θ between the direction of the magnetic field line and the particle's velocity.....	32
Figure 17 The Stationary reference frame Figure 18 The solar wind reference frame	34
Figure 19 The properties of magnetic field lines	35
Figure 20 The relationship between parallel and perpendicular velocity in reference to magnetic field lines	38
Figure 21 The magnetic field acting on the Sun's radial line.....	40
Figure 22 The flow of particles through cells	53
Figure 23 The solar eruption on 29 November 2020	60
Figure 24 The solar eruption on 3 July 2021	61

Figure 25 X-ray severity values on 29 November 2020	62
Figure 26 X-ray severity values on 3 November 2021	63
Figure 27 Kp index on 29 November 2020 as detected by NOAA GOES satellite ...	64
Figure 28 Kp index on 3 July 2021 as detected by NOAA GOES satellite.....	64
Figure 29 The home page of the website	65
Figure 30 The webpage to get the main data	65
Figure 31 The type of data selection	66
Figure 32 The DoY of the selected event (29/11/2020)	67
Figure 33 A web page showing selected elements and their counts.....	68
Figure 34 Sample of Helium particle distribution chart at 4.032 MeV/n energy level	71
Figure 35 A Helium sample graph illustrating the relationship between momentum log values and spectral spectra of occurrences on 29 November 2020.	75
Figure 36 The relationship between χ^2 and the mean free path (λ).....	78
Figure 37 The helium release triangle with an energy level of 4.032 MeV/n	78
Figure 38 The kp-index value on 27-30 November 2020.....	82
Figure 39 The simulation results of helium particle distribution over time at different energy levels from 4.032– 11.493 MeV/n	85
Figure 40 Simulation result showing the dispersion of helium particles along different mean free paths at a level of energy of 4.032 MeV/n.....	86
Figure 41 The spacecraft data of He at 4.032 MeV/n for the solar event on 3 July 2021.....	87
Figure 42 The simulation result of He at 4.032 MeV/n for the solar event on 3 July 2021.....	87
Figure 43 The simulation result of He at 4.032 MeV/n for the solar event on 3 July 2021.....	88
Figure 44 The injection profile of He at 4.032 MeV/n for the solar event on 3 July 2021.....	88
Figure 45 The spacecraft data of He at 4.032 MeV/n for the solar event on 29 November 2020.....	89
Figure 46 The simulation result of He at 4.032 MeV/n for the solar event on 29 November 2020.....	89

Figure 47 The fitting result at 4.032 MeV/n for the solar event on 29 November 2020	90
Figure 48 The injection profile of He at 4.032 MeV/n for the solar event on 29 November 2020.....	90
Figure 49 The spacecraft data of O at 8.538 MeV/n for the solar event on 29 November 2020.....	91
Figure 50 The simulation result of O at 8.538 MeV/n for the solar event on 29 November 2020.....	91
Figure 51 The fitting result of O at 8.538 MeV/n for the solar event on 29 November 2020.....	92
Figure 52 The injection profile of O at 8.538 MeV/n for the solar event on 29 November 2020.....	92
Figure 53 The λ of He at the various energy levels of two events	94
Figure 54 The Injection time of two events at the various energy levels	94
Figure 55 The map showing the impact of the solar flare on the atmosphere	97



CHAPTER I

INTRODUCTION

1.1 Importance and background

Nothing is more crucial to us on Earth than the Sun, the most important star in our solar system. Life would not have started on Earth if it hadn't been for the Sun. The Sun heats our oceans, agitates our atmosphere, shapes weather patterns, and gives energy to growing plants, which sustain life on Earth by producing food and oxygen. However, the Sun's activity changes with the number of sunspots on its surface every 11 years, which is known as the solar cycle (Hathaway, 2015).

The Sun's periodic variations emit electromagnetic energy in various wavelengths, including visible light, radio waves, ultraviolet light, high-energy X-rays, and others. Along with these waves, it emits a stream of radiation in the form of charged particles that comprise the solar wind's plasma (Gorney, 1990). Random outbursts from massive explosions on the Sun, such as solar flares and Coronal Mass Ejections (CMEs), cause Space Weather storms to race across our solar system. Some of these storms strike the magnetosphere, the protective magnetic bubble that surrounds our vulnerable planet. Particle radiation cascading down the magnetic field lines of our planet can harm satellites, impair communications networks, and even short out our electrical power systems. Furthermore, radiation particles occasionally hit atoms in Earth's upper atmosphere, resulting in stunning light displays known as Auroras, Northern Lights, and Southern Lights (NOAA, 2016).

Space weather refers to conditions in space induced by the Sun that can impact the operation and reliability of space-borne and ground-based technological equipment, as well as risk human life (Koons et al., 1999). Space weather is caused by magnetic fields formed in the Sun's outer convective layer when hot ionized gas rises towards the Sun's surface, carrying heat with it. The Sun's differential rotation disrupts these magnetic fields, which subsequently emerge into the corona to form complex magnetic fields. The energy in these fields causes space weather due to magnetic reconnection. Magnetic reconnection in the solar corona simplifies the magnetic field topology,

releasing energy from the magnetic field and increasing the kinetic energy of the corona's electrons and ions (Hapgood, 2018).

So, using distribution data from the Advanced Composition Explorer (ACE) spacecraft to analyze the motion of high-energy particles from the Sun, this research investigated the space weather and physical properties, including the eruptions on the Sun's surface. The data from the ACE spacecraft was collected and simulated using the Ubuntu operating system written in C programming. Furthermore, we compared the injection time of the simulated solar flare and the X-ray injection on the Sun with the space environment.

Solar activity and the Earth's space environment can have a negative impact on a variety of modern technologies. As a result, forecasting Space-weather is crucial to avoid substantial destruction and minimize expenditure. Therefore, the primary objective of this study was to predict and manage the risks associated with a solar eruption by examining the time at which high-energy particles arrive on Earth following the eruption of the Sun and its intensity profile of each element and comparing this to the space environment at the beginning of the 25th solar cycle.

1.2 Purpose of the Study

This work aims to find information on space weather and propagation time of solar energetic particles (SEPs) from the simulation of the two strongest solar events at the beginning of the 25th solar cycle. Instruments on the ACE spacecraft measured and collected the data. The motion of particles was simulated using Ruffolo's transport equation (1995), and the injection time profile of particles was computed when released from Sun to Earth. Thus, the relationship between space weather and SEPs at the beginning of the current solar cycle was analyzed to predict and prevent future incidents on time during solar minimum.

1.3 Scope of the Study

1. Study space weather from spacecraft at the beginning of the 25th solar cycle.
2. Select the strongest solar events for analysis at the beginning of the 25th solar cycle.
3. Compare and analyze the relationship between space weather and the solar event simulation result at the beginning of the 25th solar cycle.



Table 1 Displays a Research Plan

Activities	Month																							
	1	2	3	4	5	6	7	8	9	10	11	12	13	14	15	16	17	18	19	20	21	22	23	24
Study background of the thesis and selection of topic.	█	█	█	█	█	█																		
Study of research related to space weather and select the event of interest to prepare and present the proposal.				█	█	█	█																	
Download and prepare the data for the simulation, prepare the intensity data, initial value.								█	█	█														
Simulate the propagation of SEPs using transport equation in Ubuntu operating system.									█	█	█													
Find the injection time of particle and analyze the data obtained from simulation.										█	█	█												
Write a paper for publication and present on the findings in other university.												█	█	█										
Summarize, analyze the findings and write a book.															█	█	█	█						
Final thesis defense																	█	█	█					
Edit and print the final copy																				█	█	█		
Submit the final copy to the University																						█	█	█

CHAPTER II

LITERATURE REVIEW

2.1 The Structure of the Sun

The Sun is a massive ball of scorching, mostly ionized gas that shines brightly under its influence. It's a star that's around 4.6×10^9 years old. This huge spherical object primarily contains hydrogen (73%) and helium (25%) with minor amounts of oxygen, carbon, and iron. Not only is the Sun formed of blazing gas, but it also comprises layers with varying temperatures (Carroll & Ostlie, 2017). Each layer as shown in figure 1 has its own set of characteristics, as indicated below:

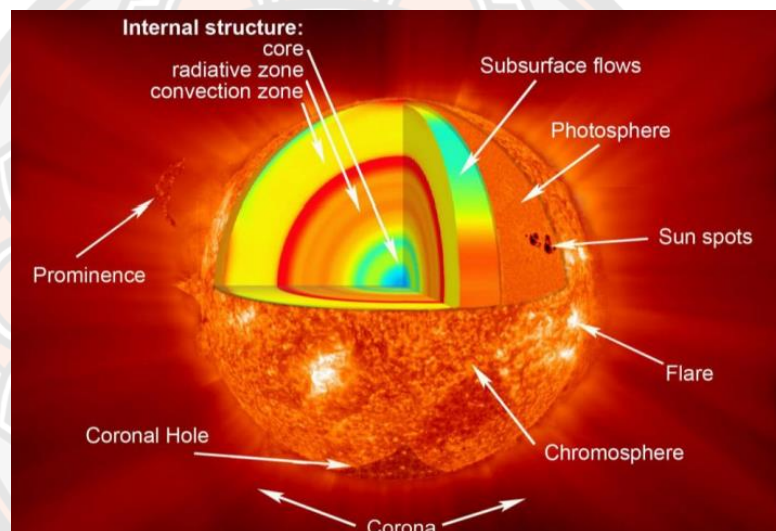


Figure 1 Structure of the Sun

Source: <https://www.coursehero.com/study-guides/earthscienceck12x33/the-Sun/>

The structure of the Sun is primarily divided into two parts:

2.1.1 Internal Structure of the Sun

The interior structure of the Sun comprises the following layers:

2.1.1.1 Core

With a temperature of 1.57×10^7 K, the Sun's core is the hottest component of the solar system. The Sun's solar core stretches from the center to around 20–25 % of the solar radius and is made of hot, concentrated plasma (ions and electrons) at an extremely high pressure of 150 g/cm^3 . In this region of the Sun, a nuclear reaction

known as a P-P chain releases a large amount of heat energy from the fusion of four free protons of hydrogen nuclei into a single alpha particle. Because the energy produced is essentially constant, we don't notice much variation in its brightness or the amount of heat it emits. The energy produced in the core is sent outward through successive layers to different sections of the Sun and then exits into space by photon radiation or large particle advection (Cesar, 2016).

2.1.1.2 The Radiative zone

The radiative zone extends from the periphery of the core to the interface layer at the base of the convection zone (25% to 70% of that distance). The mechanism of energy delivery through radiation defines the radiative zone. The energy produced in the core is carried through the radiative zone by light (photons) that bounce off of particles one after another. Some atoms can survive in the radiation zone because it has a little lower temperature than the core (Hathaway, 2015). These particles have the capacity to absorb energy, fast store it, and then quickly release it as new radiation. As it ascends through the radiation zone, the energy produced in the core is transmitted from one atom to the next. From the bottom to the top of the radiative zone, the density drops from 20 g/cm^3 to 0.2 g/cm^3 . The temperature reduces from $7 \times 10^6 \text{ K}$ to roughly $2 \times 10^6 \text{ K}$ over the same distance.

2.1.1.3 The Convective zone

The solar interior's topmost layer, the convection zone, extends $2 \times 10^5 \text{ km}$ toward the visible surface. The temperature near the bottom of the convection zone is around $2 \times 10^6 \text{ K}$, which is cold enough for heavier ions like nitrogen, carbon, calcium, oxygen, and iron to retain some of their electrons. The substance becomes more opaque, making it harder for radiation to get through. These eventually trap heat, causing the liquid to become unstable and convect. The convective motion rapidly transports heat to the surface, expanding and cooling the fluid as it rises to bring energy to the surface (Hathaway, 2015).

2.1.2 The Atmosphere of the Sun

The Sun's atmosphere is divided into the following three parts:

2.1.2.1 The Photosphere

The lowest part of the Sun's atmosphere is called the photosphere, and it is around 500 km thick. This layer's temperature varies from 4400 K to 10^4 K at the bottom. Deeper photons are unable to escape without being absorbed and reemitted. In this stratum, also known as the Sun's visible surface, the Sun's energy is emitted as light. The Sun lacks Earth's distinct, solid surface because it is a giant ball of plasma (electrified gas). On the other hand, the photosphere is the visible zone with the maximum density and is more opaque due to intense light absorption by hydrogen ions. The photosphere is the disk that appears in the sky when viewed through a telescope with a filter.

2.1.2.2 The Chromosphere

The chromosphere is thicker than the photosphere and has a density 10^{-4} times that of the photosphere. It is a thin layer that lies 2000 km above the visible surface between the photosphere and the solar transition region. Due to the low density and brightness of the photosphere beneath, it is invisible without narrowband filters or during a total solar eclipse. The chromosphere emits a red light when superheated hydrogen burns off, contributing to the transmission of heat from the Sun's core to the corona.

2.1.2.3 The Corona

The corona is the Sun's outermost component, and it is made up of plasma escaping from the Sun at a lower density than the chromosphere. The corona is generally veiled by the intense light of the Sun's surface, and it can only be observed with a special instrument during a total solar eclipse. The temperatures can reach 2×10^6 K, and the gases cool to form the solar wind. Furthermore, the solar wind transports the corona's material to the interplanetary medium.

2.2 The Solar Cycle

The Sun has a predictable pattern of activity. The Solar Cycle, also known as the Sunspot Cycle, is a regular 11-year cycle in which the number of Sunspots grows and declines over time. The solar cycle's two extremes are the solar maximum, or period when solar activity is at its peak and the solar minimum, or period when solar activity is at its lowest or nonexistent. The rise and fall of the Sunspot numbers are shown in figure 2. During the solar maximum stage, the Sunspot will be significant and can remain for weeks; however, the Sunspot will be small and short-lived during solar minimum (NASA, 2021b). As the cycle progresses, Sunspots become more concentrated around the equator; we cannot see Sunspots above a latitude of seventy degrees. The Sun's magnetic field undergoes the solar cycle, during which the positions of the north and south poles tend to switch and causes the magnetic field to become slightly more active in the middle of the cycle. The Sun's north and south poles flip over after about 11 years. During each 11-year cycle, the Sun exhibits the same behavior regardless of which pole is in the upper position (Hathaway, 2015).

Solar activity on the Sun's surface, such as Sunspots produced by the Sun's magnetic fields, is influenced by the solar cycle. The amount of activity on the surface of the Sun changes along with the magnetic field. During the solar maximum, the Sun experiences an increase in the frequency of large eruptions like solar flares and coronal mass ejections (CMEs). These eruptions could impact the Earth because they release a large amount of material and energy into space. Explosions can, for example, generate auroras in the sky, disrupt radio communications, and even disrupt energy grids on Earth (cycle, 2021).

Despite the difficulty of forecasting the Sunspot cycle, scientists are working hard to enhance our capacity to predict the severity and duration of solar cycles. These predictions will be helpful in forecasting these solar conditions, known as space weather (NASA, 2021b). According to Waldmeier's calculations, the first cycle began with the lowest level of solar activity in 1755, followed by the zero cycles, which peaked in 1750 (Künzel, 1962). We are currently in the 25th solar cycle, which began in 2019 as shown in figure 2, thus in the solar minimum phase.

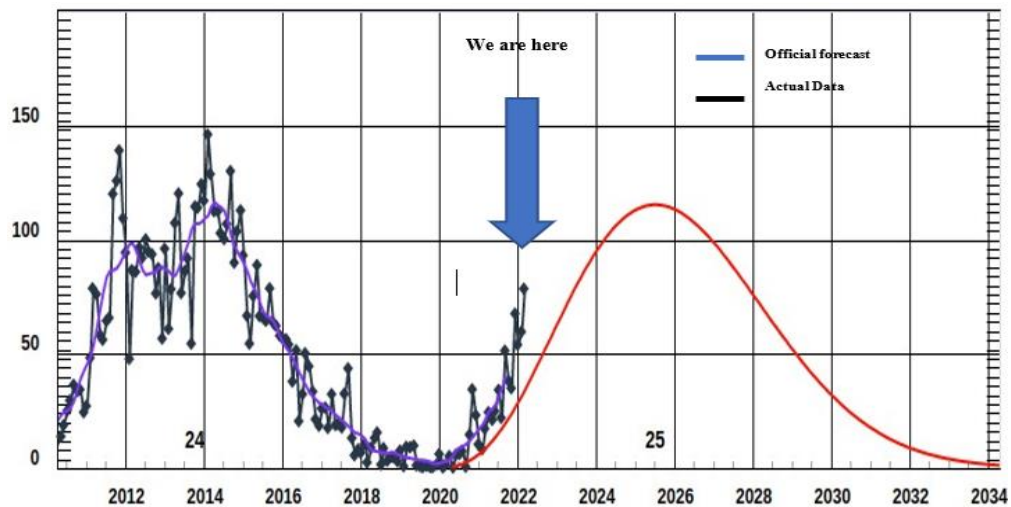


Figure 2 The current solar cycle

Source: <https://spaceweatherarchive.com/2022/01/09/solar-cycle-25-update/>

2.3 The Space Weather

Space weather was defined by Baker (1998) as 'conditions on the Sun and in the solar wind, magnetosphere, ionosphere, and thermosphere that can impact the functionality and dependability of space-borne and ground-based technological systems and jeopardize human life or health' (Baker, 1998). Space weather is caused by the magnetic fields that are created in the Sun's outer convective layer as hot, ionized plasma rises towards the surface and heats that area. When these magnetic fields are deformed by the Sun's differential rotation and escape into the solar atmosphere, the corona and the magnetic reconnection occur. The magnetic reconnection in the solar corona simplifies the topology of the magnetic field, releasing energy from it and increasing the kinetic energy of the electrons and ions in the corona. Due to the field reconfiguration, corona sections can magnetically separate from the Sun and be ejected into planetary space, producing CMEs (Hapgood, 2018).

Solar radiation storms are associated with CMEs and solar flares. In near-Earth space and occasionally even deep inside the Earth's atmosphere, down to sea level, the radiation conditions are noticeably amplified by the explosion of protons, alphas, and heavier ions. While the reconnection event powers flare particles, CME particles are

electrified by shocks that erupt in front of rapid CMEs (Drake, 2009). Flare-induced radiation storms are typically short-lived (less than a day) and arise when particles escape into interplanetary space due to the solar magnetic fields above the flare source (Reames, 1999). Radiation storms caused by CMEs can last for several days because the CME's passage and shock to and beyond Earth excite the particles (Hapgood, 2018). Radiation storms have an impact on a number of electrical and electronic devices, people, satellites, and aircraft. Northern regions are more vulnerable to these effects than areas further south (Kutner, 2012).

Space weather research is vital because radiation from Sun particles connected to massive solar flares can endanger unprotected astronauts, airline occupants, and satellites. On the other hand, space weather does not always have a negative impact. The aurorae pride themselves on being a beautiful, natural result of space weather. Aurorae are similar to rainbows in space weather, except that the rain has nothing to do with shimmering curtains of light. Instead, they form when charged particles from solar eruptions collide with the Earth's upper atmosphere (NOAA, 2016). The same Halloween 2003 space weather event that caused many issues also produced a spectacular aurora. The aurora borealis, often known as the Northern Lights, was so brilliant that sightings were reported worldwide (Mike Hapgood, 2018). We must understand both solar flares and CMEs in order to comprehend and forecast Space Weather and the impact of solar activity on the Earth.

2.4 The Solar Flare

Magnetic reconnection in the solar corona manifests itself most visibly in the generation of solar flares. A solar flare is a bright flash of light created by magnetic energy released by Sunspots. Flares are the most violent explosive phenomena in the solar system, and they are bright regions of the Sun that can last anywhere from a few minutes to several hours. Solar flare photons (or light) can be seen at virtually every spectrum wavelength. Electrons, protons, and heavier particles can all be accelerated by flares. A solar flare occurs when magnetic energy accumulated in the solar atmosphere is rapidly released. A flare produces 10 million times the energy of a volcanic explosion.

The strength of solar flares varies with the solar cycle, and they are categorized based on the brightness of the x-ray wavelength (Paluk et al., 2017). A typical flare goes through three stages:

1. The precursor stage of a solar flare is the stage in which magnetic energy is released. Soft x-ray emission is found at this stage.
2. The impulsive stage occurs when protons and electrons are accelerated to energies greater than 1 MeV. Radio waves, gamma rays, and hard x-rays are emitted during this stage.
3. In the decay stage, soft X-rays gradually build up and decay.

Solar flare stages vary in length, and there is no way to estimate their intensity or duration with any certainty. These stages can take either a few seconds or an hour (NASA, 2021c).

Solar flare explodes from the active region, where a strong magnetic field penetrates the photosphere and connects the solar interior and corona. It is mainly caused by the rapid release of magnetic energy stored in the corona. A flare typically has a temperature of 2×10^7 K, but it can also reach 1×10^8 K. Flares occur in accordance with the Sun's 11-year cycle. When the solar cycle is at its minimum (at the start and end of the solar cycle), active zones are tiny and infrequent, and solar flares are few. Solar flares cannot be seen with the naked eye and should not be attempted. Flares are detected with specialized devices like optical telescopes, and their wavelengths can also be caught using radio telescopes. Flare images are collected by space telescopes and broadcast to Earth. While most people are unaffected by solar flares, bigger flares have been known to disrupt communications and electrical systems. On the other hand, solar flares are responsible for the lovely aurora borealis and aurora Australis. The magnetosphere's energetic particles are responsible for these stunning light displays (Svestka, 2012).

2.4.1 The Classification of solar flares

Solar flares are classified into two groups based on their physical characteristics: impulsive and gradual solar flares. Solar flares are hypothesized to be caused by the release of free energy in coronal magnetic fields, either by reconnection or another type of magnetic dissipation. As a result, impulsive and gradual solar flares

are distinguished by various energy release methods, magnetic dissipation modes, and magnetic configurations.

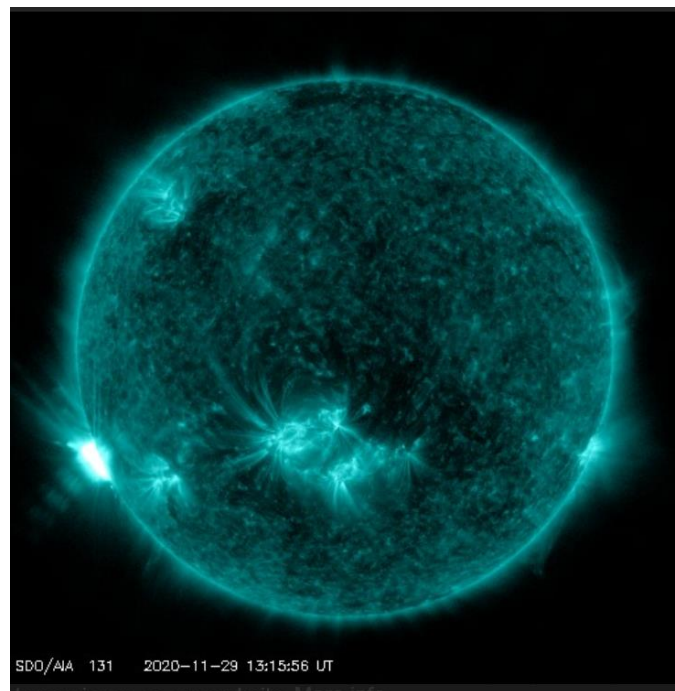


Figure 3 Showing solar flare eruption on 29 November 2020

Source: <https://watchers.news/2020/11/29/m4-4-solar-flare-november-29-2020/>

2.4.1.1 Impulsive Solar Flares

Impulsive solar flares are brief eruptions that release a huge number of electron particles, and the eruption lasts for less than an hour. When particles flow through the Earth, the density of the particles increases rapidly. Indicating that coronal mass ejection would not be released from the corona layer after the eruption and that pace and intensity would be typical, the increase in Fe/O and $^3\text{He}/^4\text{He}$ ratios is four times that of the corona. Thus there is no shock wave phenomenon (Ruffolo, 2002).

2.4.1.2 Gradual Solar Flares

Gradual solar flares are the eruptions of high-energy particles like protons. Coronal mass ejections (CMEs) from the Sun's corona accelerate particles in the interplanetary medium during this sort of eruption. This results in solar storms as the

solar wind accelerates more quickly and powerfully than usual. It will take more than an hour for the particle to be released by the gradual eruption (Ruffolo, 2002).

2.4.2 The Classification of X-rays

According to the X-ray intensity (measured in W/m^2) of 1 to 8 Angstrom X-rays near Earth, as determined by the XRS instrument on board the GOES-15 (The Geostationary Operational Environmental Satellite System) satellite, in a geostationary orbit over the Pacific Ocean, solar flares are classified as A, B, C, M, or X and in it will be displayed as shown in figure 4.

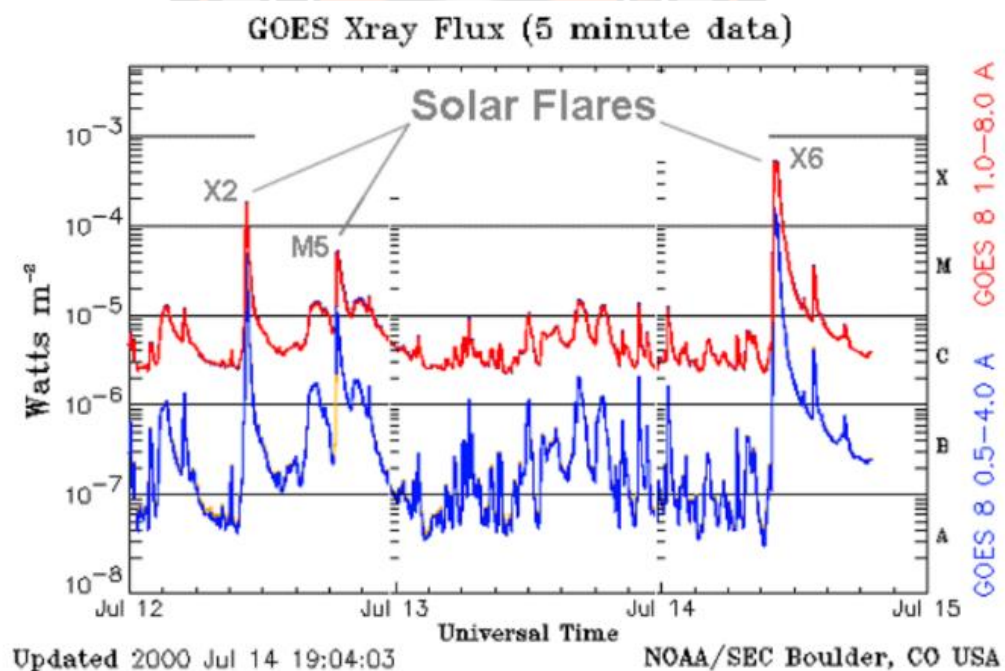


Figure 4 Shows a series of solar flares as detected by NOAA satellites in July 2000

Source: <https://spaceweather.com/glossary/flareclasses.html>

Table 2 The Classification of solar flares at different intensities

Solar flare class	Approximate peak flux range at 100–800 picometre (w/m²)
A	$< 10^{-7}$
B	$10^{-7} - 10^{-6}$
C	$10^{-6} - 10^{-5}$
M	$10^{-5} - 10^{-4}$
X	$> 10^{-4}$

The categorization of X-rays of solar flares based on their intensity is shown in table 2, and the sample of measurement of X-ray intensity from a satellite is shown in figure 4. The detailed explanation and their effects are as follows:

1. A and B class solar flares are the most common types. The background flux, or the amount of energy the Sun gives when no flares are present, is frequently in the B range during solar maximum and the A range during solar minimum.
2. C-class solar flares are minor solar flares with little or no impact on Earth. Although long-duration C-class flares can trigger a coronal mass ejection, their weak and slow nature makes them unlikely to cause significant geomagnetic disturbances on Earth. When a complex Sunspot region is present on the Earth-facing solar disk, the background flux can be in the lower C-class range.
3. M-class solar flares are known as medium-size solar flares. On the Earth's daytime side, they cause minor (R1) to moderate (R2) radio blackouts. Long-duration M-class solar flares are likely to generate a coronal mass ejection. The accompanying geomagnetic storm is anticipated to be strong enough to create aurora at mid-latitudes if the solar flare happens near the center of the Earth-facing solar disk and sends a coronal mass ejection towards our planet.
4. X-class solar flares are the largest and most powerful flares. On average, there are ten solar flares of this size per year, and they are more frequent during solar maximum than solar minimum. During this solar flare, there are strong to extremely strong (R3 to R5) radio blackouts on the dayside of the Earth. If the solar flare is eruptive and happens close to the center of the Earth-facing solar

disk, it may produce a major coronal mass ejection and a powerful and long-lasting solar radiation storm that can result in severe (G4) to intense (G5) geomagnetic storming on Earth (Tandberg-Hanssen & Emslie, 1988).

2.5 The Coronal Mass Ejection

Coronal mass ejections (CMEs) are the most important mechanism through which solar activity can cause space weather effects to be directed toward Earth. The CME is caused by active regions on the Sun's surface that emits a large volume of plasma and a magnetic field. These plasmas are expelled into the solar wind, according to coronagraph imagery. They are routinely observed following solar flares and are most commonly observed during a solar prominence eruption. The Sun produces approximately three CMEs each day near the solar maximum and approximately one CME every five days near the solar minimum (Möstl et al., 2015).

Billions of coronal materials are expelled, each with a magnetic field that is stronger than the solar wind's background interplanetary magnetic field (IMF). CMEs exit the Sun at speeds ranging from less than 250 km/s to around 3000 km/s. Earth-directed CMEs can reach our Earth in as little as 15-18 hours, and slower CMEs can take many days to arrive. As they move away from the Sun, they grow in size, and larger CMEs can occupy over a fourth of the space between Earth and the Sun by the time they reach our planet (NOAA, 2021).

When highly twisted flux ropes or magnetic field structures located in the lower corona of the Sun experience excessive stress, they realign into a less tense form, a process known as magnetic reconnection, and this is when the most explosive CMEs typically occur. Solar flares, which frequently accompany CMEs, are electromagnetic energy bursts that can be caused by magnetic reconnection as well. These CMEs typically originate from regions of the Sun that have localized, intense magnetic flux fields, such as active regions connected to Sunspot groups. CMEs can also form in regions where filaments and prominences, magnetic flux reaching to the inner corona trap and hang comparatively cool and denser plasma. The denser filament or prominence may fall back to the solar surface and be silently reabsorbed when these flux ropes reorganize, or a CME may happen. Shock waves can be produced by CMEs that are moving faster than the pace of background solar wind. These shock waves can

speed up charged particles in their path, increasing the likelihood or intensity of a radiation storm (NOAA, 2021).

When a CME collides with Earth, it initially interacts with the magnetosphere, which is the region of space governed by the Earth's magnetic field. This zone normally extends 60,000 km Sunward of Earth, where it is restricted by the solar wind, a tenuous plasma constantly flowing from the Sun. As seen in figure 5, the magnetosphere spreads out into a lengthy tail on the anti-Sunward side, possibly stretching to a million kilometers or more. The arrival of a large CME compresses the magnetosphere as shown in figure 5, creating an impulse in the Earth's magnetic field. This inflowing energy can then fuel an energy storage cycle in the magnetotail before blasting back toward Earth. It creates aurora, upper-atmosphere heating, and high ionosphere electrical currents. Substorm cycles are a fundamental dynamical cycle of planetary magnetospheres, lasting approximately 1-3 hours on average for the Earth. A huge CME, on the other hand, can go across the Earth in 12-24 hours. As a result, a big CME can cause a number of substorms, culminating in a collection of geomagnetic storms (Hapgood, 2018).

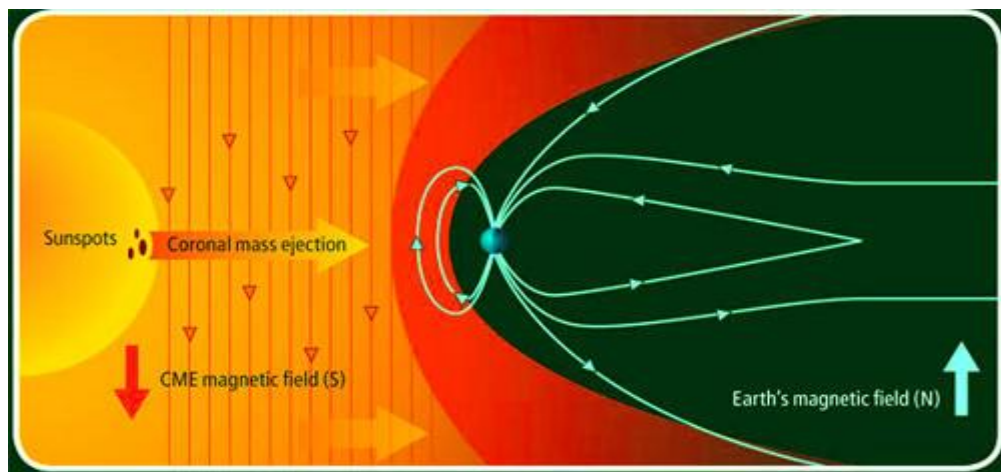


Figure 5 Shows how CME travels from Sun toward Earth

Source: <http://msrblog.com/assign/science/technology/coronal-mass-ejection.html>

2.6 The Solar Wind

A stream of particles that the Sun releases into interplanetary space is known as the solar wind. The solar wind is produced by the plasma from the Sun's corona expanding outward. When the gravity of the Sun can no longer hold down this plasma due to its continual heating, it moves along the Sun's magnetic field lines that extend radially outward (Meyer-Vernet, 2007).

The Sun's magnetic field lines coil up into a massive spinning spiral as it revolves, producing a constant stream of wind. These emissions, called streamers, come from enormous luminous patches called coronal holes that are located in the Sun's corona. The solar wind pulls the ends of the magnetic field lines that extend from these coronal holes, and they extend to such a length that they generate an IMF that encloses all of the planets in our solar system (NASA, 2021a).

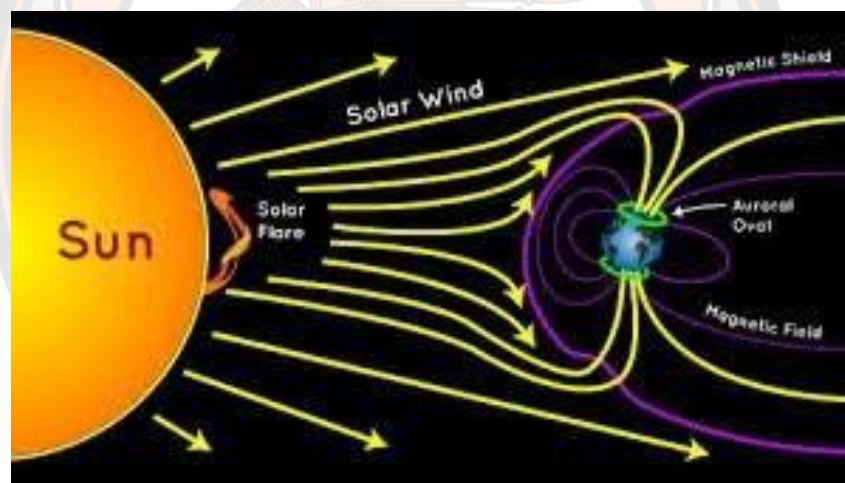


Figure 6 Showing solar radiation storm

Source: <https://lynceans.org/tag/solar-radiation-storm/>

The heliosphere, a vast bubble formed by the solar wind, surrounds the Sun and stretches well beyond the orbits of the majority of the planets in our solar system. Figure 6 shows how, when the solar wind moves farther from the Sun, it spreads outward. It will then encounter a shock wave known as the termination shock and enter subsonic motion since it won't be able to survive the inward pressure of the instellar space medium. The heliosheath, or subsonic flow area, reaches the heliopause, or point where the heliosphere and interstellar medium converge. Magnetic field lines,

magnetosheath, and magnetopause share a topography similar to Earth's magnetic shield (Fisher, 2021).

Some of the magnetic fields of the Sun are carried by the solar wind plasma, as shown in figure 6, as it exits the corona. The interaction of solar wind with Earth and, ultimately, the interstellar medium is profoundly affected by this outward extension of the Sun's magnetic field. The solar wind moves through space at a speed of more than a million miles per hour. Due to the solar wind's rapid movement around the planets in the solar system, bow shocks are created. Bow shocks develop around objects like rockets, the Space Shuttle, and aircraft when they fly faster than the speed of sound in the atmosphere. Due to the magnetic shield, most of the solar wind's energetic particles are forced to orbit and pass beyond Earth when it comes into contact with it. The region around our atmosphere is living and dynamic as the Earth's magnetosphere reacts to the Sun's activity.

The impacts of the solar wind are seen when examining a comet that is near the Sun. Since the solar wind forces the comet's tail material out of the comet's head, the comet's tail always points away from the Sun. The Sun is losing mass at a rate of 10^{14} M/yr, and the wind is still gaining speed as it travels from the Sun to Earth in five to ten days. The orbit of the Earth travels at a speed of about 400 to 450 km/s, and its particle density ranges from 5 to 10 cm^3 . The positive ions and electrons that make up the solar wind have an impact on the Earth. Most solar wind particles that are directed toward Earth never reach the surface because charged particles cannot penetrate field lines; the Earth's magnetic field serves as a shield. However, some particles travel along the field lines and approach the Earth closest to the magnetic poles. These charged particles cause the aurora displays, which explains why aurorae are most visible near magnetic poles, as shown in figure 7. The aurorae grow more prevalent as solar activity rises. Radio interference is also caused by the increased number of charged particles in our environment (Space, 2021).

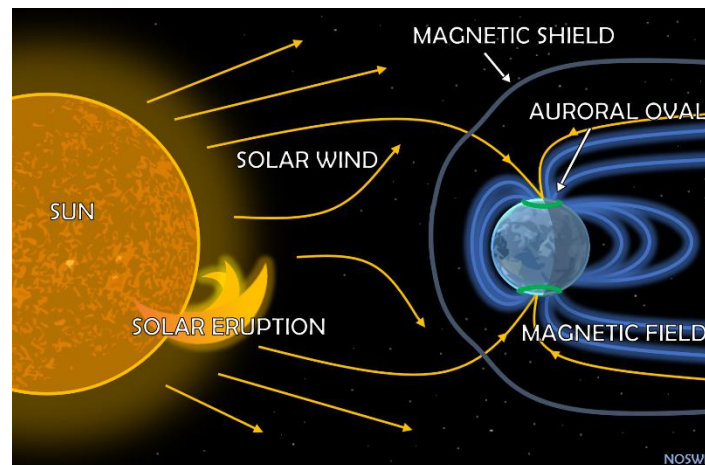


Figure 7 Showing formation of auroras due to solar wind

Source: <https://site.uit.no/spaceweather/what-are-the-northern-lights-aurora/>

2.7 The Solar Energetic Particles

Solar Energetic Particles (SEPs) are high-energy particles released by the Sun that was discovered in the early 1940s. They are composed of protons, electrons, and heavy ions with energy ranging from tens of keV to GeV, and the fastest particle can travel at up to 80% the speed of light. Solar flares, filament eruptions, and CMEs are all critical phenomena related to solar eruptions. Its intensity is determined by the speed of the CME and its magnetic connectivity to Earth (Klein & Dalla, 2017).

SEPs constitute a significant aspect of space weather, endangering people and electrical devices with radiation and ionizing the atmosphere of the Earth. The IMF helped them spread over the interplanetary medium, and the event can last anywhere from a few hours to several days. The space weather impacts of SEPs are brought on by the interaction of the particles with electronics, the Earth's atmosphere, and living things. Because they can interfere with space-borne electronics and produce a large amount of particle radiation, strong SEP occurrences pose a risk to space weather.

The Earth's atmosphere and any exposed materials are exposed to primary radiation from energetic ions and secondary radiation from nuclear processes, increasing ionization and altering the local chemistry of the Earth's high polar atmosphere in certain situations. Beyond the Earth's magnetosphere, SEP occurrences pose a serious obstacle to human spaceflight. Either energization can create SEPs at the

location of a solar flare or shock waves connected to CMEs. But only a small percentage (about 1%) of CMEs cause severe SEP events (Reames, 1999).

2.8 The Interplanetary Magnetic Field

The portion of the Sun's magnetic field that the solar wind carries into interplanetary space is known as the interplanetary magnetic field (IMF). The IMF lines remain in the solar wind plasma, which rotates around the Sun and moves outward in a spiral pattern. The magnetic field is open where the IMF originates on the Sun, which means that field lines leaving one region do not reenter a conjugate zone but rather extend almost indefinitely into space. Each solar cycle, the polarities of the fields in the northern and southern hemispheres of the Sun shift in opposition to one another (State Key Laboratory of space weather, 2007).

IMF is crucial in many space processes. The orientation of the IMF points in the direction ideal for solar wind thermal qualities. Increased IMF intensity efficiently forces energetic particles away from the Sun and out into interplanetary space, excluding low-energy cosmic rays from the solar system. Geomagnetic activity is triggered when the IMF near-Earth rotates southward. In 1958, Parker served as the first model for the principal character of the IMF. The interaction between the solar wind and the magnetosphere of Earth is significantly influenced by the IMF (Gosling, 1997).

2.9 Impact of Space Weather

For years, the impact of space weather has been visible in the polar skies. When the first humans crossed the land bridge from Asia to the Western Hemisphere, the ghostly greens, yellows, and reds of the northern aurora danced above them. That diaphanous color dance continues today, but its impact is more significant than the colors themselves. The technologies listed below are negatively impacted (Eastwood et al., 2017).

1. **Satellite Operation:** Highly energetic ions can enter electronic components and cause bit-flips in a series of electrical impulses, which could lead to erroneous sensor data or spacecraft directives. Less energetic particles can cause a number of spacecraft surface charge problems when geomagnetic activity is high.

2. **Human Space Exploration:** Astronauts on space missions face a health danger from energetic particles, and electrical systems are also at risk. During space missions, astronauts outside of spacecraft are less shielded and more susceptible to radiation from space.
3. **Aviation:** Space weather storms can interfere with communications, expose crew and passengers to radiation, produce inaccurate navigational data, and interfere with electronic systems that are essential for flight.
4. **Electric Power:** Power lines may experience currents caused by ionosphere currents. These induced current surges have the ability to destroy significant portions of the electrical grid and bring about widespread network failures.
5. **Communication:** At all frequencies, space weather has the potential to interfere with communication. Due to the frequency band's reliance on ionosphere reflection for long-distance signal transmission, high-frequency radio communications are more frequently impacted.
6. **Navigation system:** GPS range measurements can be impacted by ionosphere disturbances, and in the worst circumstances, they can result in the receiver losing lock on the GPS signal.

2.10 The Advanced Composition Explorer Spacecraft

The Advanced Composition Explorer (ACE) spacecraft provided the data for this study. Around 1.5 million kilometers away from Earth, at the Sun-Earth L1 Lagrange point, it was created to research energetic particles in space. It was launched on August 25, 1997, to examine the material the Sun ejected to ascertain how the Sun, Earth, and the Milky Way Galaxy interact. The ACE spacecraft is a two-deck irregular octagon approximately 1.6 m wide and 1.0 m in height. It spins on its axis, always pointing one end toward the Sun and the other toward the Earth. Spacecraft's redundant equipment collects and stores data before transmitting it to Earth. The ACE spacecraft weighs approximately 785 kg, including the hydrazine fuel. Additionally, ACE offers geomagnetic storm early warnings and real-time space weather data (Center, 2013; Chiu et al., 1998).

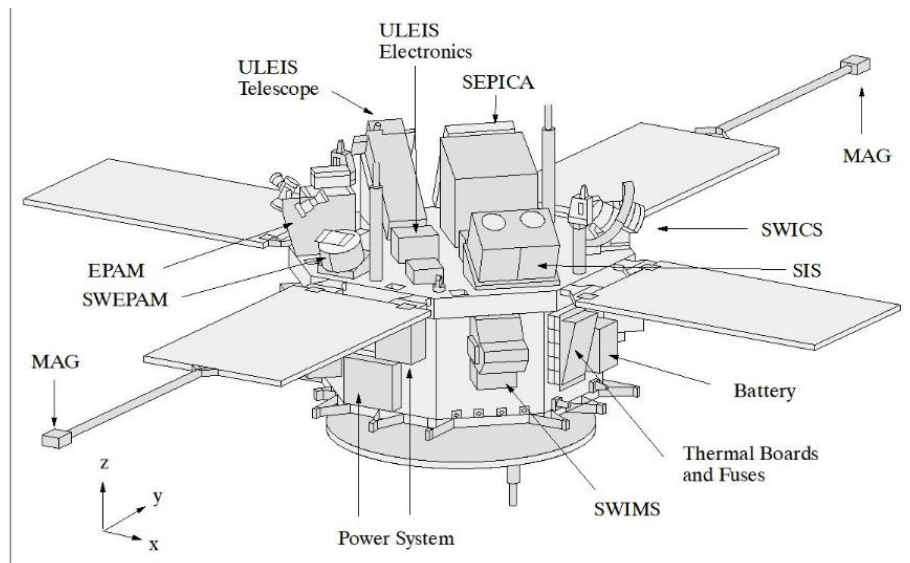


Figure 8 The Line Drawing of Advanced Composition Explorer (ACE) Spacecraft

Source: <https://directory.eoportal.org/web/eoportal/satellite-missions/content/-/article/ace>

As illustrated in figure 8, the ACE spacecraft is equipped with nine instruments, including six high-resolution sensors and three monitoring devices. Aside from the propulsion system, all parts are installed on the body's exterior surfaces to test the instrument. Two on each side and six on the upper deck, facing the Sun, are mounted instruments. A detailed explanation of each part is given below.

1. The SIS (Solar Isotope Spectrometer) is made to offer precise mass measurements of the elements and isotopes that make up solar energetic nuclei with energies between 10 and 100 MeV/n. Position-sensitive silicon strip detectors equipped with customized, low-power electronics are used to monitor particle trajectories.
2. The CRIS (Cosmic Ray Isotope Spectrometer) is made to detect the elemental and isotopic composition of galactic rays in the energy range from 100 to 600 MeV/n. CRIS uses a scintillating optical-fiber trajectory system visible to two CCD cameras to trace the paths of energetic nuclei that stop in four co-aligned stacks of large-area silicon detectors.
3. The SEPICA (Solar Energetic Particle Ionic Charge Analyzer) analyzes energetic ions with energies ranging from 0.2 to 3 MeV/n by measuring their charge state, kinetic energy, and nuclear charge. Between six sets of electrode plates carrying

high voltages of up to 30 kV, particles entering SEPICA's multi-slit collimator are electrostatically deflected. The source plasma's temperature as well as acceleration processes that are charge-to-mass related will be revealed by SEP charge state measurements.

4. The EPAM (Electron, Proton, and Alpha Monitor) measures particle energy with energy levels ranging from 0.3 to 0.5 MeV/n in order to display the energy and density of electrons, particles, alpha and protons.
5. The ULEIS (Ultra-Low Energy Isotope Spectrometer) measures the mass and kinetic energy of nuclei in the range of He to Ni over an energy range of 0.2 to 20 MeV/n by combining exact measurements of their time-of-flight (TOF) over a 50 cm flight path with an assessment of their total kinetic energy. Among the energy ranges covered by ULEIS are solar energetic particles, particles accelerated by interplanetary shocks, and low energy anomalous cosmic rays.
6. The SWIMS (Solar Wind Ion Mass Spectrometer) has a high mass resolution and is designed to research the chemical and isotopic composition of the solar wind for all elements between He and Ni, with a mass resolution of up to 10 keV/e.
7. The SWICS (Solar Wind Ion Composition Spectrometer) combines electrostatic deflection and post acceleration TOF measurements with energy measurements to identify the elemental and ionic charge state composition of all important solar wind ions from H to Fe.
8. The SWEAPAM (Solar Wind Electron, Proton and Alpha Monitor) measures the three-dimensional characteristics of suprathermal electrons with energies between 1 and 900 eV and ions with energies between 0.26 and 35 keV in the solar wind.
9. The MAG (Magnetic Field Experiment) analyzes the dynamic behavior of the vector magnetic field, which controls the movement and acceleration of energetic particles.

The composition of energetic nuclei with energies ranging from the solar wind to galactic cosmic rays is measured using all instruments in terms of their isotopic, elemental, and ionic states. These findings have aided researchers' understanding of the sources, composition, and processes associated with solar wind and SEPs. Additionally, ACE's solar wind plasma, energetic particle, and magnetic field instruments offer continuous measurements of background and disturbed solar wind that are essential for

studying space weather. Because geomagnetic storms can overwhelm electricity lines, interfere with communications on Earth, and endanger astronauts, ACE can alert people to their impending arrival.

The SIS instrument is used to collect data from the nine instruments on ACE for this study. With an energy range of 10 to 100 MeV/n, the SIS is designed to give high-resolution studies of the isotopic composition of energetic nuclei from He to Zn ($Z = 2$ to 30). The flux of solar energetic particles can rise by a factor of 10,000 or more during solar active periods, enabling SIS to determine the composition of solar material and research particle acceleration processes. The anomalous cosmic ray component, which originates in the local interstellar medium during solar quiet times, will also be measured by SIS together with low-energy cosmic rays from the Galaxy and their isotopes. The SIS detector system consists of two-particle telescopes that are identical. Each telescope includes two silicon strip detectors that monitor the nuclear charge, mass, and kinetic energy of incident nuclei. A pair of two-dimensional silicon strip detectors with unique Very Large Scale Integrated (VLSI) circuitry that can measure both position and energy loss are used in each telescope to measure particle trajectories.

SIS was specifically created to obtain exceptional mass resolution in massive solar particle events, which are characterized by extremely high flux circumstances. Its geometry factor, which is considerably greater than that of other solar particle isotope spectrometers, is roughly $40 \text{ cm}^2\text{-sr}$. The device is managed by a CPU that formats data for readout by the spacecraft and prioritizes events into buffers based on their charge, range, angle of incidence, and trajectory determination quality (NASA, 2013).

2.11 The Archimedean Spiral

The locus for a point's location over time as it moves away from a fixed point along a line that spins with a constant rotational velocity is known as the Archimedean Spiral (Wikiwand, 2019).

Particles traveling in a direction parallel to the magnetic field's direction are characterized as

$$\vec{dl} \times \vec{B} = 0 \quad (2.1)$$

$$\vec{\nabla} \times \vec{B} = 0 \quad (2.2)$$

Where: \vec{dl} is a spherical coordinate and

\vec{B} is a magnetic field with zero electric force

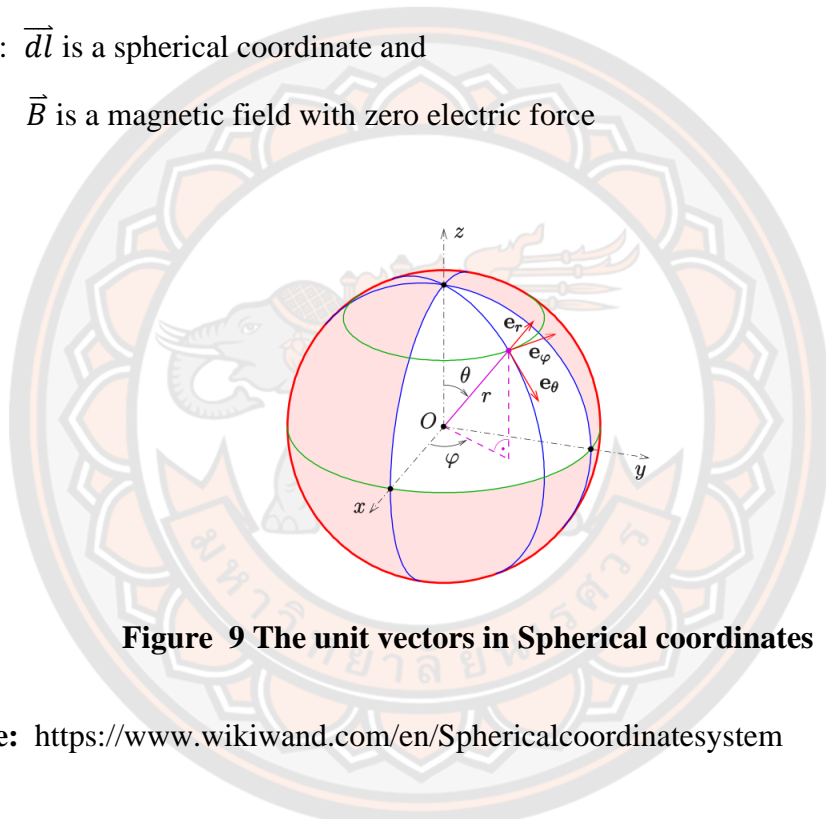


Figure 9 The unit vectors in Spherical coordinates

Source: <https://www.wikiwand.com/en/Sphericalcoordinatesystem>

When the Sun revolves around itself, as shown in figure 9. A magnetic field line in spherical coordinates along the magnetic field's radius will be generated by applying equation (2.1) to the figure by

$$\vec{dl} = dr\hat{e}_r + r d\theta\hat{e}_\theta + r \sin\theta d\varphi\hat{e}_\varphi \quad (2.3)$$

And the magnetic field will be

$$\vec{B}(r, \theta, \varphi) = B_r\hat{e}_r + B_\theta\hat{e}_\theta + B_\varphi\hat{e}_\varphi \quad (2.4)$$

Substituting equations (2.3) and (2.4) in (2.1), we get

$$\vec{dl} \times \vec{B} = (dr\hat{e}_r + r d\theta\hat{e}_\theta + r \sin\theta d\varphi\hat{e}_\varphi) (B_r\hat{e}_r + B_\theta\hat{e}_\theta + B_\varphi\hat{e}_\varphi) = 0$$

$$0 = (rd\theta B_\varphi - B_\theta r \sin\theta d\varphi)\widehat{e}_r + (B_r r \sin\theta d\varphi - B_\varphi dr)\widehat{e}_\theta + (B_\theta dr - B_r r d\theta)\widehat{e}_\varphi$$

Considering the elements along the line \widehat{e}_r , we get

$$\begin{aligned} d\theta B_\varphi &= B_\theta r \sin\theta d\varphi \\ \frac{rd\theta}{B_\theta} &= \frac{r \sin\theta d\varphi}{B_\varphi} \end{aligned} \quad (2.5)$$

Now considering the elements along the line \widehat{e}_θ , we get

$$\begin{aligned} B_r r \sin\theta d\varphi &= B_\varphi dr \\ \frac{r \sin\theta d\varphi}{B_\varphi} &= \frac{dr}{B_r} \end{aligned} \quad (2.6)$$

By equating equations (2.5) and (2.6), we get

$$\frac{dr}{B_r} = \frac{rd\theta}{B_\theta} = \frac{r \sin\theta d\varphi}{B_r} \quad (2.7)$$

From equation (2.7), the relation of $\vec{B}(r, \theta, \varphi)$ for various elements is given by:

$$\begin{aligned} B_r(r, \theta, \varphi) &= B_r(r, \theta, \varphi) \\ B_\theta(r, \theta, \varphi) &= \frac{rd\theta}{dr} B_r(r, \theta, \varphi) \\ B_\varphi(r, \theta, \varphi) &= r \sin\theta \frac{d\varphi}{dr} B_r(r, \theta, \varphi) \end{aligned} \quad (2.8)$$

In the simulation of the Parker spiral, consider only the magnetic field in the equatorial plane, thus $B_\theta = 0$. Therefore equation (2.8) will become

$$\begin{aligned} B_r(r, \theta, \varphi) &= B_r(r, \theta, \varphi) \\ B_\theta(r, \theta, \varphi) &= 0 \\ B_\varphi(r, \theta, \varphi) &= r \sin\theta \frac{d\varphi}{dr} B_r(r, \theta, \varphi) \end{aligned} \quad (2.9)$$

To determine the radius 'r' and the rate of change of the angle ' φ ' of the magnetic field emitted from the Sun.

Consider the Sun revolving about its own axis with an angular velocity ' Ω ' associated with the angle ' φ ' and the magnetic field acting at radius 'r' from the Sun, as shown in figure 10.

R is the distance between Sun and point A in m

v_{sw} is the solar wind speed in m/s

Ω is the angular velocity of the Sun's rotation (2.7×10^{-6} rad s⁻¹)

To find the magnetic field in the direction of \widehat{e}_φ , substitute equation (2.13) in (2.9), we get

$$B_\varphi(r, \theta, \varphi) = r \sin\theta \left(-\frac{\Omega}{v_{sw}} \right) B_r(r, \theta, \varphi) \quad (2.14)$$

Therefore, magnetic field \vec{B} becomes

$$\begin{aligned} \vec{B}(r, \theta, \varphi) &= B_r(r, \theta, \varphi) \widehat{e}_r - \frac{\Omega}{v_{sw}} r \sin\theta B_r(r, \theta, \varphi) \widehat{e}_\varphi \\ \vec{B}(r, \theta, \varphi) &= B_r(r, \theta, \varphi) \left(\widehat{e}_r - \frac{\Omega}{v_{sw}} r \sin\theta \widehat{e}_\varphi \right) \end{aligned} \quad (2.15)$$

In the spherical coordinate system, the vector field's divergence is given by:

$$\frac{1}{r^2} \frac{\partial r^2}{\partial r} B_r - \frac{1}{r \sin\theta} \frac{\partial}{\partial \theta} \sin\theta B_\theta + \frac{1}{r \sin\theta} \frac{\partial B_\varphi}{\partial \varphi} = 0 \quad (2.16)$$

The magnetic field in the equatorial plane, $B_\theta = 0$ and substituting equation (2.9) in (2.16), we get

$$\begin{aligned} \frac{1}{r^2} \frac{\partial r^2}{\partial r} B_r - \frac{1}{r \sin\theta} \frac{\partial}{\partial \varphi} \left(\frac{\Omega}{v_{sw}} r \sin\theta B_r \right) &= 0 \\ \frac{1}{r^2} \frac{\partial r^2}{\partial r} B_r - \left(\frac{\Omega}{v_{sw}} \right) \frac{\partial B_r}{\partial \varphi} &= 0 \end{aligned} \quad (2.17)$$

From equation (14), we get B_r is independent of φ and the value of $r^2 B_r$ is constant, and it depends on θ and doesn't depend on r . Thus,

$$B_r = \frac{A(\theta)}{r^2} \quad (2.18)$$

Now consider that r_1 is a magnetic reference point $B_r = B_1$, so

$$A(\theta) = B_1 r_1^2$$

By substituting $A(\theta)$ in equation (2.18), we get

$$B_r = \frac{B_1 r_1^2}{r^2} \quad (2.19)$$

Now by substituting equation (2.19) in (2.15), we get

$$\vec{B}(r, \theta, \varphi) = \frac{B_1 r_1^2}{r^2} \left(\widehat{e}_r - \frac{\Omega}{v_{sw}} r \sin\theta \widehat{e}_\varphi \right) \quad (2.20)$$

Therefore equation (2.20) gives the properties of Parker spiral's magnetic field in spherical coordinates.

The magnetic field properties in various components are as follows:

$$B_r = \frac{B_1 r_1^2}{r^2} \quad \text{Characteristic of the magnetic field in the radius.}$$

$$B_\theta = 0 \quad \text{Indicates there is no magnetic field in the line } \theta.$$

$$B_\varphi = -\frac{B_1 \Omega r_1^2 \sin \theta}{v_{sw} r} \quad \text{Characteristic of vertical magnetic field } \varphi.$$

2.12 Data analysis of solar eruption's high-energy particles

The diffusion of particles at different times from the simulation $f[t, \mu, z, p]$ is taken into account while analyzing high-energy particle data. Figures 11 and 12 illustrate diffusion characteristics in early and later phases.

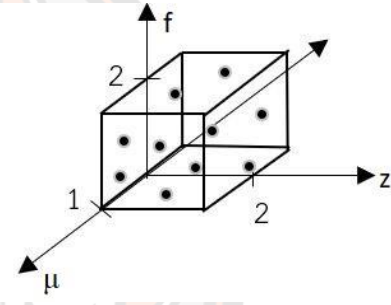
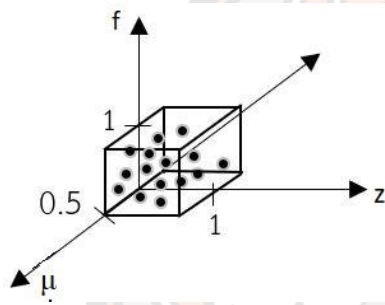


Figure 11 Early phase of diffusion

Figure 12 Later phase of diffusion

As shown in figure 13, the solar wind causes the magnetic field lines to be uneven, making it difficult for high-energy particles to pass through them without being scattered. This analysis of the mean free path (λ) of high-energy particles can help us determine which particles can pass through magnetic field lines before they are scattered.

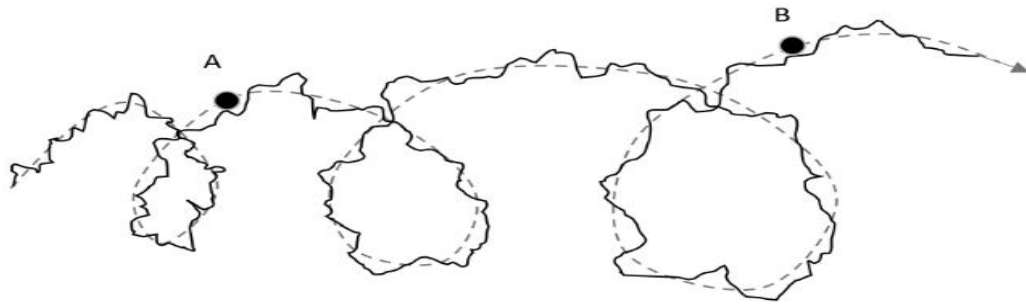


Figure 13 Examples of high-energy particle mean free paths that can move before scattering due to shifting magnetic field lines, with particle A having a shorter mean free path than particle B

2.13 The Transport equation

The propagation of energetic particles through interplanetary space is the primary factor in influencing the consequences of Space Weather (Ruffolo et al., 1998). The Sun emits both charged and neutral electrical particles at high energies. The diffusion-conduction equation can explain the velocity of particles moving along a magnetic field line in space. Considering the particle distribution in one dimension (cell), which can be defined as:

$$f(x, t) = \frac{dN}{dx}$$

$$dN = f(x, t)dx \quad (2.21)$$

The total number of particles in the cell is denoted by N .

Let 'S' be the flux defined as the number of particles (N) moving through a point at unit time t . Then mathematically:

$$S = \frac{N}{\Delta t} \quad (2.22)$$

By substituting equation (2.21) in equation (2.22), we get:

$$S = vf(x, t) \quad (2.23)$$

Thus, N will be:

$$N = f(x, t)\Delta x \quad (2.24)$$

Relationships between equations (2.23) and (2.24) can be stated as follows as the particles move in the axial x -direction through the cell:

$$\frac{\partial}{\partial t}(f \cdot \Delta x) = S\left(x - \frac{\Delta x}{2}\right) - S\left(x + \frac{\Delta x}{2}\right)$$

As $\Delta x \rightarrow 0$

$$\frac{\partial f(x, t)}{\partial t} = -\frac{\partial S(x, t)}{\partial x} \quad (2.25)$$

There are systematic and random mechanisms in the distribution of particles throughout time. When all of the particles in a cell travel in the same direction and at the same speed, this is referred to as a systematic process as in figure 14.

The systematic or convective change is expressed mathematically as:

$$S(x, t)_{convective} = \left(\frac{\Delta x}{\Delta t}\right) f(x, t) \quad (2.26)$$

When particles move randomly or disorderly, this is referred to as random changes, as in figure 15.

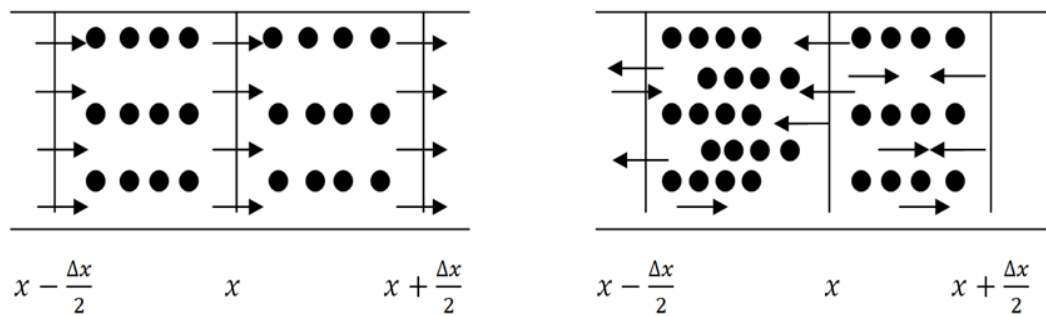


Figure 14 The Systematic flux conduction **Figure 15 The Random flux conduction**

Figure 15 indicates that the left particle's flow is denser than the right.

$$S(x, t)_{diffusive} \propto -\left(\frac{\partial f(x, t)}{\partial x}\right) \quad (2.27)$$

$$S(x, t)_{diffusive} = -D \left(\frac{\partial f(x, t)}{\partial x}\right) \quad (2.28)$$

Substituting equations (2.26) and (2.28) in equation (2.25), we get:

$$\frac{\partial f(x, t)}{\partial t} = \underbrace{-\frac{\partial}{\partial x} \left[\frac{\Delta x}{\Delta t} f(x, t) \right]}_{\text{Systematic first-order}} + \underbrace{\frac{\partial}{\partial x} \left[D \frac{\partial f(x, t)}{\partial x} \right]}_{\text{Random process of diffusion second-order term}} \quad (2.29)$$

Systematic first-order Random process of diffusion second-order term

The motion of particles that decay with time can be explained by the diffusion equation, which has the form of a partial differential equation as:

$$D \frac{\partial^2 F}{\partial x^2} - \frac{\partial F}{\partial t} = 0 \quad (2.30)$$

Where: D is the diffusion coefficient, ∂x is the time period during which the particle moves through the distance ∂x , $\frac{\partial^2 F}{\partial x^2}$ is the number of particles that pass through the phase in one unit volume ∂x and $\frac{\partial F}{\partial t}$ is the variation in particle distribution over time caused by systemic and random variations.

Particle motion was simulated using the Fokker-Plank equation, which is based on the periodic particle distribution equation. Ruffolo (1998) created a simulation equation describing high-energy particles' transit from the Sun.

$$\frac{\partial F}{\partial t} + \frac{\partial(\dot{a}_i F)}{\partial a_i} = Q \quad (2.31)$$

Where: Q is the particle release function (Source term), F is the particle diffusion function (Distribution function), $\frac{\partial F}{\partial t}$ is the particle flux distribution over time, a_i are the parameters of various independent variables connected to movement or independent variables in terms $t, \mu, z,$ and p . Here, t is the amount of time it takes for a particle to travel from the Sun to the Earth (in seconds), μ is the direction of the particle's movement in or out of the Sun, z is the distance along the magnetic field from the Sun to the Earth (AU), and p is the particle's momentum $\left(\frac{\text{MeV}}{c}\right)$.

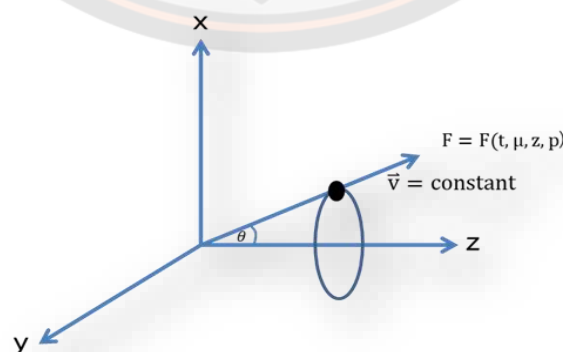


Figure 16 Shows the pitch angle θ between the direction of the magnetic field line and the particle's velocity.

Charged high-energy particles from the Sun flow along magnetic field lines with a speed of \vec{v} , as in figure 16, when we analyzed independent variables that impact their travel.

The following variables can change when we treat the systemic change as an independent variable:

1. Distance change along magnetic field lines in the z-axis
2. Change of momentum
3. Change of μ , where μ is the direction of particle motion.

As; $\mu = \cos \theta$; θ is the spiral phase, the angle between the velocity v of the particle and the magnetic field direction.

The particle approaches the Sun when $\theta > 90^\circ$, $\mu < 0$ and

The particle leaves the Sun when $\theta < 90^\circ$, $\mu > 0$

If F represents the distribution of solar energetic particles, then

$$F(t, \mu, z, p) = \frac{d^3 N}{dz d\mu dp} \quad (2.32)$$

Where, $F(t, \mu, z, p)$ is the dispersing function of high-energy particles emitted by the Sun's outburst, The distance traveled by particles down the magnetic field line to Earth is given by z (AU), p is the momentum of a particle $\left(\frac{\text{MeV}}{c}\right)$, μ is the direction of the particles' motion, t is the time in minutes that the particles take to travel from the Sun to the Earth, and N is the total number of particles.

We analyzed the independent variables of particle motion in terms of random changes since the magnetic field lines on the Sun fluctuate due to solar wind. In terms of random changes, variations in μ along the magnetic field lines in the z-axis with the speed v are independent variables. When we take multiple independent variables into account, the equation becomes:

$$\begin{aligned} \frac{\partial F(t, \mu, z, p)}{\partial t} &= \frac{\partial}{\partial z} \left(\frac{\Delta z}{\Delta t} F \right) - \frac{\partial}{\partial \mu} \left(\frac{\Delta \mu}{\Delta t} F \right) - \frac{\partial}{\partial p} \left(\frac{\Delta p}{\Delta t} F \right) \\ &+ \frac{\partial}{\partial \mu} \left[\frac{\varphi \mu}{2} \frac{\partial}{\partial} \left(\frac{E'}{E} F \right) \right] \end{aligned} \quad (2.32)$$

The equation (2.32) considers fixed frame, solar wind frame, and mixed frame. The particle ratio from the stationary frame to the solar wind frame is determined by:

The velocity of particles in fixed frame v and solar wind frame is defined as v' . In the fixed frame, conservative velocity is given by the equation

$$v = v' + v_{sw} \quad (2.35)$$

where:

v_{sw} is solar wind speed

v_{\parallel} is the velocity parallel to the magnetic field lines in the fixed frame

v_{\perp} is the velocity perpendicular to the magnetic field lines in the fixed frame

v'_{\parallel} is the velocity parallel to the magnetic field lines in the solar wind frame

v'_{\perp} is the velocity perpendicular to the magnetic field lines in the solar wind frame

When we consider the stationary reference frame and the solar wind, as shown in figures 17 and 18, the particles will be traveling in the solar wind frame (v_{sw}) at the same speed as indicated in the equation:

$$v' = v - v_{sw} \quad (2.36)$$

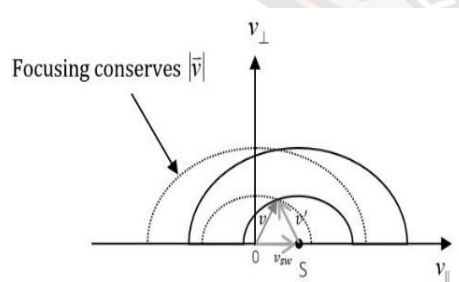


Figure 17 The Stationary reference frame

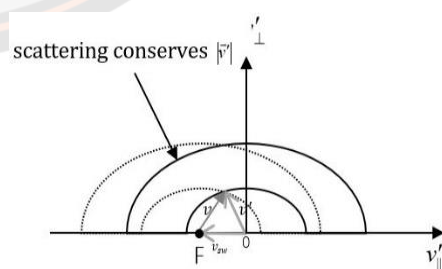


Figure 18 The solar wind reference frame

According to the equation, the deceleration rate will result in a drop in the particle's velocity in the solar wind frame under scattering and focusing.

$$\dot{v}' = \frac{dv'}{d\mu} \Big|_v \dot{\mu} \quad (2.37)$$

Where:

- μ direction of motion of the particle. $\mu = \cos \theta$
- $\dot{\mu}$ rate of change in particle movement direction over time
- v the velocity of particles in a stationary frame
- v' the velocity of particles in the solar wind frame
- \dot{v}' rate of change of the velocity in the solar wind reference frame.

As shown in figure 19, consider the magnetic field lines that the Sun has released in a fixed reference frame.

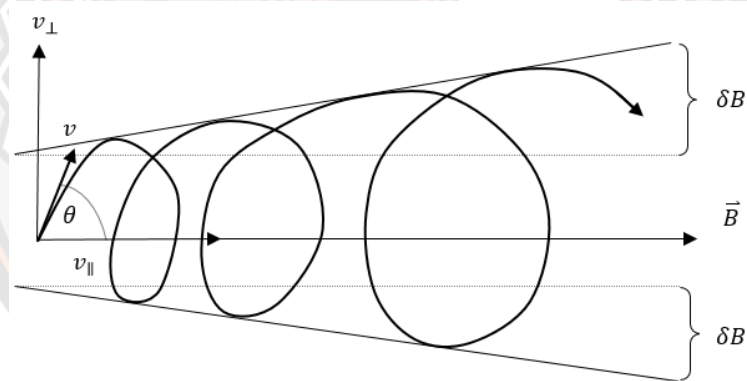


Figure 19 The properties of magnetic field lines

When the particles move along the distance z-axis, the strength of the magnetic field of the Sun weakens with increasing distance. As stated in the following definition of the focusing length

$$\frac{1}{L(z)} = -\frac{1}{B} \frac{dB}{dz} \quad (2.38)$$

Where:

$L_{(z)}$ is the length of field lines along the z – axis (AU)

B is the magnetic field (T)

Z is the distance of the particles from the Sun to Earth (AU)

According to the Lorentz force equation, particles that pass between the Sun and the intermediate planets generate force due to the magnetic field as

$$\vec{F} = q(\vec{E} + \frac{\vec{v}}{c} \times \vec{B}) \quad (2.39)$$

Where:

\vec{F} is the force due to the magnetic field (N)

q is the charged particle (C)

\vec{v} is the velocity of the particle (m/s)

\vec{B} is the magnetic field (T)

\vec{E} is the electric field (V/m)

c is the speed of light (3×10^8 m/s)

Since the particles in the interplanetary medium move close to the speed of light and the electric field is zero ($\vec{E} = 0$), we do not take this into account. As a result, the force caused by the flux of the perpendicular magnetic field lines is as follows.

$$\Delta F = \frac{ev_{\perp}}{c} \delta B \quad (2.40)$$

And from the centripetal force

$$\begin{aligned} \frac{mv_{\perp}^2}{R} &= \frac{ev_{\perp}}{c} \delta B \\ R &= \frac{mv_{\perp}}{eB} \end{aligned} \quad (2.41)$$

When, $p_{\perp} = mv_{\perp}$, we get

$$R = \frac{p_{\perp} c}{eB}$$

As R is the radius of the curvature of the magnetic field lines and

let $\vec{F} = m\vec{a}$, then equation (2.41) becomes

$$\begin{aligned} ma &= \frac{ev_{\perp}}{c} \delta B \\ a &= \frac{ev_{\perp}}{mc} \delta B \\ \frac{\partial v_z}{\partial t} &= \frac{ev_{\perp}}{mc} \delta B \end{aligned}$$

When $v_z = v \cos \theta = v\mu$, the above equation becomes

$$\frac{\partial(v\mu)}{\partial t} = \frac{ev_{\perp}}{mc} \delta B$$

Where v is constant

$$\dot{\mu} = \frac{ev_{\perp}}{mcv} \delta B \quad (2.42)$$

From the Maxwell equation $\vec{\nabla} \cdot \vec{B} = 0$

$$\vec{\nabla} \cdot \vec{B} = \frac{\partial B_x}{\partial x} + \frac{\partial B_y}{\partial y} + \frac{\partial B_z}{\partial z} = 0$$

Given that the velocity of the particles is thought to follow the lines of the magnetic field on the z-axis, then $\vec{B} \propto \frac{1}{r^2}$.

Based on the definition of focusing of the magnetic field

$$\frac{1}{L(z)} = -\frac{1}{B} \frac{dB}{dz} \quad (2.43)$$

$$\frac{1}{L(z)} = -r^2 \frac{d}{dz} \left(\frac{1}{r^2} \right)$$

$$\frac{1}{L(z)} = \frac{1}{B} \frac{dB}{dz} = \frac{2}{r}$$

Substitute $\frac{\partial B_x}{\partial x} = \frac{\partial B_y}{\partial y}$ in the Maxwell equation, we get

$$\frac{\partial B_y}{\partial y} + \frac{\partial B_y}{\partial y} + \frac{\partial B_z}{\partial z} = 0$$

$$\frac{2 \partial B_y}{\partial y} = -\frac{\partial B_z}{\partial z}$$

$$\frac{\partial B_y}{\partial y} = -\frac{\partial B_z}{2 \partial z}$$

Consequently, we obtain the following by combining the magnetic field line and radius

$$\delta B = -\frac{1}{2} \frac{\partial B_z}{\partial z} R \quad (2.44)$$

Substituting equations (2.41) and (2.43) in (2.42), we will get

$$\dot{\mu} = \frac{ev_{\perp}}{mcv} \left(-\frac{1}{2} \frac{\partial B_z}{\partial z} \frac{mv_{\perp}c}{eB} \right)$$

$$\dot{\mu} = -\frac{1}{2B} \frac{\partial B_z}{\partial z} \frac{v_{\perp}^2}{v}$$

By substituting equation (2.43) in the above equation, we get

$$\dot{\mu} = \frac{1}{2L(z)} \frac{v^2(1-\mu^2)}{v}$$

$$\dot{\mu} = \frac{v(1-\mu^2)}{2L(z)} \quad (2.45)$$

Where $L(z)$ is the length of the magnetic field and z is the length of the arc the particle makes as it travels from the Sun to the Earth along the magnetic field line.

And according to equation (2.13), the relationship between the solar wind speed and the magnetic field is perpendicular and parallel, as depicted in Figure 20.

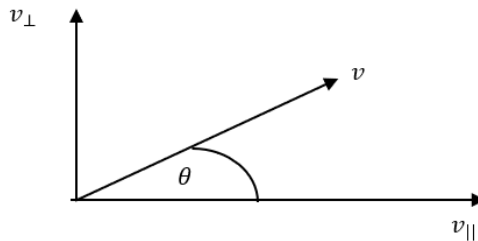


Figure 20 The relationship between parallel and perpendicular velocity in reference to magnetic field lines

We can write the relationship as below from figure 20.

$$v_{\perp} = v \sin \theta$$

$$v_{\perp}^2 = v^2 \sin^2 \theta$$

$$v_{\perp}^2 = v^2 (1 - \cos^2 \theta)$$

$$v_{\perp}^2 = v^2 - v_{\parallel}^2$$

In magnetic field lines, the particle is moving at the velocity \vec{v} with an angle θ along the z-axis.

The following equation gives the velocity v' in the solar wind frame,

$$v' = \sqrt{v_{\parallel}'^2 + v_{\perp}'^2} \quad (2.46)$$

When

$$v_{\parallel}' = v_{\parallel} - v_{sw} \quad (2.47)$$

The perpendicular velocity is the same in both the fixed reference frame and the solar wind frame, i. e $v_{\perp}' = v_{\perp}$, then by substituting equation (2.47) in (2.46), we will get

$$v' = \sqrt{(v_{\parallel} - v_{sw})^2 + v_{\perp}^2}$$

$$v' = \sqrt{v_{\parallel}^2 - 2v_{\parallel}v_{sw} + v_{sw}^2 + v_{\perp}^2}$$

If $v^2 = v_{\parallel}^2 + v_{\perp}^2$, then we will get

$$v' = \sqrt{v^2 - 2v_{\parallel}v_{sw} + v_{sw}^2}$$

If $v_{\parallel} = v \cos \theta = v\mu$, then

$$v' = \sqrt{v^2 - 2v\mu v_{sw} + v_{sw}^2} \quad (2.48)$$

To find the rate of change of velocity in the solar wind frame, substitute equations (2.45) and (2.48) in (2.37) as

$$\begin{aligned} \dot{v}' &= \left. \frac{dv'}{d\mu} \right|_v \dot{\mu} \\ \dot{v}' &= \left[\frac{d}{d\mu} (v^2 - 2v\mu v_{sw} + v_{sw}^2)^{\frac{1}{2}} \right] \cdot \left[\frac{v(1-\mu^2)}{2L(z)} \right] \\ \dot{v}' &= \left[\frac{1}{2} (v^2 - 2v\mu v_{sw} + v_{sw}^2)^{-\frac{1}{2}} \frac{d}{d\mu} (v^2 - 2v\mu v_{sw} + v_{sw}^2) \right] \cdot \left[\frac{v(1-\mu^2)}{2L(z)} \right] \\ \dot{v}' &= \left[\frac{-v v_{sw}}{(v^2 - 2v\mu v_{sw} + v_{sw}^2)^{\frac{1}{2}}} \right] \cdot \left[\frac{v(1-\mu^2)}{2L(z)} \right] \end{aligned}$$

Further, by substituting equation (2.48) in the above equation, we will get

$$\begin{aligned} \dot{v}' &= \left[-\frac{v v_{sw}}{v'} \right] \cdot \left[\frac{v(1-\mu^2)}{2L(z)} \right] \\ \dot{v}' &= -\frac{v^2 v_{sw} (1-\mu^2)}{v' 2L(z)} \end{aligned}$$

Considering the conservation of velocity \vec{v} , $v = v'$, then the above equation becomes

$$\dot{v}' = -\frac{v' v_{sw} (1-\mu^2)}{2L(z)}$$

Thus, the rate of change of velocity in the solar wind frame will be

$$\dot{v}' = -\frac{v' v_{sw}}{2L(z)} (1 - \mu^2) \quad (2.49)$$

As $p = mv$, equation (2.49) becomes

$$\dot{p}' = -\frac{p' v_{sw}}{2L(z)} (1 - \mu^2) \quad (2.50)$$

Thus equation (2.50) gives the rate of change of momentum in the solar wind frame due to decreased momentum in the solar wind in accordance with adiabatic focusing.

Differential convection occurs when the momentum change rate depends on the length of the magnetic field line (z) and the value of the solar wind velocity at various positions (v_{sw}^c), then

$$v_{sw}^c = v_{sw} - \Omega r \sin \theta$$

$$\dot{p}' = -\frac{p' v_{sw} \sec \Psi}{2L(z)} (1 - \mu'^2) \quad (2.51)$$

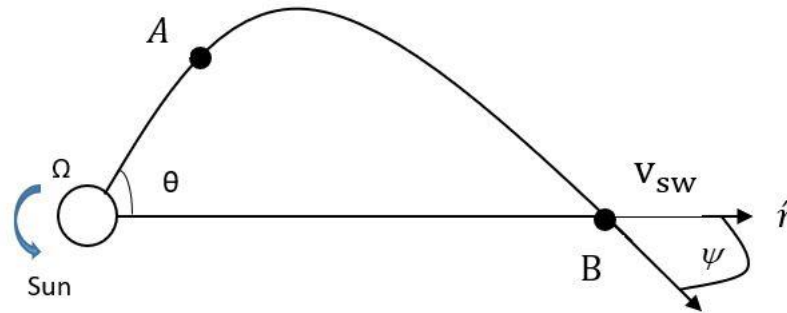


Figure 21 The magnetic field acting on the Sun's radial line

Figure 21 depicts the following relationship:

$$\cos \Psi = \frac{v_{sw}}{v_{sw}^c}$$

$$v_{sw}^c = v_{sw} \sec \Psi$$

By substituting the above equation in (2.51), we get,

$$\dot{p}' = -\frac{p' v_{sw} \sec \Psi}{2L(z)} (1 - \mu'^2) \quad (2.52)$$

$$\dot{p}' = -\frac{p' v_{sw}^c}{2L(z)} (1 - \mu'^2) \quad (2.53)$$

We can write equation (2.47) as

$$v_{\parallel} = v'_{\parallel} + v_{sw}$$

And as $E = mc^2$, we get

$$m = \frac{E}{c^2}$$

Thus, the solar wind speed's effect on the momentum along the magnetic field line in different coordinates will be

$$p_{\parallel} = p'_{\parallel} + \left(\frac{E}{c^2}\right) v_{sw}^c$$

$$p'_{\parallel} = p_{\parallel} - \left(\frac{E}{c^2}\right) v_{sw}^c \quad (2.54)$$

From equation (2.54), the decreasing momentum of the particles in solar wind from point A to B will be

$$p'_{\parallel, A} = p_{\parallel} - \left(\frac{E}{c^2}\right) v_{sw}^c, A \quad (2.55)$$

$$p'_{\parallel, B} = p_{\parallel} - \left(\frac{E}{c^2}\right) v_{sw}^c, B \quad (2.56)$$

Thus, from equations (2.55) and (2.56), we get

$$\Delta p'_{\parallel} = - \left(\frac{E}{c^2}\right) \Delta v_{sw}^c$$

$$\Delta p'_{\parallel} = - \left(\frac{E}{c^2}\right) \Delta v_{sw} \sec \Psi$$

The angle Ψ denotes the relationship between the radius (r) and the axis (z), then

$$\cos \Psi = \frac{dr}{dz}$$

$$dr = \cos \Psi dz$$

Where:

z is the length of the magnetic field along the spiral

Δz is the distance from point A to B along the magnetic field lines

Δt is the time taken from point A to B

Considering all the relationships, then

$$\Delta p'_{\parallel} = - \left(\frac{E}{c^2}\right) \Delta v_{sw} \left(\frac{d}{dz} \sec \Psi\right) \Delta z$$

If $\Delta z = v_{\parallel} \Delta t$, then the above equation becomes

$$\Delta p'_{\parallel} = - \left(\frac{E}{c^2}\right) \Delta v_{sw} \left(\frac{dr}{dz} \frac{d(\sec \Psi)}{dr}\right) v_{\parallel} \Delta t$$

$$\Delta p'_{\parallel} = - \left(\frac{E}{c^2}\right) \Delta v_{sw} \left(\cos \Psi \frac{d(\sec \Psi)}{dr}\right) v_{\parallel} \Delta t$$

As $m = \frac{E}{c^2}$ and $v_{\parallel} = v\mu$, then the above equation becomes

$$\dot{p}'_{\parallel} = -p'_{\parallel} v_{sw} \left(\cos \Psi \frac{d(\sec \Psi)}{dr}\right) \quad (2.57)$$

Equation (2.57) explains the change in momentum along a magnetic field line from one point to another, which is in accordance with Ruffolo's particle transport equation (1995,1998).

As the momentum in the solar wind frame (p') depends on the conduction of the solar wind particles, then $p'_{\perp} = 0$ and $p_{\parallel} v_{sw} = p' v_{sw}$. Therefore, we can determine the rate of decreasing momentum from the change of solar wind v_{sw}^c as follows:

$$\dot{p}' = \frac{v_{\parallel} \dot{p}'_{\parallel}}{p'} \quad (2.58)$$

If $p'_{\parallel} = p' \mu'$, the equation (2.58) becomes

$$\dot{p}' = \mu' \dot{p}'_{\parallel}$$

By substituting the above equation in equation (2.58), we get

$$\dot{p}' = \mu' \left[-p'_{\parallel} v_{sw} \left(\cos \psi \frac{d(\sec \psi)}{dr} \right) \right]$$

If $p_{\parallel} = p \mu$, and $\mu = \mu'$, then above equation will become

$$\dot{p}' = -p v_{sw} \left(\cos \psi \frac{d(\sec \psi)}{dr} \right) \mu'^2 \quad (2.59)$$

Therefore, by combining equations (2.53) and (2.59), we get

$$\dot{p}' = -\frac{p' v_{sw} \sec \psi}{2L(z)} (1 - \mu'^2) - p v_{sw} \left(\cos \psi \frac{d(\sec \psi)}{dr} \right) \mu'^2$$

If $p = p'$, then

$$\dot{p}' = -p' v_{sw} \left[\frac{\sec \psi}{2L(z)} (1 - \mu'^2) + \left(\cos \psi \frac{d(\sec \psi)}{dr} \right) \mu'^2 \right] \quad (2.60)$$

Thus equation (2.60) gives the rate of momentum change in the solar wind frame, which results from the overall deceleration.

Considering how solar wind affects the movement of particles in the interplanetary medium (on z and μ), then

$$v_{\parallel} = v'_{\parallel} + v_{sw}$$

$$E = mc^2 = pc$$

And from

$$p'_{\parallel} = p' \mu'$$

$$v_{sw}^c = v_{sw} \sec \psi$$

As a result, we can express the relationship between the fixed reference frame and the solar wind frame using the following notation:

$$\frac{E}{c^2} v_{\parallel} = p'_{\parallel} + \frac{E}{c^2} v_{sw}^c$$

$$\frac{E}{c^2} v_{\parallel} = p' \mu' + \frac{E}{c^2} v_{sw}^c$$

when $p' = m' v'$, then the above equation becomes

$$\frac{E}{c^2} v_{\parallel} = m' v' \mu' + \frac{E}{c^2} v_{sw}^c$$

$$v_{\parallel} = \frac{m' v' \mu' c^2}{E} + v_{sw}^c$$

And when $v_{\parallel} = \dot{z}$, then

$$\dot{z} = \frac{m'v'\mu'^2c^2}{E} + v_{sw} \sec \psi$$

And when $m'^2c^2 = E'$, then

$$\dot{z} = v'\mu' \frac{E'}{E} + v_{sw} \sec \psi \quad (2.61)$$

To find $\frac{E'}{E}$, we know that from equation (2.57), $p'_{\parallel} = p_{\parallel} - \left(\frac{E}{c^2}\right)v_{sw}^c$,

And when $p_{\parallel} = p'_{\parallel}$, we will get

$$cp_{\parallel} = cp'_{\parallel} + \left(\frac{E}{c^2}\right)v_{sw}^c$$

$$E = E' + \left(\frac{E}{c^2}\right)v_{sw}^c$$

$$E = pE' + pv_{sw}^c$$

$$E' = E - p'_{\parallel}v_{sw}^c$$

$$E' = E \left(1 - \frac{p'_{\parallel}v_{sw}^c}{E}\right)$$

$$\frac{E'}{E} = 1 - \frac{p'_{\parallel}v_{sw}^c}{E}$$

$$\frac{E'}{E} = 1 - \frac{mv'_{\parallel}v_{sw}^c}{mc^2}$$

When $v'_{\parallel} = v'\mu'$, then

$$\frac{E'}{E} = 1 - \frac{v'\mu'v_{sw}^c}{c^2}$$

Then by substituting $\frac{E'}{E}$ in equation (2.61), we will get

$$\dot{z} = v'\mu' \left[1 - \frac{v'\mu'v_{sw}^c}{c^2}\right] + v_{sw} \sec \psi$$

$$\dot{z} = v'\mu' \left[1 - \frac{v'\mu'v_{sw} \sec \psi}{c^2}\right] + v_{sw} \sec \psi$$

$$\dot{z} = v'\mu' - \frac{v'^2\mu'^2}{c^2}v_{sw} \sec \psi + v_{sw} \sec \psi$$

$$\dot{z} = v'\mu' + \left[1 - \frac{v'^2\mu'^2}{c^2}\right]v_{sw} \sec \psi \quad (2.62)$$

Equation (2.62) shows that streaming and convection are two terms that describe the change in the distance along the magnetic field with time which is in accordance with Ruffolo's transport equation (1995,1998). The first term is "streaming," which explains how particles flow from one point to another without being

influenced by the speed of the solar wind. Convection, the second term, describes the movement of particles along the magnetic field influenced by the solar wind.

Considering the change in μ based on the time in the stationary reference frame and solar wind frame, we can determine the following equations.

Consider the change of μ based on time in the fixed reference frame and the frame of the solar wind.

First, considering the change of μ in the stationary frame from the adiabatic focus, from the equation (2.45) we know that

$$\dot{\mu} = \frac{1}{2L(z)} v(1 - \mu^2)$$

Second, considering the change of μ in the solar wind frame and by using the chain rule, we get

$$\begin{aligned} \frac{d\mu'}{dt} &= \left. \frac{d\mu'}{d\mu} \right|_p \frac{d\mu}{dt} \\ \dot{\mu}' &= \left. \frac{d\mu'}{d\mu} \right|_p \dot{\mu} \end{aligned} \quad (2.63)$$

As

$$p'_{\parallel} = p'_{\mu'} \quad (2.64)$$

And we know that

$$p'_{\parallel} = p_{\parallel} - \left(\frac{E}{c^2}\right) v_{sw}^c \quad (2.65)$$

$$\text{And } p_{\perp} = p'_{\perp},$$

$$\text{Then } p' = \sqrt{p'^2_{\parallel} + p'^2_{\perp}} \quad (2.66)$$

As the momentum is perpendicular to the magnetic field lines, it has no effect on the particle motion, i. e. $p'_{\perp} = 0$, then by substituting equation (2.65) in (2.66), we get

$$p' = \sqrt{p'^2_{\parallel} - 2p_{\parallel} \frac{E}{c^2} v_{sw}^c + \left(\frac{E}{c^2} v_{sw}^c\right)^2}$$

Then the equation (2.66) becomes

$$\dot{\mu} = \frac{p_{\parallel} - \left(\frac{E}{c^2}\right) v_{sw}^c}{\sqrt{p'^2_{\parallel} - 2p_{\parallel} \frac{E}{c^2} v_{sw}^c + \left(\frac{E}{c^2} v_{sw}^c\right)^2}}$$

And, when $p_{\parallel} = p\mu$,

$$\dot{\mu} = \frac{p\mu - \left(\frac{E}{c^2}\right)v_{sw}^c}{\sqrt{p'^2_{\parallel} - 2p\mu\frac{E}{c^2}v_{sw}^c + \left(\frac{E}{c^2}v_{sw}^c\right)^2}}$$

And, when $p'^2_{\parallel} = p'^2$

$$\dot{\mu} = \frac{p\mu - \left(\frac{E}{c^2}\right)v_{sw}^c}{\sqrt{p'^2 - 2p\mu\frac{E}{c^2}v_{sw}^c + \left(\frac{E}{c^2}v_{sw}^c\right)^2}}$$

$$\begin{aligned} \mu' &= \left[p\mu - \frac{E}{c^2}v_{sw}^c \right] \left[p'^2 - \frac{2E}{c^2}p\mu v_{sw}^c + \left(\frac{E}{c^2}v_{sw}^c\right)^2 \right] \\ \frac{d\mu'}{d\mu} &= \left[p\mu - \frac{E}{c^2}v_{sw}^c \right] \left\{ -\frac{1}{2} \left[p'^2 - \frac{2E}{c^2}p\mu v_{sw}^c + \left(\frac{E}{c^2}v_{sw}^c\right)^2 \right]^{-3/2} \left[-\frac{2E}{c^2}p v_{sw}^c \right] \right\} + \\ &\quad \left[p'^2 - \frac{2E}{c^2}p\mu v_{sw}^c + \left(\frac{E}{c^2}v_{sw}^c\right)^2 \right]^{-\frac{1}{2}} p \\ \frac{d\mu'}{d\mu} &= \frac{-\frac{1}{2} \left[p\mu - \frac{E}{c^2}v_{sw}^c \right] \left[-\frac{2E}{c^2}p v_{sw}^c \right]}{\left[p'^2 - \frac{2E}{c^2}p\mu v_{sw}^c + \left(\frac{E}{c^2}v_{sw}^c\right)^2 \right]^{3/2}} + \frac{p}{\left[p'^2 - \frac{2E}{c^2}p\mu v_{sw}^c + \left(\frac{E}{c^2}v_{sw}^c\right)^2 \right]^{1/2}} \end{aligned}$$

From

$$\begin{aligned} p' &= \sqrt{p'^2_{\parallel} - 2p_{\parallel}\frac{E}{c^2}v_{sw}^c + \left(\frac{E}{c^2}v_{sw}^c\right)^2} \\ \frac{d\mu'}{d\mu} &= \frac{-\frac{1}{2} \left[-\frac{2E}{c^2}p^2\mu v_{sw}^c + \frac{2E^2}{c^4}p(v_{sw}^c)^2 \right]}{p'^3} + \frac{p}{p'} \\ \frac{d\mu'}{d\mu} &= \frac{Ep^2\mu v_{sw}^c}{c^2p'^3} - \frac{E^2p(v_{sw}^c)^2}{c^4p'^3} + \frac{p}{p'} \end{aligned} \quad (2.67)$$

By substituting equation (2.67) in (2.63), we get

$$\begin{aligned} \dot{\mu}' &= \left[\frac{Ep^2\mu v_{sw}^c}{c^2p'^3} - \frac{p}{p'^3} \left(\frac{Ev_{sw}^c}{c^2}\right)^2 + \frac{p}{p'} \right] \left[\frac{1}{2L(z)} v(1 - \mu^2) \right] \\ \dot{\mu}' &= \frac{v}{2L(z)} (1 - \mu^2) \frac{Ep^2\mu v_{sw}^c}{c^2p'^3} - \frac{p}{p'^3} \left(\frac{Ev_{sw}^c}{c^2}\right)^2 \frac{v}{2L(z)} (1 - \mu^2) + \frac{v}{2L(z)} (1 - \mu^2) \frac{p}{p'} \\ \dot{\mu}' &= \frac{v}{2L(z)} (1 - \mu^2) \frac{p^3\mu v_{sw}^c}{p'^3c} - \frac{p^3}{p'^3} \left(\frac{v_{sw}^c}{c}\right)^2 \frac{v}{2L(z)} (1 - \mu^2) + \frac{v}{2L(z)} (1 - \mu^2) \frac{p}{p'} \end{aligned}$$

We consider the ratio of $\frac{v_{sw}^c}{c}$ in order 1

$$\dot{\mu}' = \frac{v}{2L(z)} (1 - \mu^2) \frac{p^3 \mu v_{sw}^c}{p'^3 c} + \frac{v}{2L(z)} (1 - \mu^2) \frac{p}{p'^3}$$

From $E = mc^2 = pc = mvc$, we will get

$$v = \frac{E}{mc} = \frac{pc}{mc}$$

Therefore $v = \frac{pc^2}{E}$, and by substituting this in the above equation, we get

$$\begin{aligned} \dot{\mu}' &= \frac{1}{2L(z)} (1 - \mu^2) \left(\frac{pc^2}{E} \right) \frac{\mu v_{sw}^c}{c} + \frac{1}{2L(z)} (1 - \mu^2) \left(\frac{pc^2}{E} \right) \\ \dot{\mu}' &= \frac{1}{2L(z)} (1 - \mu^2) \left[\mu v_{sw}^c + \frac{pc^2}{E} \right] \end{aligned}$$

Taking $\frac{E' v'}{p' c^2} = 1$, and multiplying this by the last term of the above equation, we get

$$\begin{aligned} \dot{\mu}' &= \frac{1}{2L(z)} (1 - \mu^2) \left[\mu v_{sw}^c + \left(\frac{pc^2}{E} \right) \left(\frac{E' v'}{p' c^2} \right) \right] \\ \dot{\mu}' &= \frac{1}{2L(z)} (1 - \mu^2) \left[\mu v_{sw}^c + \left(\frac{E' v'}{E} \right) \right] \end{aligned}$$

And when $p = p'$, then the above equation becomes

$$\dot{\mu}' = \frac{v'}{2L(z)} (1 - \mu^2) \left[\frac{\mu v_{sw}^c}{v'} + \left(\frac{E'}{E} \right) \right]$$

Now by substituting $\frac{E'}{E} = 1 - \frac{\mu v' v_{sw}^c}{c^2}$ in above equation, we get

$$\dot{\mu}' = \frac{v'}{2L(z)} (1 - \mu^2) \left[\frac{\mu v_{sw}^c}{v} + 1 - \frac{\mu' v' v_{sw}^c}{c^2} \right]$$

When $v_{sw}^c = v_{sw} \sec \psi$, the above equation becomes

$$\dot{\mu}' = \frac{v'}{2L(z)} (1 - \mu^2) \left[\frac{\mu v_{sw} \sec \psi}{v} + 1 - \frac{\mu' v' v_{sw} \sec \psi}{c^2} \right]$$

And when $\mu = \mu'$, then the equation becomes

$$\dot{\mu}' = \frac{v}{2L(z)} \left[1 + \frac{\mu v_{sw} \sec \psi}{v} - \frac{\mu v v_{sw} \sec \psi}{c^2} \right] (1 - \mu^2) \quad (2.67)$$

Thus equation (2.67) gives the focusing term of Ruffolo's transport equation (1995,1998).

Consider that momentum perpendicular to magnetic field lines has no effect on particle motion in the solar wind model.

$$\begin{aligned}
 D(p'_\perp) &= 0 \\
 d(p'_\perp) &= d(p'_\perp \sin^2 \theta) \\
 &= d(p'^2(1 - \cos^2 \theta)) \\
 &= d(p'^2(1 - \mu'^2)) \\
 &= p'^2 d(1 - \mu'^2) + (1 - \mu'^2) d(p'^2) \\
 &= p'^2 d(-2\mu') d\mu' + (1 - \mu'^2)(2p') dp' \\
 d\mu' &= -\frac{(1-\mu'^2)(2p') dp'}{(-2\mu') p'^2} \\
 d\mu' &= -\frac{(1-\mu'^2) dp'}{(-\mu') p'} \\
 \dot{\mu}' &= \frac{(1-\mu'^2) dp'}{\mu' p'} \tag{2.68}
 \end{aligned}$$

And equation (2.59) can be rewritten as

$$\frac{\dot{p}'}{p'} = -v_{sw} \left(\cos \psi \frac{d \sec \psi}{dr} \right) \mu'^2$$

By substituting this equation in equation (2.68), we get

$$\dot{\mu}' = -v_{sw} \left(\cos \psi \frac{d}{dr} (\sec \psi) \right) \mu'^{(1-\mu'^2)} \tag{2.69}$$

Thus equation (2.69) clearly indicates that the rate of change of μ is independent of the diverging magnetic field in the solar wind, and it gives the differential convection term of the Ruffolo's transport equation (1995, 1998).

Combining equations (2.67) and (2.69), we can get the rate of change of μ with time t of the focusing term and the differential convection in the transport equation, and it can be represented as follows:

$$\begin{aligned} \dot{\mu} &= \frac{v}{2L(z)} \left[1 + \frac{\mu v_{sw} \sec \psi}{v'} - \frac{\mu v v_{sw} \sec \psi}{c^2} \right] (1 - \mu^2) && \text{Focusing} \\ &- v_{sw} \left(\cos \psi \frac{d}{dr} \sec \psi \right) \mu' (1 - \mu'^2) && \text{Differential Convection} \\ p' &= -p' v_{sw} \left[\frac{\sec \psi}{2L(z)} (1 - \mu^2) - \cos \psi \frac{d(\sec \psi)}{dr} \mu'^2 \right] && \text{Deceleration} \\ \dot{z} &= \underbrace{v' \mu'}_{\text{Streaming}} - \underbrace{\frac{v'^2 \mu'^2}{c^2} v_{sw} \sec \psi + v_{sw} \sec \psi}_{\text{convection}} \end{aligned}$$

First term order and second term order are derived from the Fokker Planck equation as

$$\begin{aligned} \frac{\partial F}{\partial t} + \frac{\partial}{\partial z} \left(\frac{\Delta z}{\Delta t} F \right) + \frac{\partial}{\partial \mu} \left(\frac{\Delta \mu}{\Delta t} F \right) + \frac{\partial}{\partial p} \left(\frac{\Delta p}{\Delta t} F \right) + \frac{\partial}{\partial \mu} \left(\frac{\Delta \mu}{\Delta t} F \right) &= 0 \\ \frac{\partial F(t, \mu, z, p)}{\partial t} &= - \frac{\partial}{\partial z} \left(\frac{\Delta z}{\Delta t} F \right) - \frac{\partial}{\partial \mu} \left(\frac{\Delta \mu}{\Delta t} F \right) - \frac{\partial}{\partial p} \left(\frac{\Delta p}{\Delta t} F \right) + \frac{\partial}{\partial \mu} \left[\frac{\psi \mu}{2} \frac{\partial}{\partial \mu} \left(\frac{E'}{E} F \right) \right] \end{aligned}$$

Pitch angle scattering random term

Employing the fundamental equation of plankton plank, along with different factors brought on by a planet-intermediary, to simulate the motion of high-energy particles emitted from the Sun.

According to the transport equation of Ruffolo (1995), the change in magnetic fluxes and the influence of the solar wind in various considerations will give us the transport equation that describes the passage of the high-energy particle, and the following equations show the precise formulation, and each term is explained in table 3.

$$\begin{aligned}
\frac{\partial \overrightarrow{F}(t, \mu, z, p)}{\partial t} &= -\frac{\partial}{\partial z} \mu v \overrightarrow{F}(t, \mu, z, p) && (\text{streaming}) \\
&- \frac{\partial}{\partial z} \left(1 - \mu^2 \frac{v^2}{c^2} \right) v_{sw} \sec \psi \overrightarrow{F}(t, \mu, z, p) && (\text{convection}) \\
&\frac{\partial}{\partial u} \frac{v}{2L(z)} 1 + \left[1 + \mu \frac{v_{sw}}{v} \sec \psi - \mu \frac{v_{sw} v}{c^2} \sec \psi \right] (1 - \mu^2) \overrightarrow{F} && (\text{focusing}) \\
&+ \frac{\partial}{\partial u} v_{sw} (\cos \psi \frac{d}{dr} \sec \psi) \mu (1 - \mu^2) \overrightarrow{F}(t, \mu, z, p) && (\text{differential convection}) \\
&+ \frac{\partial}{\partial u} \frac{\phi(\mu)}{2} \frac{\partial}{\partial \mu} \left(1 - \mu \frac{v_{sw}}{c^2} \sec \psi \right) \overrightarrow{F}(t, \mu, z, p) && (\text{scattering}) \\
&+ \frac{\partial}{\partial p} p v_{sw} \left[\frac{\sec \psi}{2L(z)} (1 - \mu^2) + \cos \psi \frac{d}{dr} (\sec \psi) \mu^2 \right] \overrightarrow{F}(t, \mu, z, p) && (\text{deceleration})
\end{aligned}$$

Table 3 Description of terms in the transport equation

Terms	Descriptions
1. Streaming	It depicts how particles move in the z-axis magnetic field
2. Convection	it depicts how particles flow along the lines of the magnetic field as a result of solar convection
3. Focusing	It depicts the movement of particles as a result of the adiabatic focusing taken into account in both the solar wind frame and the stationary reference frame
4. Differential convection	It depicts that the solar velocity varies with position. By taking into account the rate of change relative to time t in the context of the solar wind, which has no bearing on focusing
5. Scattering	It depicts the way that particles scatter randomly inside the structure of the solar wind
6. Deceleration	It depicts the rate at which momentum changes in relation to velocity changes along the magnetic field lines in the solar wind frame

CHAPTER III

RESEARCH METHODOLOGY

The methods for simulating the movement of particles from the Sun's eruption along the magnetic field lines to Earth are presented in this chapter, and it also covers the simulation techniques and tools that we employed. This study determines the space weather at the beginning of the 25th solar cycle by analyzing the time period of high-energy particles and the intensity profile of solar energetic particles reaching Earth after the Sun erupts and comparing it to the space environment. The specifics are listed below.

3.1 Research Tools

In this study, we used two different types of research tools.

3.1.1 The Data from the ACE spacecraft

The ACE spacecraft, part of NASA's Explorer program, investigates energetic particles that travel from the Sun to Earth at L1 Lagrange point, some 1.5 million kilometers away, and it is the location where the gravitational pull of Earth and the Sun are evenly distributed. ACE offers space weather data and alerts for geomagnetic storms that could damage astronauts in orbit and interfere with communications on Earth. We primarily used the SIS instrument on the ACE spacecraft to gather data, which was then uploaded online and made openly accessible to researchers. We downloaded the data from the website; <https://izw1.caltech.edu/ACE/>.

3.1.2 Ruffolo's transport equation to simulate particle motion in a C program.

The particle motion was simulated using Ruffolo's transport equation, which was then processed by the operating system using the C programming language. There are nine programs in total:

1. wind.c is the main program used to simulate the motion of particles. It receives variables from the simulated data and retrieve files from other programs. The variables used to simulate motion of the particle were saved in the file named in, with the following contents:

starts: the simulation's initial distance (AU)

stops: the simulation's final distance (AU)

s.step: the increase in distance (AU)

prints: the printing between the distance (AU)

nmu: the μ points

length: the simulation length (AU)

p: the number of momentum

p[1 ... np]: each energy's momentum

m: the particle's mass

beta of sw: the speed ratio of solar wind and light

lambda (λ): The mean free path

q: the particle scattering index

printextra: the information printing command

2. decel.c is a program to process Ruffolo's particle transport equation's gradual decomposition
3. field.c is a program to examine particle's motion along the magnetic field. The scattering coefficient will be calculated in relation to magnetic field flare-up and the impact of solar wind on the interplanetary medium.
4. initial.c is a program that determines the particle distribution source for processing particle motion simulation by comparing the maximum particle distribution in the least energy to the default value. The flux at higher energy levels is correspondingly computed to estimate the maximum flux at each energy level due to the enormous number of particles.
5. inject.c is a program to compute particle release.
6. nutil.c is a program for reservation of space in memory.
7. printout.c is a program to display important data.
8. stream.c is a program that considers how the convection of the solar wind affects the passage of particles along the z-axis.
9. tridag.c is a program for solving matrix equations.

3.2 The Numerical methods used in this research

Ruffolo's transport equation served as the central equation in this study. The Ruffolo's transport equation (1995, 1998) is a partial differential equation (PDE) with a large number of independent variables. Consequently, it is difficult to obtain the answer directly. However, because the equation is a PDE and the boundary conditions are known, the solution can be found using the finite difference method. Generally, the particles will flow, as shown in figure 22. We used the following three ways to find the solution:

1. Explicit method
2. Implicit method and
3. Crank-Nicholson method

When $f(x_i, t_n)$, then from the particle diffusion equation, we get

$$\frac{\partial f}{\partial t} = -\frac{\partial s}{\partial x} \quad (3.1)$$

Where:

$$S = -D \frac{\partial f}{\partial x} \quad (3.2)$$

Substituting equation (3.2) into equation (3.1), we obtained:

$$\frac{\partial f}{\partial t} = -\frac{\partial}{\partial x} \left(-D \frac{\partial f}{\partial x} \right) = D \frac{\partial^2 f}{\partial^2 x}$$

Where:

s : number of particles moving through a point in time t (flux)

f : the particle flux

D : the diffusion coefficient

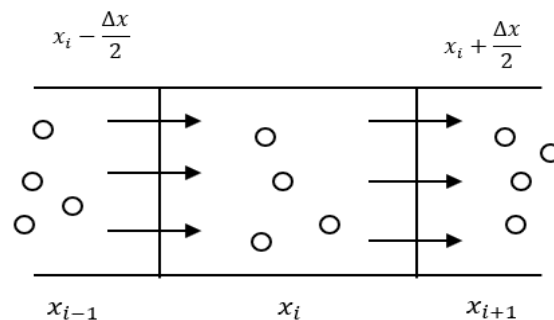


Figure 22 The flow of particles through cells

We know that:

Net number of particles = inflow particles – outflow particles

$$\frac{\partial}{\partial t} (f \cdot \Delta x) = s \left(x_i - \frac{\Delta x}{2} \right) - s \left(x_i + \frac{\Delta x}{2} \right) \quad (3.3)$$

Particle flow rate is given by:

$$\frac{\partial f}{\partial t} = \frac{f^{n+1}(x_i) - f^n(x_i)}{\Delta t} = \frac{s \left(x_i - \frac{\Delta x}{2} \right) - s \left(x_i + \frac{\Delta x}{2} \right)}{\Delta x} \quad (3.4)$$

And $n = 0, 1, 2, \dots$

$$\frac{f^{n+1}(x_i) - f^n(x_i)}{\Delta t} = \frac{-D \left(x_i - \frac{\Delta x}{2} \right) [f(x_i) - f(x_{i-1})] + D \left(x_i + \frac{\Delta x}{2} \right) [f(x_{i+1}) - f(x_i)]}{(\Delta x)^2}$$

We know;

$$r = \frac{D\Delta t}{(\Delta x)^2}$$

Where; x (distance) = 1

$$\begin{aligned} f^{n+1}(x_i) - f^n(x_i) &= -r[f(x_i) - f(x_{i-1})] + r[f(x_{i+1}) - f(x_i)] \\ &= -rf(x_i) + rf(x_{i-1}) + rf(x_{i+1}) - rf(x_i) \\ f^{n+1}(x_i) &= f^n(x_i) + r[f(x_{i-1}) - 2f(x_i) + f(x_{i+1})] \end{aligned} \quad (3.5)$$

3.2.1 The Explicit method

The principle is to assign $n + 1$ to the new value as time goes on, where n is the old value at the start time and set all of the f power to n in the left-hand expression of the equation (3.5). This puts all the old values on the right-hand side of the equation (3.5).

Thus equation (3.5) becomes

$$f^{n+1}(x_i) = rf^n(x_{i-1}) + (1 - 2r)f^n(x_i) + rf^n(x_{i+1}) \quad (3.6)$$

And $i = 1, 2, 3, \dots, N - 1$

Using the matrix method and substituting the value of i , the equation (3.6) can be solved as follows.

$$\begin{aligned}
 i = 1; \quad f^{n+1}(x_1) &= rf^n(x_0) + (1 - 2r)f^n(x_1) + rf^n(x_2) \\
 i = 2; \quad f^{n+1}(x_2) &= rf^n(x_1) + (1 - 2r)f^n(x_2) + rf^n(x_3) \\
 i = 3; \quad f^{n+1}(x_3) &= rf^n(x_2) + (1 - 2r)f^n(x_3) + rf^n(x_4) \\
 &\vdots \\
 i = N - 1; \quad f^{n+1}(x_{N-1}) &= rf^n(x_{N-2}) + (1 - 2r)f^n(x_{N-1}) + rf^n(x_N)
 \end{aligned}$$

Error analysis

From the initial equation

$$f^{n+1}(x_i) - f^n(x_i) = r[f(x_{i-1}) - 2f(x_i) + f(x_{i+1})]$$

We know,

$$f(x_{i-1}) - 2f(x_i) + f(x_{i+1})$$

Using the Taylor series distribution method:

$$f(x_{i-1}) = f(x_{i-1}) \tag{3.7}$$

$$f(x_i) = f(x_{i-1}) + \Delta x f'(x_{i-1}) + \frac{(\Delta x)^2 f''(x_{i-1})}{2} + \frac{(\Delta x)^3 f'''(x_{i-1})}{6} + \dots \tag{3.8}$$

$$f(x_{i+1}) = f(x_{i-1}) + 2\Delta x f'(x_{i-1}) + \frac{(2\Delta x)^2 f''(x_{i-1})}{2} + \frac{(2\Delta x)^3 f'''(x_{i-1})}{6} + \dots \tag{3.9}$$

By substituting equations (3.7), (3.8), and (3.9) in $f(x_{i-1}) - 2f(x_i) + f(x_{i+1})$ We will get

$$\begin{aligned}
 f(x_{i-1}) - 2f(x_i) + f(x_{i+1}) &= f(x_{i-1}) - 2f(x_{i-1}) - 2\Delta x f'(x_{i-1}) - (\Delta x)^2 f''(x_{i-1}) \\
 &\quad - \frac{1}{3}(\Delta x)^3 f'''(x_{i-1}) + \dots + f(x_{i-1}) + 2\Delta x f'(x_{i-1}) \\
 &\quad + 2(\Delta x)^2 f''(x_{i-1}) + \frac{2}{3}(\Delta x)^3 f'''(x_{i-1}) + \dots \tag{3.10}
 \end{aligned}$$

Thus,

$$\begin{aligned} f(x_{i-1}) - 2f(x_i) + f(x_{i+1}) \\ \approx -(\Delta x)^2 f''(x_{i-1}) - \frac{1}{3}(\Delta x)^3 f'''(x_{i-1}) + \dots + 2(\Delta x)^2 f''(x_{i-1}) \\ + \frac{2}{3}(\Delta x)^3 f'''(x_{i-1}) + \dots \end{aligned}$$

Finally;

$$f(x_{i-1}) - 2f(x_i) + f(x_{i+1}) \approx f''(x_{i,t}) + O(\Delta x)^2$$

When $O(\Delta x)^2$ denotes the 2nd order error in the initial equation evaluated in the expression $f^{n+1}(x_i) - f^n(x_i)$.

$$f^{n+1}(x_i) - f^n(x_i) = \frac{D\Delta t}{(\Delta x)^2} [f(x_{i-1}) - 2f(x_i) + f(x_{i+1})]$$

$$r = \frac{D\Delta t}{(\Delta x)^2}$$

$$\frac{f^{n+1}(x_i) - f^n(x_i)}{\Delta t} = \frac{\partial f(x_i)}{\partial t}$$

Therefore,

$$\frac{f^{n+1}(x_i) - f^n(x_i)}{\Delta t} = \frac{\partial f(x_i)}{\partial t} \approx O(\Delta t)$$

As a result, the error is $O(\Delta t)$, and the equation is:

$$\mathbf{error} \propto \mathbf{O}(\Delta t) + \mathbf{O}(\Delta x)^2 \quad (3.11)$$

3.2.2 The Implicit methods

The principal idea is to assign $n+1$ to the new values as time increases in equation (3.5), where n is the initial value and set $n+1$ to all powers of f .

Then the equation (3.5) becomes

$$f^{n+1}(x_i) - f^n(x_i) = r[f^{n+1}(x_{i-1}) - 2f^{n+1}(x_i) + f^{n+1}(x_{i+1})]$$

$$f^n(x_i) = f^{n+1}(x_i) - rf^{n+1}(x_{i-1}) + 2rf^{n+1}(x_i) - rf^{n+1}(x_{i+1})$$

$$\therefore f^n(x_i) = -rf^{n+1}(x_{i-1}) + (1 + 2r)f^{n+1}(x_i) - rf^{n+1}(x_{i+1}) \quad (3.12)$$

Where $i = 1, 2, 3, \dots$

Using the matrix method to solve equation (3.12), and by substituting the value of i in each equation, and we will get

$$\begin{aligned}
 i = 1, & \quad -rf^{n+1}(x_0) + (1 + 2r)f^{n+1}(x_1) - rf^{n+1}(x_2) &= f^n(x_1) \\
 i = 2, & \quad -rf^{n+1}(x_1) + (1 + 2r)f^{n+1}(x_2) - rf^{n+1}(x_3) &= f^n(x_2) \\
 i = 3, & \quad -rf^{n+1}(x_2) + (1 + 2r)f^{n+1}(x_3) - rf^{n+1}(x_4) &= f^n(x_3) \\
 & \quad \vdots \\
 i = N - 1, & \quad -rf^{n+1}(x_{N-2}) + (1 + 2r)f^{n+1}(x_{N-1}) - rf^{n+1}(x_N) &= f^n(x_{N-1})
 \end{aligned}$$

The matrix form will be:

$$\begin{pmatrix}
 (1 + 2r) & -r & 0 & \cdots & 0 \\
 -r & (1 + 2r) & -r & \ddots & \vdots \\
 0 & -r & (1 + 2r) & -r & 0 \\
 \vdots & \ddots & \ddots & \ddots & \vdots \\
 0 & \cdots & 0 & -r & (1 + 2r)
 \end{pmatrix}
 \begin{pmatrix}
 f^{n+1}(x_1) \\
 f^{n+1}(x_2) \\
 f^{n+1}(x_3) \\
 \vdots \\
 f^{n+1}(x_{N+1})
 \end{pmatrix}
 =
 \begin{pmatrix}
 rf^{n+1}(x_0) + f^n(x_1) \\
 f^n(x_2) \\
 f^n(x_3) \\
 \vdots \\
 f^n(x_{N+1})
 \end{pmatrix}$$

We used the Taylor series distribution method to calculate the difference, and the final equation will be the same as the explicit method, i. e

$$\text{error} \propto \mathbf{O}(\Delta t) + \mathbf{O}(\Delta x)^2 \quad (3.13)$$

3.2.3 The Crank-Nicolson method

This method combines explicit and implicit methods.

As

$$r = \frac{D\Delta t}{(\Delta x)^2}$$

Since

$$r = 2S$$

$$f^{n+1}(x_i) = rf^n(x_{i-1}) + (1 - 2r)f^n(x_i) + rf^n(x_{i+1}) \quad (3.14)$$

And from the implicit methods (equation 3.12), we got the following

$$f^n(x_i) = -rf^{n+1}(x_{i-1}) + (1 + 2r)rf^{n+1}(x_i) - rf^{n+1}(x_{i+1}) \quad (3.15)$$

Adding equations (3.14) and (3.15) we will get

$$-rf^{n+1}(x_{i-1}) + (2 + 2r)rf^{n+1}(x_i) - rf^{n+1}(x_{i+1}) = rf^n(x_{i-1}) + (2 - 2r)f^n(x_i) + rf^n(x_{i+1})$$

Substituting $r = 2S$ and dividing by 2 throughout the above equation, we get:

$$-Sf^{n+1}(x_{i-1}) + (1 + 2S)f^{n+1}(x_i) - Sf^{n+1}(x_{i+1}) = Sf^n(x_{i-1}) + (1 - 2S)f^n(x_i) + Sf^n(x_{i+1}) \quad (3.16)$$

Where $i = 1, 2, 3, \dots, N - 1$

Using matrix method to solve equation (3.16) and by substituting value of i , we will get

$$i = 1, -Sf^{n+1}(x_0) + (1 + 2S)f^{n+1}(x_1) - Sf^{n+1}(x_2) = Sf^n(x_0) + (1 - 2S)f^n(x_1) + Sf^n(x_2)$$

$$i = 2, -Sf^{n+1}(x_1) + (1 + 2S)f^{n+1}(x_2) - Sf^{n+1}(x_3) = Sf^n(x_1) + (1 - 2S)f^n(x_2) + Sf^n(x_3)$$

$$i = 3, -Sf^{n+1}(x_2) + (1 + 2S)f^{n+1}(x_3) - Sf^{n+1}(x_4) = Sf^n(x_2) + (1 - 2S)f^n(x_3) + Sf^n(x_4)$$

\vdots

$$i = N - 1, -Sf^{n+1}(x_{N-2}) + (1 + 2S)f^{n+1}(x_{N-1}) - Sf^{n+1}(x_N) = Sf^n(x_{N-2}) + (1 - 2S)f^n(x_{N-1}) + Sf^n(x_N)$$

And the matrix formed is:

$$\begin{pmatrix} (1 + 2S) & -S & 0 & \dots & 0 \\ -S & (1 + 2S) & -S & \ddots & \vdots \\ 0 & -S & (1 + 2S) & -S & 0 \\ \vdots & \ddots & \ddots & \ddots & \ddots \\ 0 & \dots & 0 & -S & (1 + 2S) \end{pmatrix} \begin{pmatrix} f^{n+1}(x_1) \\ f^{n+1}(x_2) \\ f^{n+1}(x_3) \\ \vdots \\ f^{n+1}(x_{N+1}) \end{pmatrix} =$$

$$\begin{pmatrix} (1 - 2S) & S & 0 & \dots & 0 \\ S & (1 - 2S) & S & \ddots & \vdots \\ 0 & S & (1 - 2S) & S & 0 \\ \vdots & \ddots & \ddots & \ddots & \ddots \\ 0 & \dots & 0 & S & (1 - 2S) \end{pmatrix} \begin{pmatrix} f^{n+1}(x_1) \\ f^{n+1}(x_2) \\ f^{n+1}(x_3) \\ \vdots \\ f^{n+1}(x_{N+1}) \end{pmatrix}$$

$$+ \begin{pmatrix} S[f^{n+1}(x_0) + f^n(x_1)] \\ f^n(x_2) \\ f^n(x_3) \\ \vdots \\ f^n(x_{N+1}) \end{pmatrix}$$

Because this method combines the explicit and implicit methods, the total error is presented as:

$$\mathbf{error} \propto \mathbf{O}(\Delta t)^2 + \mathbf{O}(\Delta x)^2 \quad (3.17)$$

3.3 Selecting an event at the beginning of the 25th solar cycle

We studied the physics of solar eruptions, particularly the movement of high-energy solar particles collected by the ACE spacecraft. Based on the alterations and phenomena caused by the intensity of particles traveling to Earth, the events of interest are selected. We have selected the two strongest solar events, one on 29 November 2020 and another on 3 July 2021. They are the most powerful flares beginning the 25th solar cycle, with X-ray intensities of M4.4 and X1.59, respectively. The eruptions are positioned in S23E98 and N24W88, respectively, with solar wind speeds of 402.1 km/s and 517 km/s. We chose to analyze the density data obtained by the ACE spacecraft on He, N, C, O, and Fe particles. Tables 4 and 5 below present the physical characteristics of the selected events.

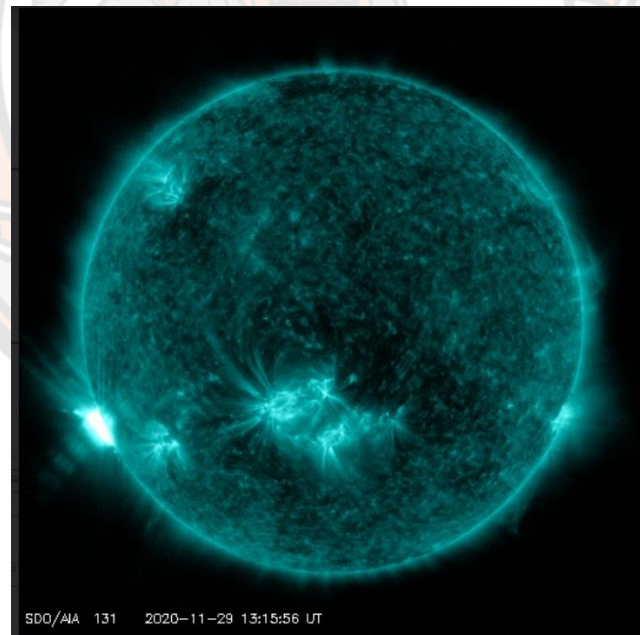
Table 4 The Physical characteristics of the event on 29 November 2020

Physical characteristics	Details
Solar cycle	25 th cycle
Radiation level	M4.4
The eruption began	12:34 UT
End of the eruption time	13:41 UT
Eruption duration	67 Minutes
Eruption position	S23E98
Solar wind speed	402 km/s

Table 5 The Physical characteristics of the event on 3 July 2021

Physical characteristics	Details
Solar cycle	25 th cycle
Radiation level	X1.59
The eruption began	14:18 UT
End of the eruption time	14:34 UT
Eruption duration	16 Minutes
Eruption position	N24W88
Solar wind speed	517 km/s

The first powerful solar eruption in the last three years, after the onset of the 25th solar cycle, exploded on 29 November 2020 from the Sun's surface. The eruption was associated with a powerful medium-class flare of X-ray intensity M4.4, which began at 12:34 UT and ended at 13:41 UT, exploding for 17 minutes. Figure 23 shows the intense particle that has erupted from the AR12790.

**Figure 23 The solar eruption on 29 November 2020**

Source: <https://www.spaceweatherlive.com/en/archive/2020/11/29/xray.html>

Another high-intensity X-ray with an intensity of X1.59 erupted at the beginning of the 25th solar cycle on 3 July 2021. The eruption lasted 16 minutes, beginning at 14:18 UT and ending at 14:34 UT. The eruption peaked at 14:29 UT and was the cycle's first X-class solar flare. It occurred at AR2835 on the Sun's northwest limb, as depicted in figure 24.

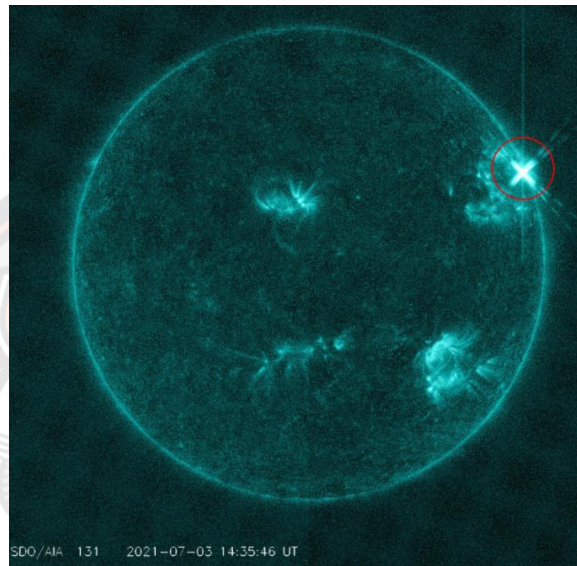


Figure 24 The solar eruption on 3 July 2021

Source: <https://www.spaceweatherlive.com/en/archive/2021/07/03/xray.html>

The Sun produces a continual stream of charged particles toward Earth over time. Therefore, we evaluated at the flux values of particles measured by the SIS instrument on the ACE spacecraft for helium, carbon, nitrogen, oxygen, and iron particles. The Ruffolo (1995, 1998) transport equation was solved in C using the Ubuntu operating system to model the transportation of high-energy particles from the Sun along Archimedian magnetic field lines employing the number of particles per unit time.

3.4 Kp-index on the selected events

Solar flares are categorized according to their X-ray brightness in the 1 to 8 Angstrom wavelength range. Classes A, B, C, M, and X. Significant X-class flares can result in long-lasting radiation storms and global radio blackouts. GOES, a geostationary satellite, makes these measurements. The X-ray severity values are shown in figures 25 and 26.

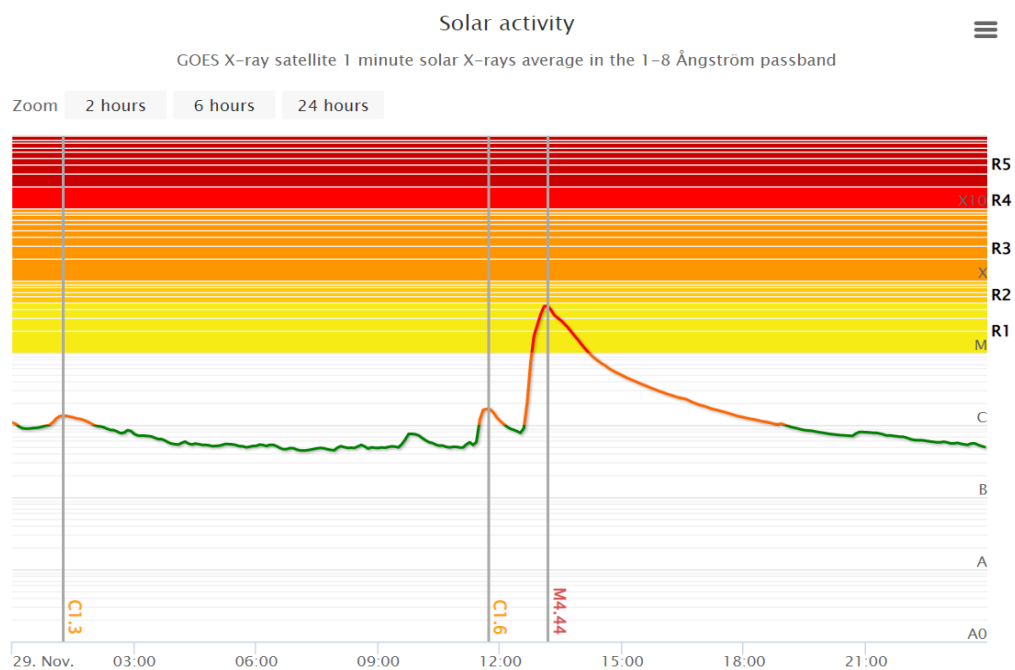


Figure 25 X-ray severity values on 29 November 2020

Source: <https://www.spaceweatherlive.com/en/archive/2020/11/29/xray.html>

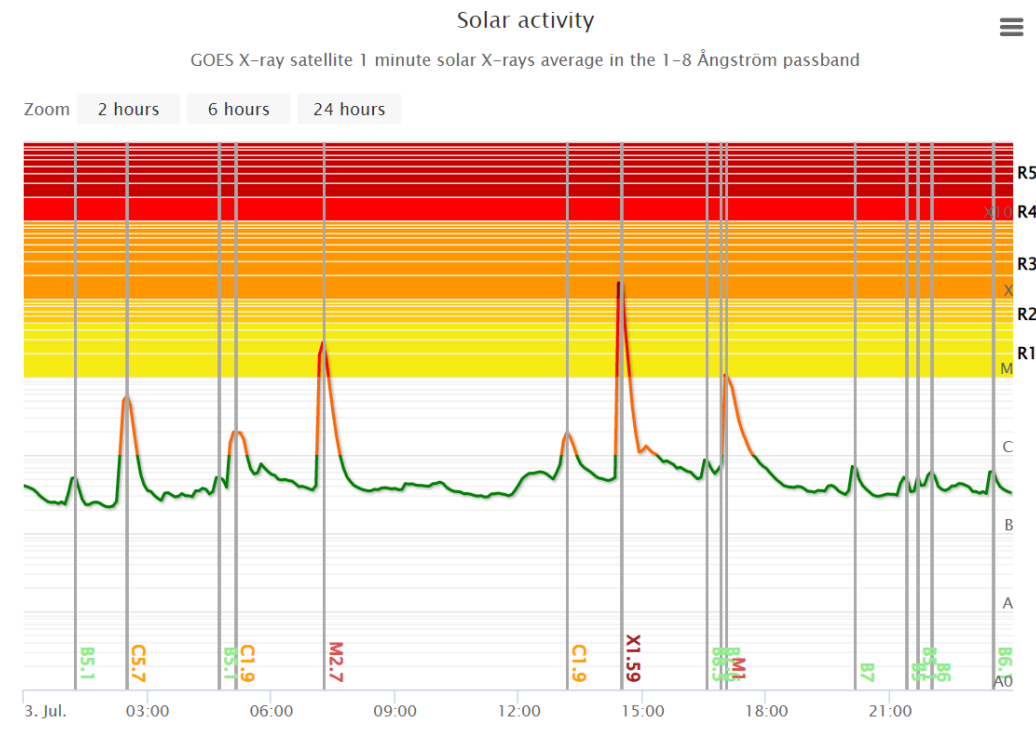


Figure 26 X-ray severity values on 3 November 2021

Source: <https://www.spaceweatherlive.com/en/archive/2021/07/03/xray.html>

The Kp-index, which ranges from 0 to 9, indicates disturbances in the horizontal component of the Earth's magnetic field, with 1 indicating calm and ≥ 5 signaling a geomagnetic storm. The graphs depict the kp-index on events observed within 3 hours by the GOES satellite. The graphs (figures 27 and 28) indicate that the estimated kp-index is less than 2 in both incidents, indicating that the effect on Earth's livelihood is minimal. Nevertheless, according to some sources, it increased solar energetic proton radiation, which could harm astronauts if not shielded. They also interfered with some GPS and communication signals, however, not to the extent that it resulted in radio communication blackouts.

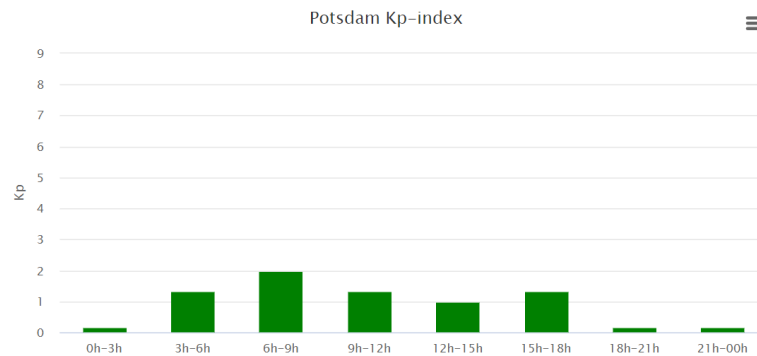


Figure 27 Kp index on 29 November 2020 as detected by NOAA GOES satellite

Source: <https://www.spaceweatherlive.com/en/archive/2020/11/29/kp.html>

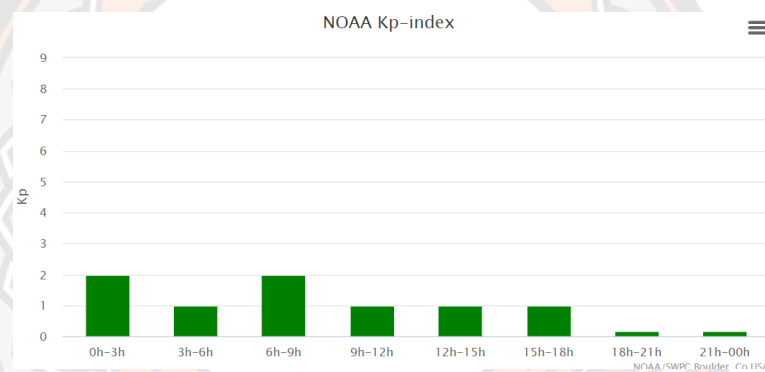


Figure 28 Kp index on 3 July 2021 as detected by NOAA GOES satellite

Source: <https://www.spaceweatherlive.com/en/archive/2021/07/03/kp.html>

3.5 The collection of Data from ACE spacecraft through SIS instrument

The current study is based on data collected from ACE spacecraft and measured by SIS. We downloaded data on the day of the solar eruption and then prepared the required initial values for the simulation of particle motion. We have used the following steps to download the data.

1. Entered the website 'www.srl.caltech.edu/ACE,' and the following page was displayed as shown in figure 29. Then selected *online data*.

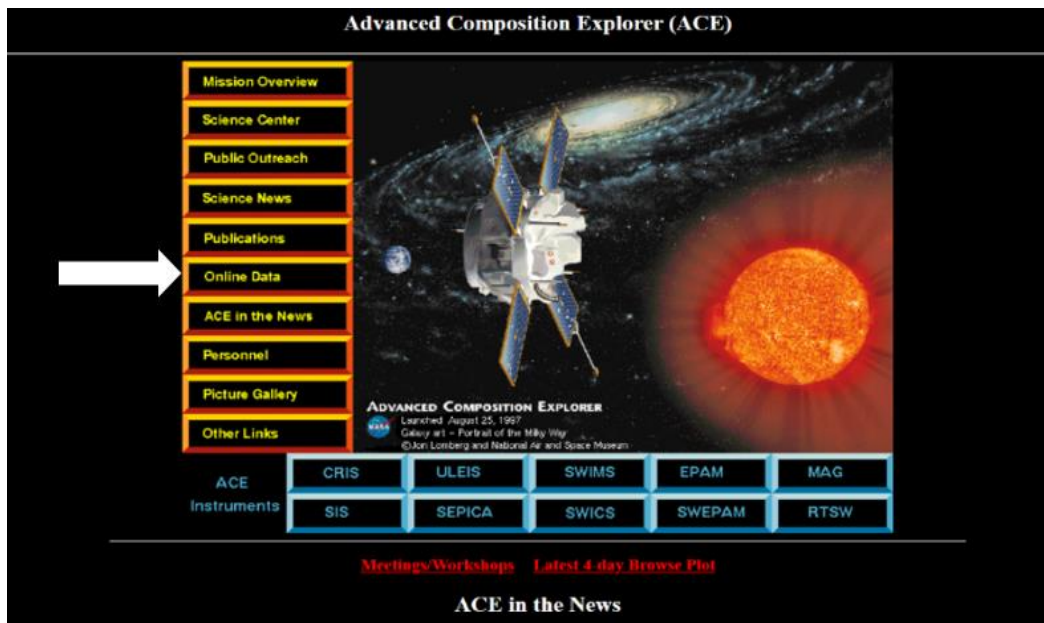


Figure 29 The home page of the website

Source: <https://izw1.caltech.edu/ACE/>

2. Selected 'Verified / Level2' as in figure 30 to get data from different instruments on spacecraft.

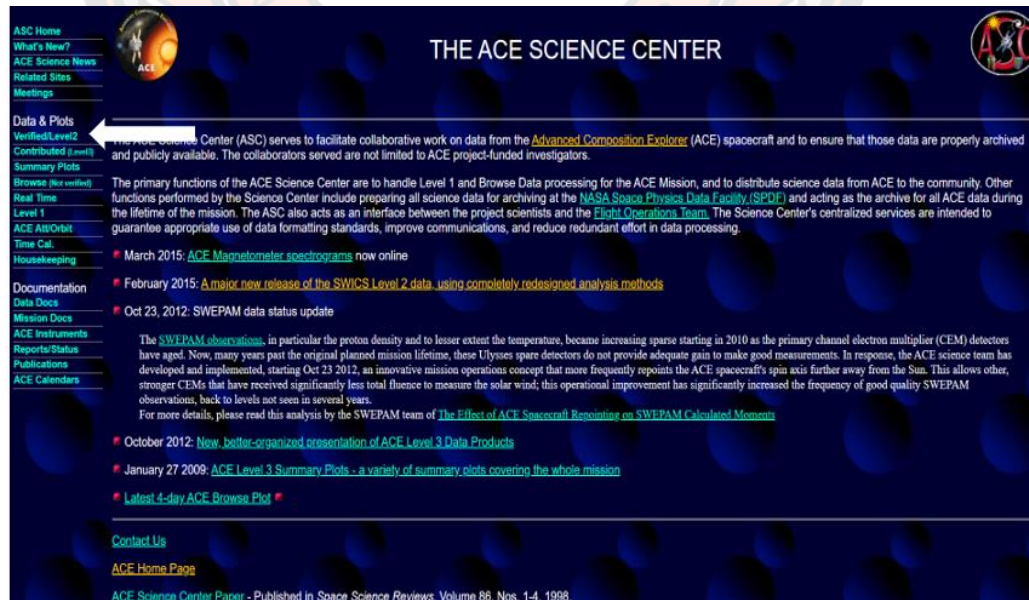


Figure 30 The webpage to get the main data

Source: <https://izw1.caltech.edu/ACE/ASC/>

3. Selected SIS Data as indicated in figure 31.

ACE Level 2 (Verified) Data

You might like to try our [New ACE Level 2 data server \(beta-test\)](#)

[ACE Level 2 Data Policy](#)

Interplanetary Magnetic Field Parameters: MAG.	MAG Data	Documentation
Solar Wind Parameters: SWEPAM	SWEPAM Data	Documentation
Solar Wind Temperatures, Speeds, Composition, Charge States: SWICS prior to August 23 2011	SWICS 1.1 Data	Documentation
Solar Wind Temperatures, Speeds, Composition, Charge States: SWICS after August 23 2011	SWICS 2.0 Data	Documentation
Solar Wind Proton density and speed: SWICS	SWICS Proton Data	Documentation
Solar Suprathermal and Energetic Particle Intensities: ULEIS	ULEIS Data	Documentation
Solar Energetic Particle Intensities: EPAM	EPAM Data	Documentation
Solar Energetic Particle Intensities: SEPICA	SEPICA Data	Documentation
SEP, GCR, and ACR Intensities: SIS.	SIS Data	Documentation
Galactic Cosmic Ray Intensities: CRIS	CRIS Data	Documentation
Merged IMF and Solar Wind 64-second Averages	MAG/SWEPAM Data	Documentation
Merged IMF, Solar Wind, and Energetic Particle Hourly Averages	Multi-instrument Data	Documentation

[Autosubscription Guidelines](#) [Data Processing Changing](#)

[Data Inventory Graph](#) [Register at ACE Data User](#)

Note: Most of these data are also available from [CDAWeb](#). Level 2 data for each instrument are delivered to CDAWeb when we have confidence in the stability of the data set.

Figure 31 The type of data selection

Source: <https://izw1.caltech.edu/ACE/ASC/level2/index.html>

4. Selected day of year of chosen events

In the Hourly Averages field, enter the date range for required information. This study investigated the eruption events on 29 November 2020 and 3 July 2021. The day of the year (DOY) is calculated as 334 and 184, respectively. As a result, we chose 331/2020 – 357/2020 and 181/2021–207/2021. Then, as shown in Figures 32, press GO to begin downloading.

ACE SIS Level 2 Data

You might like to try our [New ACE Level 2 data server \(beta-test\)](#)

Solar Energetic Particle, Low Energy Galactic Cosmic Ray, and Anomalous Cosmic Ray Fluxes

256-second Averages (Yearly Data Files)

Year 2022
Year 2021
Year 2020
Year 2019

Hourly Averages (27-day Bartels rotations DOY/Year)

2557	19/2021 - 45/2021
2556	358/2020 - 18/2021
2555	331/2020 - 357/2020
2554	304/2020 - 330/2020

Daily Averages (27-day Bartels rotations DOY/Year)

Full Data Range	226/1997 - 4/2022
2569	343/2021 - 4/2022
2568	316/2021 - 342/2021
2567	289/2021 - 315/2021

Figure 32 The DoY of the selected event (29/11/2020)

Source: https://izw1.caltech.edu/ACE/ASC/level2/lv12DATA_SIS.html

5. Selection of the required elements for the simulation

We analyzed He, C, N, O, and Fe, so we have selected these elements and their counts to download, as shown in figure 33. The desired date range was then entered in the Starting and Ending boxes. We choose starting YR/DOY as 20/331 and ending YR/DOY as 20/343 for the event on 29 November 2020 and 21/181 to 21/196 for the event on 3 July 2021, respectively, as their DOYs are 334 and 184. The data file for the simulation was then downloaded after choosing the "Text file download box" and "Retrieve data" options.

SIS Hourly Averaged Element Fluxes.

Select the data items you want to retrieve.

Click on items in first column for more information.

Note: Data for each element consists of particle fluxes in 8 energy ranges.

Time (UT)	<input type="checkbox"/> year	<input type="checkbox"/> day	<input type="checkbox"/> hour	<input type="checkbox"/> min	<input type="checkbox"/> sec	<input type="checkbox"/> year (float)	<input type="checkbox"/> day (float)	<input type="checkbox"/> ACE epoch
Element Fluxes	<input checked="" type="checkbox"/> He	<input checked="" type="checkbox"/> C	<input checked="" type="checkbox"/> N	<input checked="" type="checkbox"/> O	<input type="checkbox"/> Ne	<input type="checkbox"/> Na	<input type="checkbox"/> Mg	<input type="checkbox"/> Al
	<input type="checkbox"/> Si	<input type="checkbox"/> S	<input type="checkbox"/> Ar	<input type="checkbox"/> Ca	<input type="checkbox"/> Fe	<input type="checkbox"/> Ni		
Element Counts	<input checked="" type="checkbox"/> He cnt	<input checked="" type="checkbox"/> C cnt	<input checked="" type="checkbox"/> N cnt	<input checked="" type="checkbox"/> O cnt	<input type="checkbox"/> Ne cnt	<input type="checkbox"/> Na cnt	<input type="checkbox"/> Mg cnt	<input type="checkbox"/> Al cnt
	<input type="checkbox"/> Si cnt	<input type="checkbox"/> S cnt	<input type="checkbox"/> Ar cnt	<input type="checkbox"/> Ca cnt	<input checked="" type="checkbox"/> Fe cnt	<input type="checkbox"/> Ni cnt		
Other Info	<input type="checkbox"/> uptime fraction		<input type="checkbox"/> solar activity					

or [check here to select all the data \(over 100 columns!\)](#)

Starting "YR/DOY": Ending "YR/DOY": (Example: **98/37**, note: no leading zeros)

Choose Data Format: X-Y Plot Text file download Text on Screen

Figure 33 A web page showing selected elements and their counts

Source: <https://izw1.caltech.edu/cgi-bin/dib/rundibviewsis12/ACE/ASC/DATA/level2/>

3.6 Preparation of spacecraft data for simulation in the C program

To prepare data for the simulation in the C program, we followed the processes outlined below. To demonstrate the techniques, we have only shown sample data for Helium particles. Nonetheless, we followed comparable techniques for all of the elements chosen. Table 6 displays sample data from the SIS instrument on the ACE spacecraft for the He element of the event that occurred on 29 November 2020.

Table 6 Data sample collected for Helium particles at all energy levels

Time(min)	He1	He2	He3	He4	He5	He6	He7	He8	CNT1	CNT2	CNT3	CNT4	CNT5	CNT6	CNT7	CNT8
30	2.67E-05	7.74E-05	0.00E+00	0.00E+00	9.39E-06	-1.00E+03	-1.00E+03	-1.00E+03	1.00E+00	3.00E+00	0.00E+00	0.00E+00	1.00E+00	0.00E+00	0.00E+00	0.00E+00
90	0.00E+00	4.71E-05	9.96E-05	1.48E-05	3.91E-05	-1.00E+03	-1.00E+03	-1.00E+03	0.00E+00	2.00E+00	3.00E+00	1.00E+00	4.00E+00	0.00E+00	0.00E+00	0.00E+00
150	7.83E-05	9.91E-05	6.70E-05	6.07E-05	6.97E-05	-1.00E+03	-1.00E+03	-1.00E+03	3.00E+00	4.00E+00	2.00E+00	4.00E+00	7.00E+00	0.00E+00	0.00E+00	0.00E+00
210	0.00E+00	4.84E-05	3.10E-05	7.04E-05	0.00E+00	-1.00E+03	-1.00E+03	-1.00E+03	0.00E+00	2.00E+00	1.00E+00	5.00E+00	0.00E+00	0.00E+00	0.00E+00	0.00E+00
270	4.94E-05	0.00E+00	0.00E+00	0.00E+00	9.39E-06	-1.00E+03	-1.00E+03	-1.00E+03	2.00E+00	0.00E+00	0.00E+00	0.00E+00	1.00E+00	0.00E+00	0.00E+00	0.00E+00
330	7.97E-05	7.01E-05	6.85E-05	4.43E-05	1.01E-05	-1.00E+03	-1.00E+03	-1.00E+03	3.00E+00	3.00E+00	2.00E+00	3.00E+00	1.00E+00	0.00E+00	0.00E+00	0.00E+00
390	0.00E+00	4.81E-05	2.90E-05	5.79E-05	2.78E-05	-1.00E+03	-1.00E+03	-1.00E+03	0.00E+00	2.00E+00	1.00E+00	4.00E+00	3.00E+00	0.00E+00	0.00E+00	0.00E+00
450	8.09E-05	2.23E-05	1.01E-04	1.42E-05	1.95E-05	-1.00E+03	-1.00E+03	-1.00E+03	3.00E+00	1.00E+00	3.00E+00	1.00E+00	2.00E+00	0.00E+00	0.00E+00	0.00E+00
510	2.41E-05	4.76E-05	2.96E-05	0.00E+00	6.87E-05	-1.00E+03	-1.00E+03	-1.00E+03	1.00E+00	2.00E+00	1.00E+00	0.00E+00	7.00E+00	0.00E+00	0.00E+00	0.00E+00
570	1.03E-04	9.93E-05	5.67E-05	0.00E+00	2.04E-05	-1.00E+03	-1.00E+03	-1.00E+03	4.00E+00	4.00E+00	2.00E+00	0.00E+00	2.00E+00	0.00E+00	0.00E+00	0.00E+00
630	2.52E-05	2.61E-05	0.00E+00	8.61E-05	8.81E-06	-1.00E+03	-1.00E+03	-1.00E+03	1.00E+00	1.00E+00	0.00E+00	6.00E+00	1.00E+00	0.00E+00	0.00E+00	0.00E+00
690	2.52E-05	2.49E-05	6.26E-05	1.45E-05	5.78E-05	-1.00E+03	-1.00E+03	-1.00E+03	1.00E+00	1.00E+00	2.00E+00	1.00E+00	6.00E+00	0.00E+00	0.00E+00	0.00E+00
750	2.64E-05	2.61E-05	3.15E-05	4.29E-05	3.85E-05	-1.00E+03	-1.00E+03	-1.00E+03	1.00E+00	1.00E+00	1.00E+00	3.00E+00	4.00E+00	0.00E+00	0.00E+00	0.00E+00
810	2.18E-05	0.00E+00	2.66E-05	1.35E-05	9.39E-06	-1.00E+03	-1.00E+03	-1.00E+03	1.00E+00	0.00E+00	1.00E+00	1.00E+00	1.00E+00	0.00E+00	0.00E+00	0.00E+00
870	5.72E-05	4.71E-05	2.83E-05	0.00E+00	4.85E-05	-1.00E+03	-1.00E+03	-1.00E+03	2.00E+00	2.00E+00	1.00E+00	0.00E+00	5.00E+00	0.00E+00	0.00E+00	0.00E+00
930	7.46E-05	6.92E-05	8.53E-05	4.49E-05	5.53E-05	-1.00E+03	-1.00E+03	-1.00E+03	3.00E+00	3.00E+00	3.00E+00	3.00E+00	6.00E+00	0.00E+00	0.00E+00	0.00E+00
990	5.08E-05	0.00E+00	5.87E-05	6.08E-05	3.99E-05	-1.00E+03	-1.00E+03	-1.00E+03	2.00E+00	0.00E+00	2.00E+00	4.00E+00	4.00E+00	0.00E+00	0.00E+00	0.00E+00
1050	5.04E-05	0.00E+00	8.86E-05	2.66E-05	9.39E-06	-1.00E+03	-1.00E+03	-1.00E+03	2.00E+00	0.00E+00	3.00E+00	2.00E+00	1.00E+00	0.00E+00	0.00E+00	0.00E+00
1110	8.35E-05	5.10E-05	0.00E+00	4.47E-05	1.03E-05	-1.00E+03	-1.00E+03	-1.00E+03	3.00E+00	2.00E+00	0.00E+00	3.00E+00	1.00E+00	0.00E+00	0.00E+00	0.00E+00
1170	7.73E-05	5.17E-05	3.25E-05	1.55E-05	1.97E-05	-1.00E+03	-1.00E+03	-1.00E+03	3.00E+00	2.00E+00	1.00E+00	1.00E+00	2.00E+00	0.00E+00	0.00E+00	0.00E+00
1230	1.57E-04	4.71E-05	0.00E+00	2.93E-05	3.99E-05	-1.00E+03	-1.00E+03	-1.00E+03	6.00E+00	2.00E+00	0.00E+00	2.00E+00	4.00E+00	0.00E+00	0.00E+00	0.00E+00
1290	7.59E-05	6.87E-05	3.10E-05	0.00E+00	2.93E-05	-1.00E+03	-1.00E+03	-1.00E+03	3.00E+00	3.00E+00	1.00E+00	0.00E+00	3.00E+00	0.00E+00	0.00E+00	0.00E+00
1350	4.99E-05	4.63E-05	0.00E+00	4.50E-05	2.88E-05	-1.00E+03	-1.00E+03	-1.00E+03	2.00E+00	2.00E+00	0.00E+00	3.00E+00	3.00E+00	0.00E+00	0.00E+00	0.00E+00
1410	1.36E-04	4.94E-05	1.27E-04	6.14E-05	0.00E+00	-1.00E+03	-1.00E+03	-1.00E+03	5.00E+00	2.00E+00	4.00E+00	4.00E+00	0.00E+00	0.00E+00	0.00E+00	0.00E+00

3.6.1 Calculating errors in the data obtained from the spacecraft

Table 6 shows the data collected by the SIS instrument on the ACE spacecraft. We then set the 'Start time' to 0, 60, 120... and the 'End time' to 60, 120, 180... The time, He1 [Flux], and Cnt1 are duplicated and put in the order as depicted in Table 7.

Table 7 Data samples for helium particles at 4.032 MeV/n energy level

Time(min)	He1 (Flux)	CNT1	Error	Start time (min)	End time (min)
30	2.67E-05	1.00E+00	2.67E-05	0	60
90	0.00E+00	0.00E+00	#DIV/0!	60	120
150	7.83E-05	3.00E+00	4.52E-05	120	180
210	0.00E+00	0.00E+00	#DIV/0!	180	240
270	4.94E-05	2.00E+00	3.49E-05	240	300
330	7.97E-05	3.00E+00	4.60E-05	300	360
390	0.00E+00	0.00E+00	#DIV/0!	360	420
450	8.09E-05	3.00E+00	4.67E-05	420	480
510	2.41E-05	1.00E+00	2.41E-05	480	540
570	1.03E-04	4.00E+00	5.15E-05	540	600
630	2.52E-05	1.00E+00	2.52E-05	600	660
690	2.52E-05	1.00E+00	2.52E-05	660	720
750	2.64E-05	1.00E+00	2.64E-05	720	780
810	2.18E-05	1.00E+00	2.18E-05	780	840
870	5.72E-05	2.00E+00	4.04E-05	840	900
930	7.46E-05	3.00E+00	4.31E-05	900	960
990	5.08E-05	2.00E+00	3.59E-05	960	1020
1050	5.04E-05	2.00E+00	3.56E-05	1020	1080

We made a separate column for 'Error' as the data obtained directly from the spacecraft will be inaccurate. The error(σ_{stat}) was calculated by using the flux of the particles (He1 Flux) and the particles count per unit time (CNT) obtained from spacecraft as follows:

$$\sigma_{\text{stat}} = \frac{\text{flux}}{\sqrt{\text{counts}}} \quad (3.18)$$

Where: σ_{stat} : is the spacecraft data error

flux: is the density of particles per unit area

counts: is the number of particles

In order to prevent unnecessary difficulties during simulation, we deleted every row with the error value "# DIV/0!".

The starting values, such as the maximum particle density, start time, and half time of the particle density necessary for simulating the motion, were calculated from the data by plotting particle density (particles/(s-cm²-sr-MeV/n)) against time(min). The sample of He1 from the event on 29 November 2020 is shown in figure 34, with the particle density started increasing at 6150 minutes, peaked at 9390 minutes, and halved at 11130 minutes.

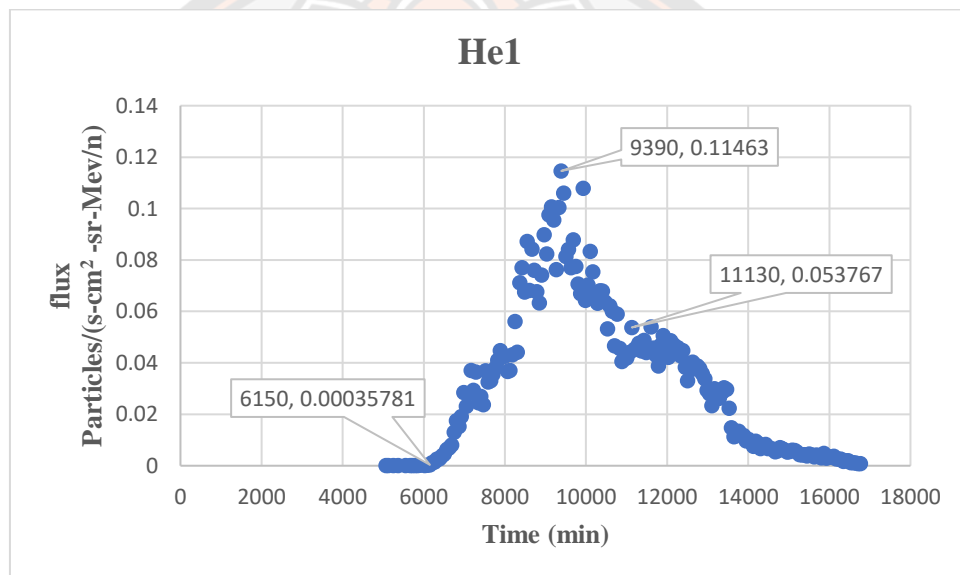


Figure 34 Sample of Helium particle distribution chart at 4.032 MeV/n energy level

The numeric data of 'Start time' and 'End time' from table 33 were copied into a new excel file, saved as text (Tab delimited), and saved as 'He1time.txt'. Similarly, the numeric values of 'Time,' 'He1,' and 'Error' were copied into a new excel file and saved as 'He1data.txt'. For all the elements of all energies of both events, we used the same processes.

3.6.2 Determination of the variables required for particle motion simulation

To simulate data using the transport equation, we prepared the following initial values:

1. Calculating the average energy value for each energy (E_k)

Using the maximum energy E_{max} and minimum energy E_{min} , average value of each energy

level E_k is calculated by the equation:

$$E_k = \sqrt{E_{min} + E_{max}}$$

The sample of average energy values of He is given in table 8, and the same procedure is followed for all elements in both events.

Table 8 Helium's average energy value

Range	E_{min} (MeV/n)	E_{max} (MeV/n)	Sqrt ($E_{min} * E_{max}$) (MeV/n)
0	3.43000	4.74000	4.03215
1	4.74000	6.13000	5.39038
2	6.13000	7.29000	6.68489
3	7.29000	9.72000	8.41777
4	9.72000	13.59000	11.4932
5	13.59000	17.96000	15.6229
6	17.96000	29.35000	22.9592
7	29.35000	41.19000	34.7696

2. Determination of true mass or real mass of an element

The following equation determined the real mass or true mass:

$$Real\ mass(m_0) = \frac{\left(\frac{931.5\ MeV}{c^2}\right) (A)}{Z}$$

Where:

A: is the atomic number

Z: is the mass number

So, to calculate real mass values of He particle,

$$\text{Real mass of He} = \frac{(931.302)(4.0026) \left(\frac{\text{Mev}}{c^2}\right)}{4}$$

$$\text{Real mass of He} = 932.107 \frac{\text{MeV}}{c^2}$$

3. Determination of the distance of the magnetic field lines drawn by the solar wind (R)

The distance of the magnetic field lines drawn by the solar wind (R) as

$$R = \frac{v_{sw} \times 0.002291}{\cos(s/c \text{ latitude})} \quad (3.19)$$

Where:

R is the the distance of magnetic field drawn by solar wind

v_{sw} is the solar wind speed ($1 \text{ km/s} = 0.00291 \text{ AU/Min}$)

4. Determination of the distance between the Sun and the position of the spacecraft (USER R)

We computed the distance between the Sun and the spacecraft's position as

$$USERR = \frac{1 \text{ AU}}{1 + 0.0017 \left[\left(\frac{DOY-2}{365} \right) \times 360 \right]}$$

Where:

USERR is the is the distance between the Sun and the spacecraft's location

DOY is the day of the eruption, the number of days in a year

5. Determination of each energy level's momentum (p)

To simulate the motion of particles, we calculated the momentum(p) of each particle as

$$P = \sqrt{(E_k + m_0)^2 - m_0^2}$$

Where:

E_k : the average energy value (measured in MeV/n) of each energy level

P: the momentum (MeV/c)

m_0 : the true mass of the element (in kg)

6. Determination of speed of each energy level

We computed the speed of each energy as a ratio of the speed of the solar wind and the speed of light as:

$$v_{sw} = \beta c$$

$$\beta = \frac{v_{sw}}{c} = \frac{p}{E_k + m_0}$$

Where:

B: ratio of solar wind speed to light speed.

v_{sw} : the speed of each energy level (AU/ min).

c: speed of light (0.1202 AU/ min).

7. Determination of each energy level's spectrum

We computed the spectra of each energy level as follows:

$$\text{spectrum} = \frac{\text{Maximum flux at energy level } N}{\text{The maximum flux at the power level}}$$

Where: $N = 1, 2, 3, 5, 6, 7 \text{ \& } 8$

8. Determination of the particle's constant decay value

High-energy particles from the Sun continually decompose, and this decomposition follows the power law as follows:

$$\frac{dE}{dN} \propto E^{-\gamma}$$

Where:

E : the energy of particles.

N : the number of particles in each energy level.

γ : Constant decay of the particle

Figure 35 illustrates how the slope of the graph between the momentum log value and the spectral log value can be used to determine the particle's constant decay. For the particle motion simulation, we used the default setting.

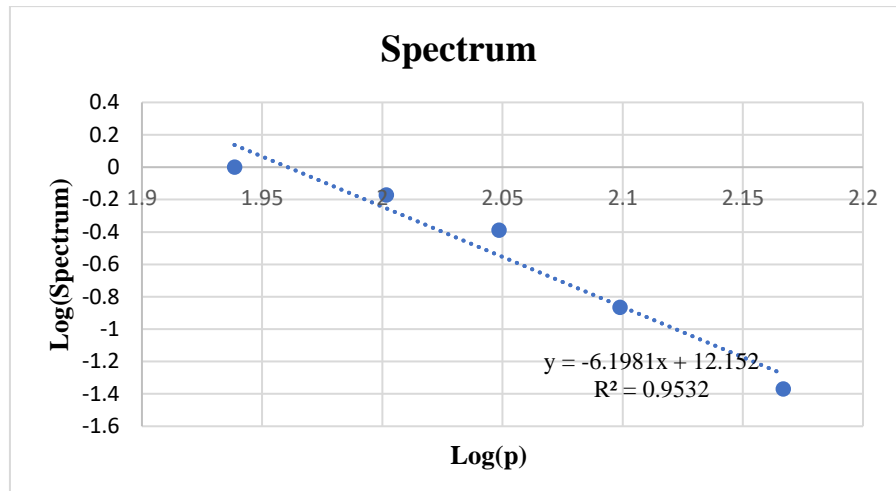


Figure 35 A Helium sample graph illustrating the relationship between momentum log values and spectral spectra of occurrences on 29 November 2020.

9. Determination of the maximum particle distance in each energy level

We computed a particle's maximum distance traveled as

$$V_{max} = \beta c$$

$$S = V_{max} t$$

Where:

V_{max} : the maximum speed of each energy level (AU/min).

β : the ratio of solar wind speed to light speed.

t : the time taken by the particle's motion (min).

S : the distance traveled by a particle (AU).

c : the speed of light (0.1202 AU/min).

Table 9 The values used in the He data preparation process

E (MeV/n)	m_0 (MeV/c ²)	P (MeV/c)	B	V (AU/min)	log P	He flux	spectrum	log (spectrum)	S (AU)
4.03215	932.1075	86.79316071	0.092713903	0.011144211	1.938485504	0.012076	1	0	64.19065617
5.39038	932.1075	100.388662	0.107081482	0.012871194	2.001684666	0.0081696	0.676515402	-0.169722	74.13807792
6.68489	932.1075	111.8336263	0.119124982	0.014318823	2.048572407	0.005189	0.429695263	-0.366839	82.47641933
8.41777	932.1075	125.5523475	0.133491732	0.016045706	2.098824837	0.00294	0.243458099	-0.613576	92.42326776
11.4932	932.1075	146.8260518	0.155601889	0.018703347	2.166803121	0.0025845	0.214019543	-0.669547	107.7312794
15.6229	932.1075	171.3724585	0.18082406	0.021735052	2.233941027		0	0	125.1938994
22.9592	932.1075	208.1538131	0.217946886	0.026197216	2.318384371		0	0	150.8959623
34.7696	932.1075	256.9570683	0.265759804	0.031944328	2.409860569		0	0	183.9993316

Helium particle preparation is shown in Table 9 for the energy range of 4.032 to 34.7696 MeV/n.

Where:

E: the average energy (MeV/n)

m_0 : the real mass (in kg)

P: the momentum (in MeV/c)

β : the ratio of solar wind speed and light speed

V: the velocity of a particle at different energy levels (in AU/min)

S: the maximum distance traveled by the particles (in AU).

3.7 Simulation of motion of high-energy particle

We have simulated the motion of high-energy particles using Ruffolo's transportation equation. Since the equation is in complex linear partial differential equation form, we used the finite difference method to solve it. The processing was done through the C program in the ubuntu operating system using initial data from the ACE spacecraft. The following is Ruffolo's transport equation.

$$\begin{aligned}
\frac{\partial F}{\partial t} = & -\frac{\partial}{\partial z} \mu v F - \frac{\partial}{\partial z} \left(1 - \mu^2 \frac{v^2}{c^2} \right) v_{sw} \sec \psi F \\
& - \frac{\partial}{\partial \mu} \frac{v}{2L(z)} \left[1 + \mu \frac{v_{sw}}{v} \sec \psi - \mu \frac{v_{sw} v}{c^2} \sec \psi \right] (1 - \mu^2) F \\
& + \frac{\partial}{\partial \mu} v_{sw} \left(\cos \psi \frac{d}{dr} \sec \psi \right) \mu (1 - \mu^2) F \\
& + \frac{\partial}{\partial \mu} \frac{\phi(\mu)}{2} \frac{\partial}{\partial \mu} \left(1 - \mu \frac{v_{sw} v}{c^2} \sec \psi \right) F \\
& + \frac{\partial}{\partial p} p v_{sw} \left[\frac{\sec \psi}{2L(z)} (1 - \mu^2) + \cos \mu \frac{d}{dr} (\sec \psi) \mu^2 \right] F
\end{aligned}$$

The wind.c program in the simulation of particle motion takes various data parameters and stores the output result in a file named intense.dat for later use in fitting to compare data.

3.8 Fitting data to compare

After obtaining the results of the particle motion simulation, we used the linear least-squares fitting method and compared the data from the spacecraft to the results of the particle motion simulation using the following equation:

$$\chi^2 = \sum_{i=1}^N \left[\frac{y_n - y(x_n)}{\sigma_n} \right]^2$$

Where:

χ^2 : the sum of squared differences of data n

y_n : the spacecraft's actual data in the particle flux data (fitdata.dat)

$y(x_n)$: the data from a particle motion simulation in the counts.dat file format

σ_n : the divergence of each data point

n : the number of data

In order to identify the trend of the mean free path that produces the lowest chi-square value out of all three or five nearby points, we fitted distances to simulate the mean free path and compared them to the real data. We obtained the parabolic trend line as shown in a sample (figure 36) of helium particles with the energy of 4.032 MeV/n.

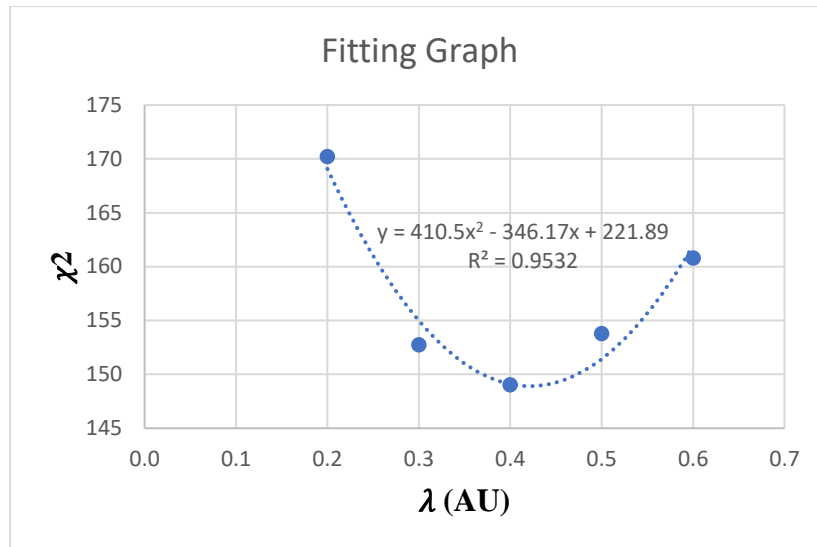


Figure 36 The relationship between χ^2 and the mean free path (λ)

3.9 Determination of Injection Time

After obtaining the best λ , the function of particle release according to time was generated and later used to plot graphs and calculate particle release time. We computed the particle release time from the injection profile obtained from the Ubuntu operating system using the Full Width at Half Maximum (FWHM) method, where the width of the highest point is halved. Figure 37, a sample graph, illustrates the detailed graphing, and we performed the calculations as listed below.

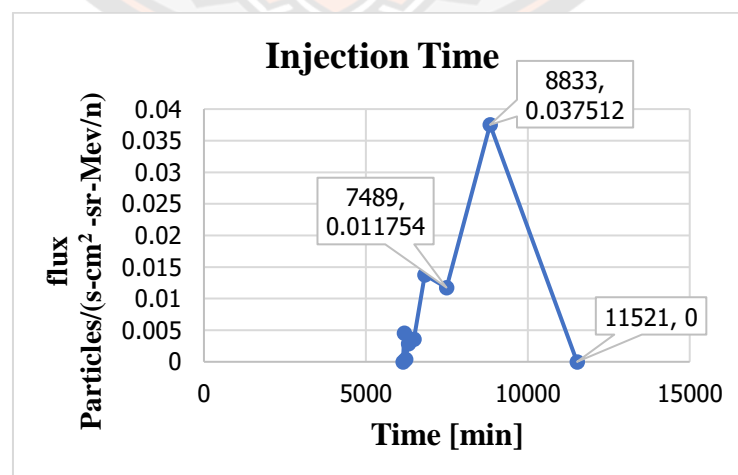


Figure 37 The helium release triangle with an energy level of 4.032 MeV/n

Table 10 The injection profile obtained from the ubuntu operating system of He1 released on 29 November 2020

Time (min)	Injection	Error	Error/2
6145	0	0	0
6187	0.004531	0.000963	0.000482
6229	0.000374	0.000961	0.000481
6313	0.002868	0.000671	0.000336
6481	0.00359	0.00059	0.000295
6817	0.01375	0.000773	0.000387
7489	0.011754	0.000693	0.000347
8833	0.037512	0.000636	0.000318
11521	0	0	0

Table 10 is the sample of the injection profile obtained from the ubuntu operating system, which was then used to plot graphs. The following are sample procedures using the FWHM method for Helium element at energy level 4.032 MeV/n emitted from Sun to Earth:

1. Determine the half value from the release triangle's highest point (Half Maximum)

$$\text{Half maximum} = \frac{y_2}{2} = \frac{0.037512}{2} = 0.018756$$

2. Determine the slope from line 1

$$\text{Slope}(m) = \frac{\Delta y}{\Delta x} = \frac{y_2 - y_1}{x_2 - x_1}$$

From the graph:

$$(y_2, y_1) = (0.037512, 0.011754)$$

$$(x_2, x_1) = (8833, 7489)$$

$$\text{Slope}(m) = \frac{0.037512 - 0.011754}{8833 - 7489} = 0.000019165$$

Thus, the equation of line 1 will be

$$y = (0.000019165)x + C \quad (3.20)$$

3. Determining the slope from line 2

$$\text{Slope } (m) = \frac{\Delta y}{\Delta x} = \frac{y_2 - y_1}{x_2 - x_1}$$

From the graph:

$$(y_2, y_1) = (0, 0.037512)$$

$$(x_2, x_1) = (11521, 8833)$$

$$\text{Slope } (m) = \frac{0 - 0.037512}{11521 - 8833} = -0.000013955$$

Thus, the equation of line 2 will be

$$y = (-0.000013955)x + C \quad (3.21)$$

4. Determine the value of C for equation (3.20)

From equation (3.20), we know that

$$y_1 = (0.000019165)x_1 + C$$

Let us choose the co-ordinate:

$$(x_1, y_1) = (7489, 0.011754)$$

Substituting the value in this equation, we got:

$$C = -0.131774022$$

5. In the equation of line1, substitute the values of half maximum and C

From the equation of line 1,

$$y_1 = (0.000019165)x_1 + C$$

$$0.018756 = (0.000019165)x_1 - 0.131774022$$

$$x_1 = t_1 = \frac{0.018756 + 0.131774022}{0.000019165} = 7854.35 \text{min}$$

6. Determine the value of C for equation (3.21)

From equation (3.21),

$$y = (-0.000013955)x + C$$

Selected a co-ordinate from line 2

$$(x_1, y_1) = (8833, 0.037512)$$

Substituting the values of x_1, y_1 in the equation, we got:

$$C = 0.16077967$$

7. In the line 2 equation, substitute the values of half maximum and C.

From the equation of line 2,

$$0.018756 = (-0.000013955)x_2 + 0.16077967$$

$$x_2 = t_2 = \frac{0.018756 - 0.16077967}{-0.000013955} = 10177 \text{ min}$$

8. Final injection time

Now, subtracting $t_2 - t_1$ we will obtain injection time

$$t_2 - t_1 = 10177 \text{ min} - 7854.35 \text{ min} = 2322.649 \text{ min}$$

Thus, the injection time of helium particles at 4.032 MeV was 2322.649 minutes.

Likewise, we followed the same preceding methods to determine injection time for all energy levels in both events.

3.10 Space condition at the beginning of the 25th solar cycle (in 2020 and 2021)

The Sun is the primary source of space weather. Space weather effects were initiated by coronal mass ejections (CMEs), which are sudden outbursts of plasma and magnetic field ropes from the Sun's atmosphere, as well as solar flares, which are sudden bursts of radiation. As a result, we investigated the space environment during two significant events at the beginning of the 25th solar cycle, which began in December 2019. We selected two significant events, one from 2020 and another from 2021, to study space weather.

According to the SpaceWeatherLive website's records of the top 50 solar flares, there were two M-class eruptions in 2020, with the remaining 48 being C-class eruptions. Despite the fact that the first M4.4 solar flare occurred after the start of the 25th solar cycle on 29 November, there was no impact on Earth due to the location of the eruption. Out of 50 top solar flares, 28 solar flares erupted from the east limb of the Sun, 13 from the west limb, and nine solar flares that were visible but could not specify the location.

This solar cycle's first and strongest solar flares erupted on 3 July and 28 October 2021 with X-ray intensities of X1.59 and X1, respectively. In the same year, 29 C-class solar flares and 19 M-class solar flares erupted. Out of 50 top solar flares,

24 erupted from the west limb of the Sun, 17 from the east limb, but the spacecraft could not specify the location of the remaining 9.

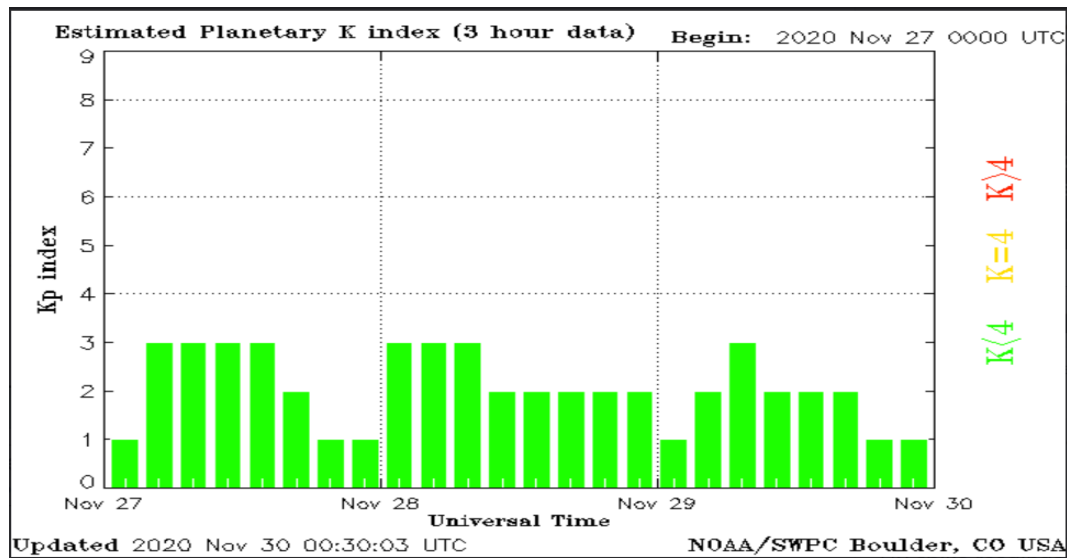


Figure 38 The kp-index value on 27-30 November 2020

Source: <https://www.spaceweatherlive.com/en/archive/2020/11/29/xray.html>

On 29 November 2020, the kp-index was less than 4 as depicted in figure 38, which is not at a level that interferes with radio transmission or satellite navigation systems. A detailed explanation of the effect of the kp-index is shown in Table 11.

Table 11 The potential impact of solar activity on the Kp-index

kp-index	Severity Level	The effect
9	most intense	The electricity distribution system cannot supply electricity. Damage transformer. Complications in receiving and sending satellite signals and tracking satellite positions. For several hours, the low-frequency radio guidance system will be unavailable
8	very intense	There will be issues with the power supply and complications in tracking the satellite. The low-frequency radio navigation system will be disturbed
7	intense	Satellite navigation systems and low-frequency radio wave navigation systems may crash from time to time and cause the Aurora phenomenon in the 50 ⁰ latitude region
6	moderate	High-frequency radio propagation in high latitudes signals will be reduced. Cause the Aurora phenomenon in the 55 ⁰ latitude zone
5	little	Cause little disruption to satellite operations and the Aurora phenomenon in high latitudes

Source: <https://www.electronics-notes.com/articles/antennas-propagation/ionospheric/solar-indices-flux-a-ap-k-kp.php>

CHAPTER IV

RESULTS AND DISCUSSION

This study examined the transport of high-energy particles from the Sun to Earth in order to study the space weather at the beginning of the 25th solar cycle. The research was carried out using data collected by the ACE spacecraft's SIS instruments. We downloaded the spacecraft data from the internet and formatted it as the initial values for simulation. The simulation was performed in the Ubuntu operating system using Ruffolo's transport equation (1995, 1998), which was solved using a finite difference numerical method written in the C program. Based on the two strongest events, which occurred at the beginning of the 25th solar cycle on 3 July 2021, with an X-ray intensity of X1.59, and 29 November 2020, with an X-ray intensity of M4.4, we analyzed high-energy particles of helium, carbon, nitrogen, oxygen, and iron at different energy levels.

This chapter discusses the results of the best mean free path (λ) according to its least chi-square value, error, and simulated value. The fitting results (compare.dat) and injection profile were obtained as auto-generated files using the spacecraft's original data. The fitting results (compare.dat) file contains information on the correctness of the results. This chapter also covers the injection time derived using the FWHM in the injection profile to propagate SEPs from the Sun to the Earth.

4.1 The simulation result of the propagation of SEPs

The output results from the simulation of particle motion are saved in the file to be used in the fitting process later. Figure 39 depicts the simulation results for the helium particle distribution over time at various energies between 4.032 and 11.493 MeV/n. According to the graph, higher-energy particles have less flux and distribute more quickly than low-energy particles. A particle with more energy travels to Earth faster than one with less energy.

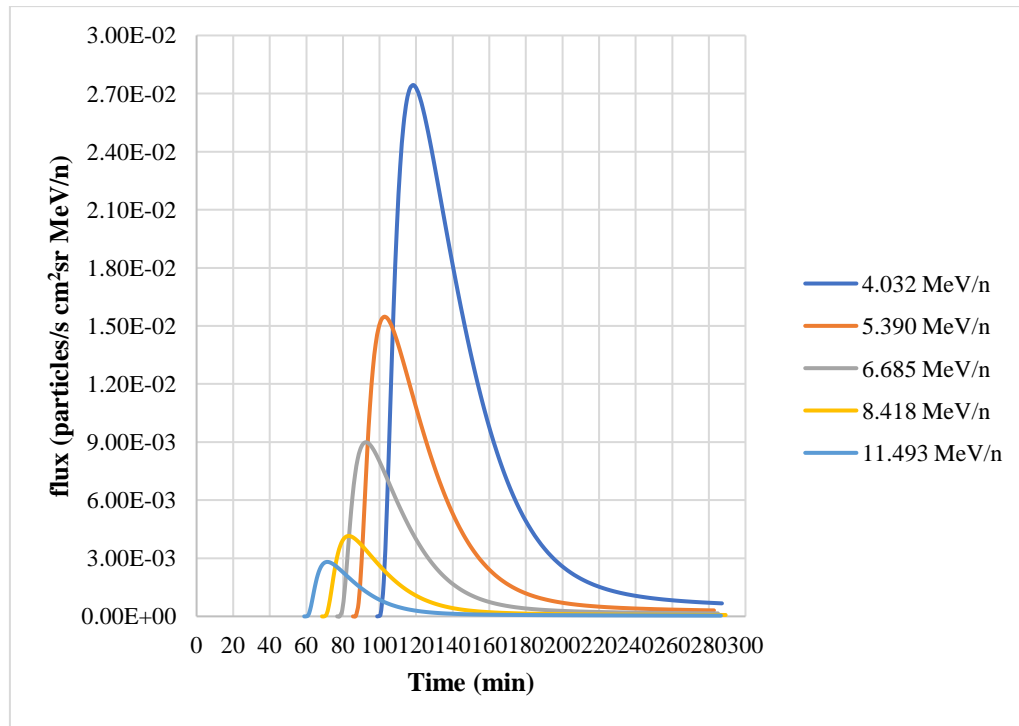


Figure 39 The simulation results of helium particle distribution over time at different energy levels from 4.032– 11.493 MeV/n

4.2 Simulation of the particle distribution over time using the best mean free path

In the particle motion simulation, the helium particle is simulated by the distribution of particles across time with varying mean free paths (λ). Where λ , is the particle's distance traveled along the irregular magnetic field lines before being scattered by the unstable magnetic field lines. The simulation results are depicted in Figure 39.

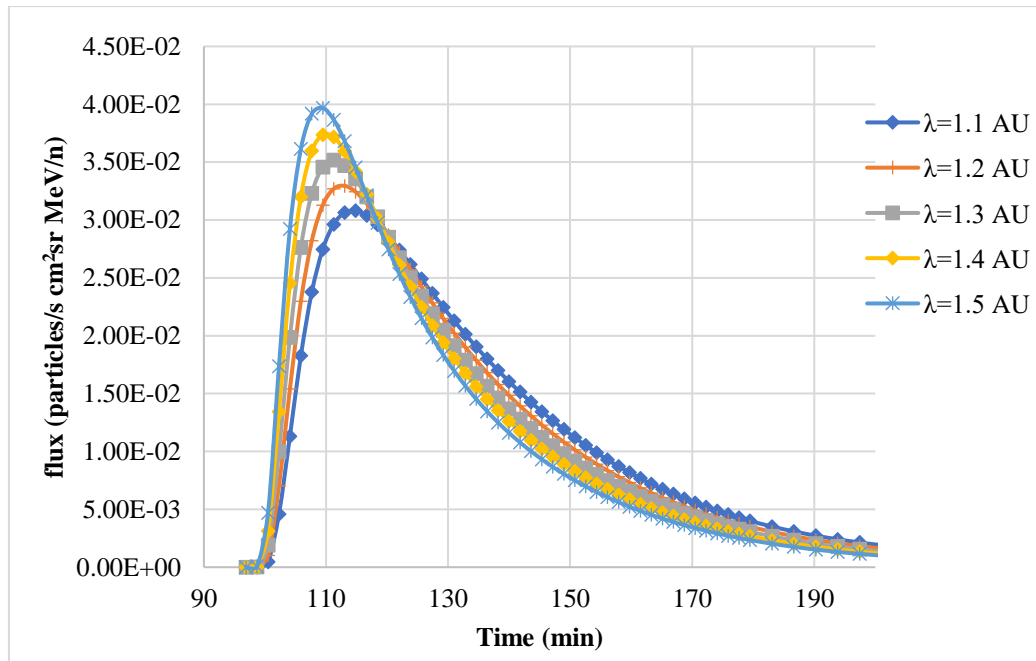


Figure 40 Simulation result showing the dispersion of helium particles along different mean free paths at a level of energy of 4.032 MeV/n

Figure 40 illustrates the flux of helium particles over time at different λ , at an energy level of 4.032 MeV/n. The graph clearly demonstrates that particles with a high λ travel to Earth more quickly than particles with a lower λ . Additionally, particles with a high λ were less scattered than particles with a low λ . In comparison to the particle distribution with a high λ , the particle distribution with a low λ has a broader peak.

4.3 Fitting comparison of simulation results and spacecraft data

We computed the injection function of particles moving from the Sun to the Earth using the fitting method. The data from the spacecraft, the simulation result of particle propagation with the best mean free path, a comparison of the spacecraft data with the simulation result of the fitting process, and the injection function of helium at 4.03 MeV/n are all shown in figure 41, 42, 43, and 44.

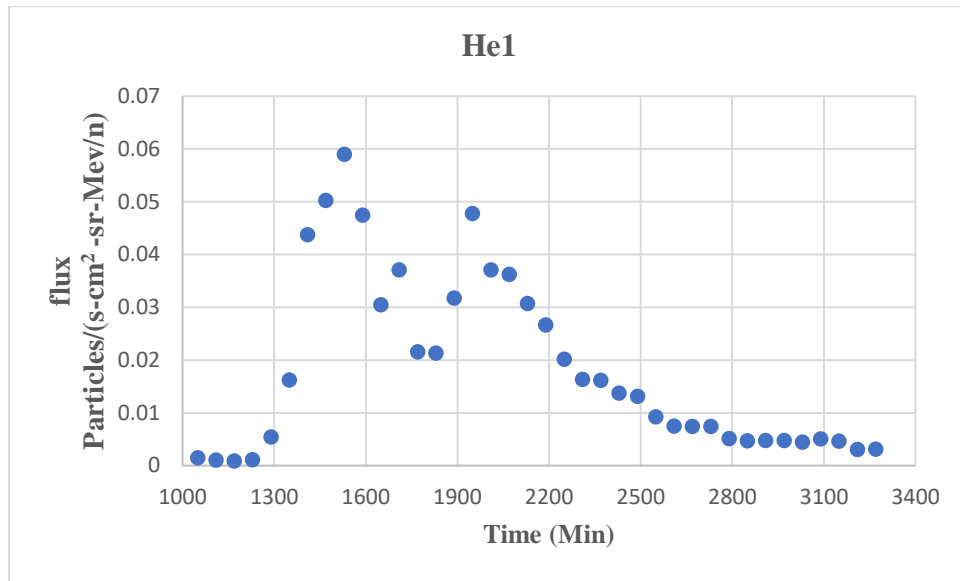


Figure 41 The spacecraft data of He at 4.032 MeV/n for the solar event on 3 July 2021

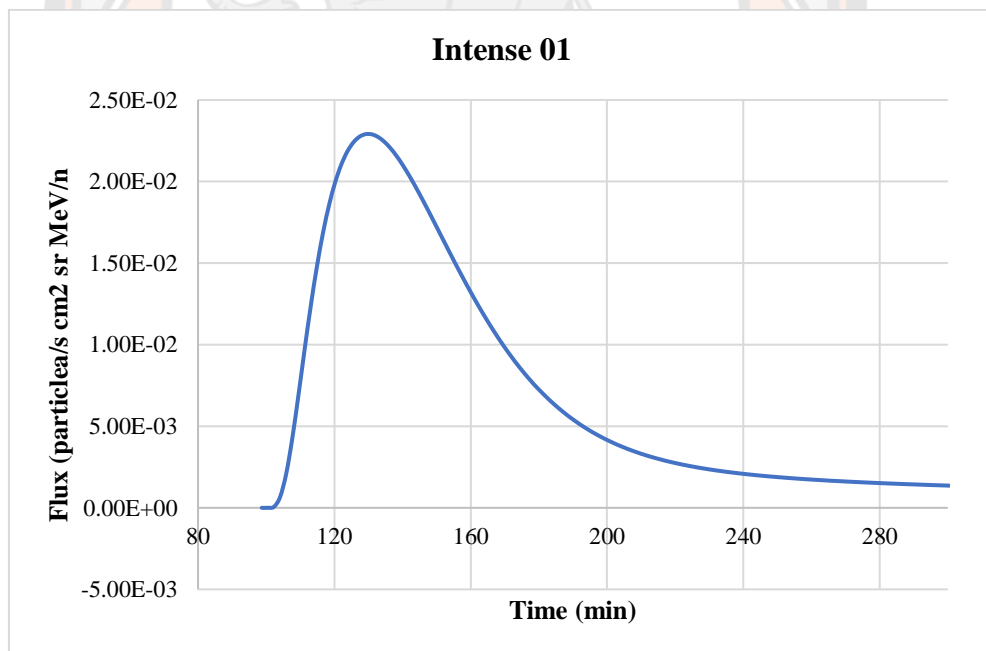


Figure 42 The simulation result of He at 4.032 MeV/n for the solar event on 3 July 2021

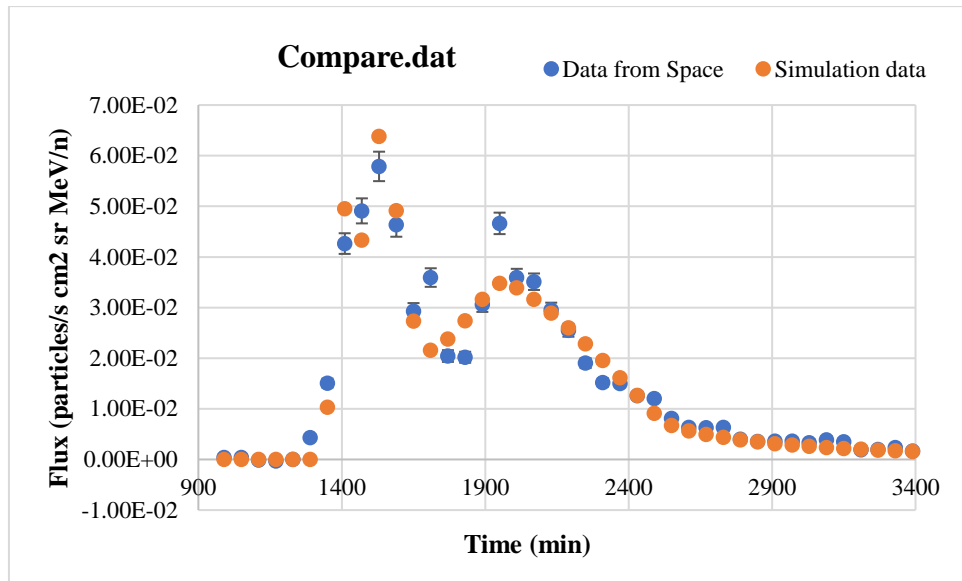


Figure 43 The simulation result of He at 4.032 MeV/n for the solar event on 3 July 2021

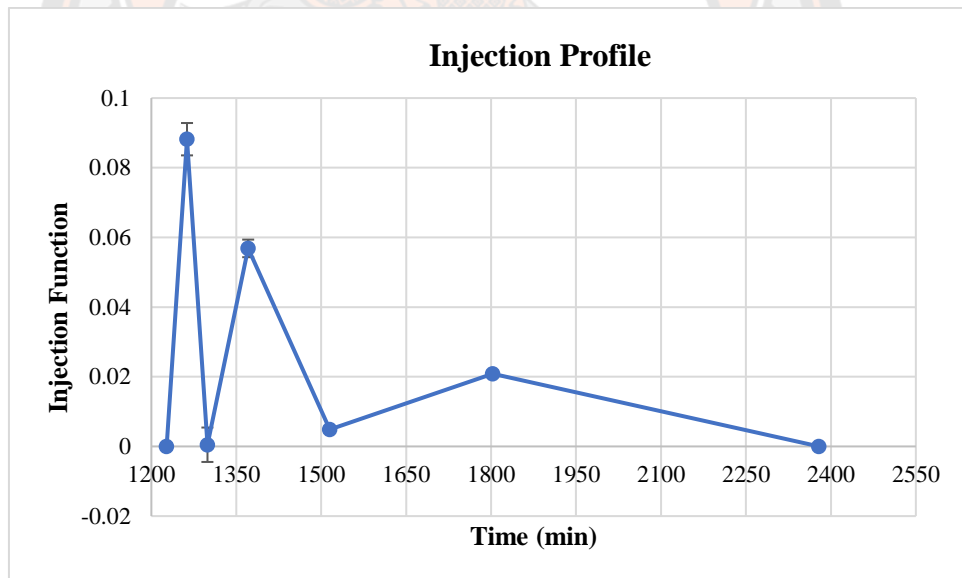


Figure 44 The injection profile of He at 4.032 MeV/n for the solar event on 3 July 2021

The data from the spacecraft, the simulation result of particle propagation with the best mean free path, the data comparison between the spacecraft, and the simulation result of the fitting process and injection function of the helium at 4.032 MeV/n are all shown in figure 45, 46, 47, and 48, respectively.

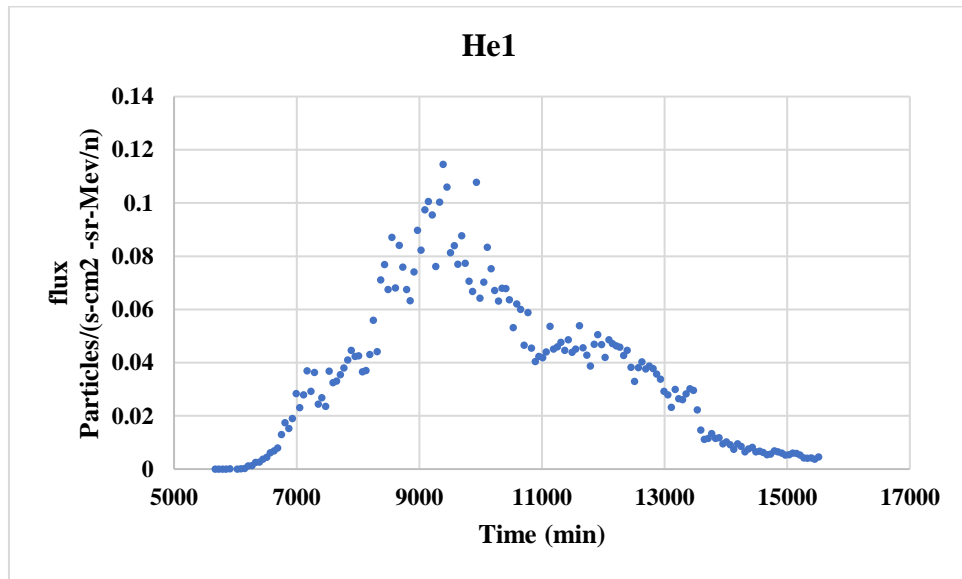


Figure 45 The spacecraft data of He at 4.032 MeV/n for the solar event on 29 November 2020

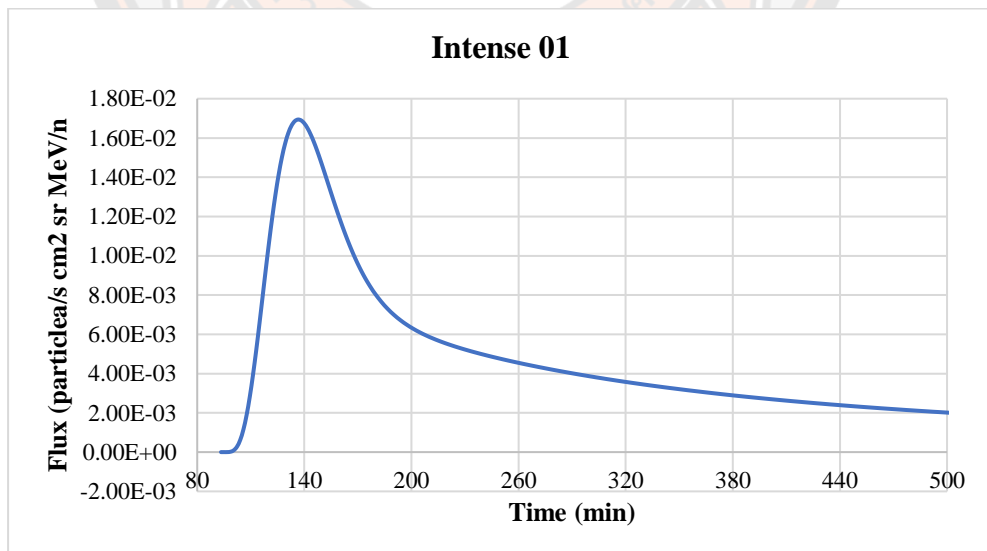


Figure 46 The simulation result of He at 4.032 MeV/n for the solar event on 29 November 2020

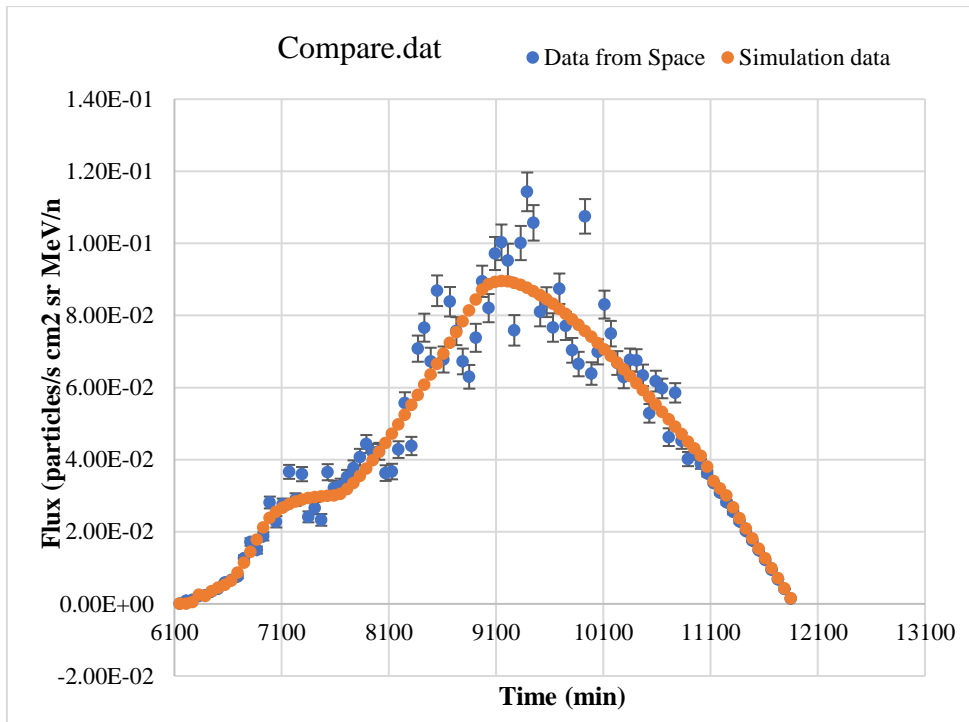


Figure 47 The fitting result at 4.032 MeV/n for the solar event on 29 November 2020

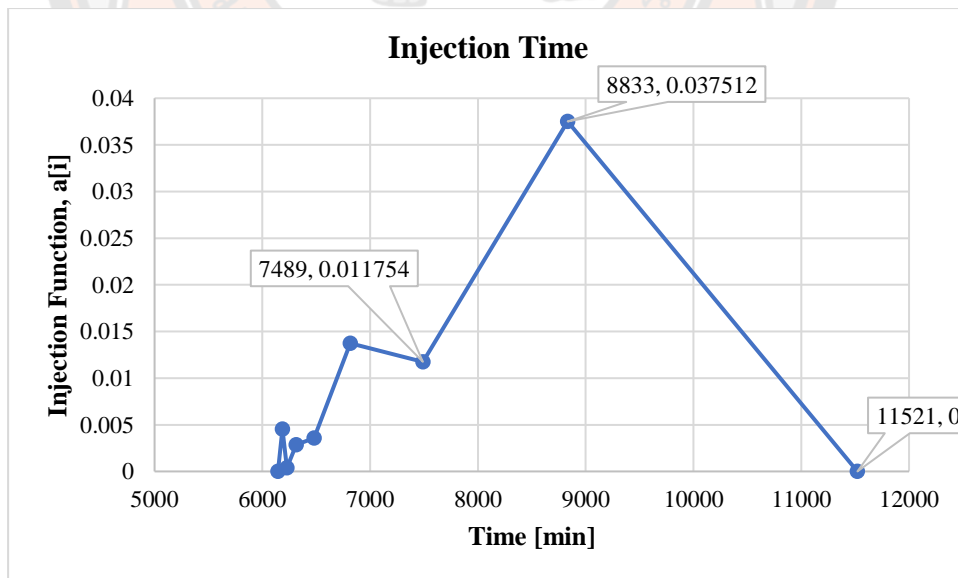


Figure 48 The injection profile of He at 4.032 MeV/n for the solar event on 29 November 2020

The data from the spacecraft, the particle propagation simulation result with the best mean free path, and the data comparison between the spacecraft and the simulation result from the fitting process and injection function of the oxygen at 8.538 MeV/n are all shown in Figures 49, 50, 51, and 52.

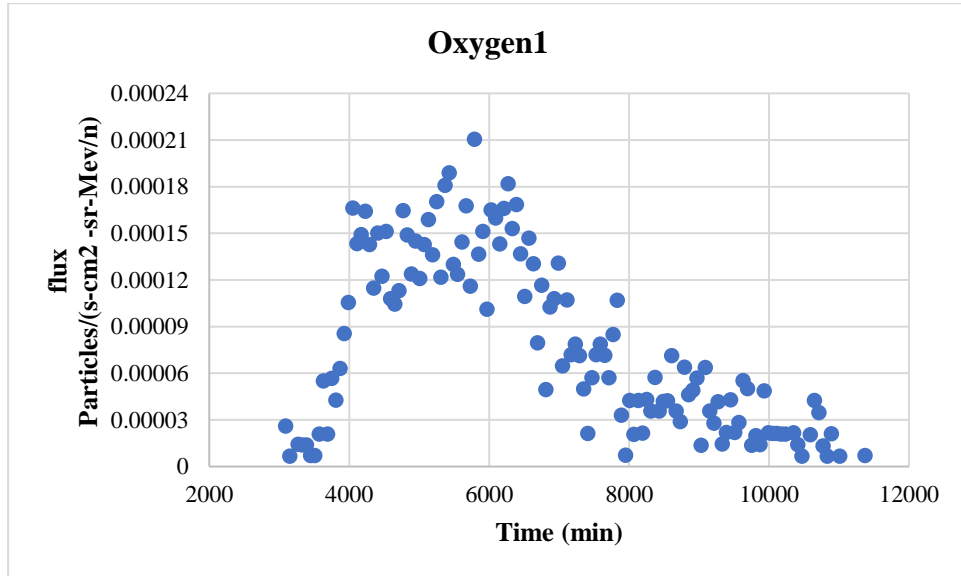


Figure 49 The spacecraft data of O at 8.538 MeV/n for the solar event on 29 November 2020

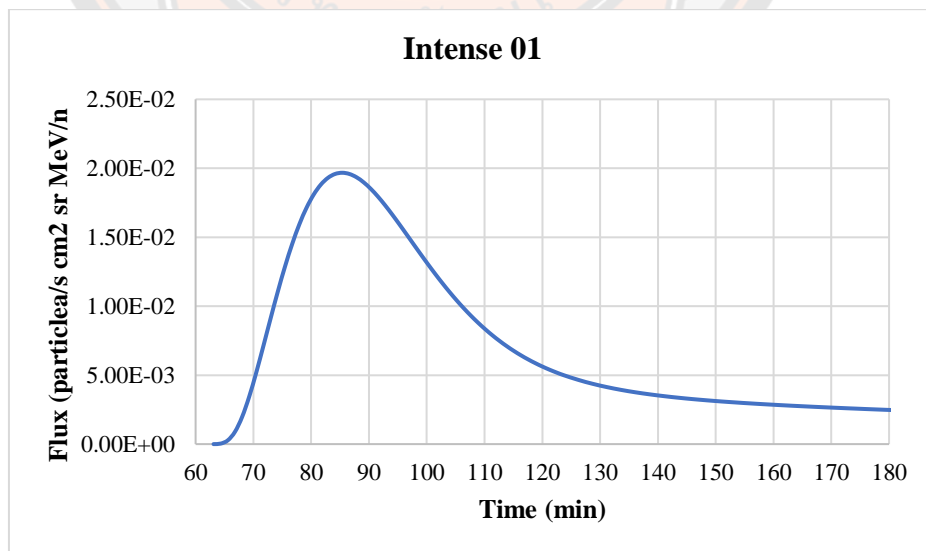


Figure 50 The simulation result of O at 8.538 MeV/n for the solar event on 29 November 2020

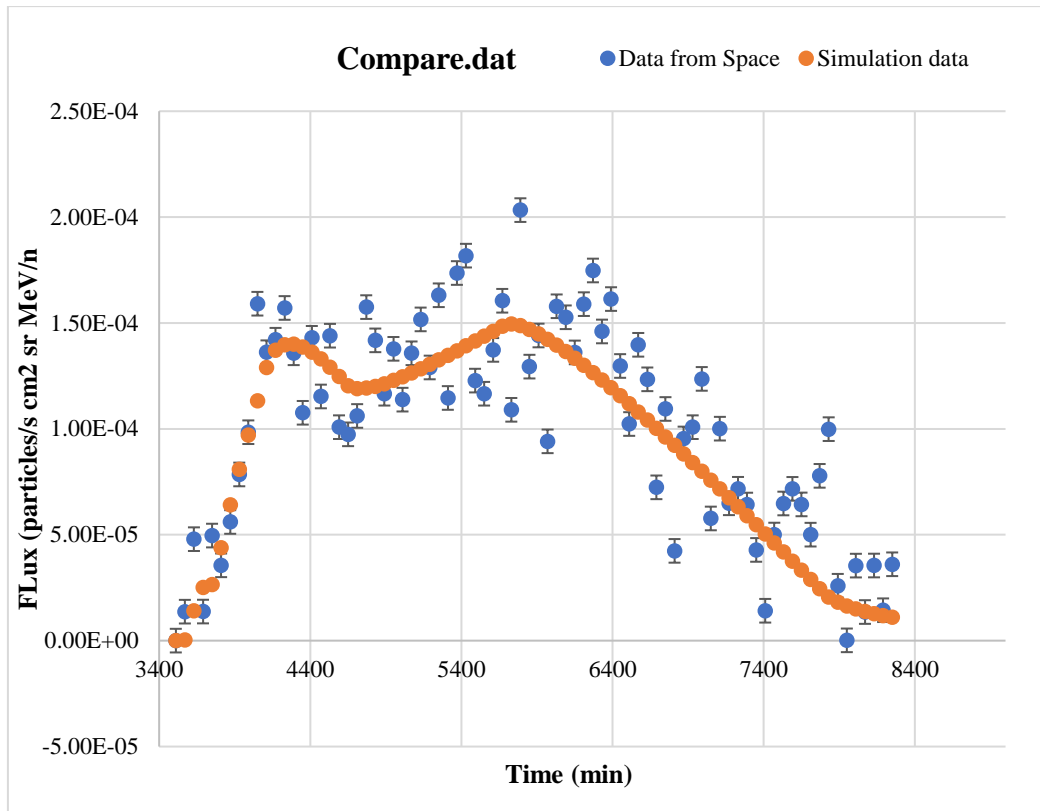


Figure 51 The fitting result of O at 8.538 MeV/n for the solar event on 29 November 2020

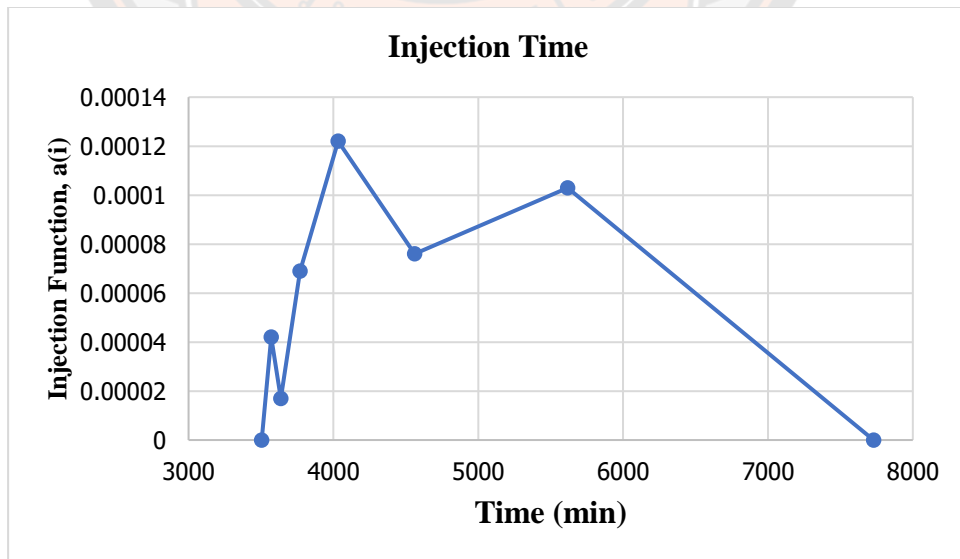


Figure 52 The injection profile of O at 8.538 MeV/n for the solar event on 29 November 2020

For the solar events on 29 November 2020 and 3 July 2021, the fitting result is presented in table 12 as the best mean free path for each particle at various energy levels in AU and the release time of particles from the Sun to the Earth in minutes.

Table 12 The helium and oxygen simulation results of two different events

Events	X-ray intensity	Element	Energy (MeV/n)	Mean free path (λ) (AU)	Injection Time(min)
29/11/2020	M4.4	Helium	4.032	0.422 ± 0.062	2322.650
			5.390	0.348 ± 0.096	2261.145
			6.685	0.376 ± 0.132	3468.644
			8.418	0.427 ± 0.116	3204.268
		Oxygen	8.538	0.529 ± 0.277	2729.512
3/7/2021	X1.59	Helium	4.032	0.648 ± 0.088	406.076
			5.390	0.804 ± 0.069	228.099
			6.685	0.788 ± 0.090	221.911
			8.418	0.933 ± 0.100	207.257
			11.493	1.126 ± 0.103	87.693

We found that helium particles at the energy levels of 4.032-8.418 MeV/n have an average λ of 0.400 AU, and oxygen level 8.538 MeV/n has λ of 0.529 AU of the solar event erupted on 29 November 2020 with the X-ray intensity of M4.4. The injection time of high-energy particles released during this event was 2323 -3204 minutes, or around 2 days. The first X-class solar flare of the solar cycle 25 erupted on 3 July 2021, and this was the first X-class solar flare after the massive X8.2 solar flare erupted on 9 September 2017. We found that the helium particles at the energy level of 4.032-11.493 MeV/n have a λ in the range of 0.648 - 1.126 AU during this solar event. The injection time decreases when the λ increases.

The solar flare with X-ray intensity X1.59 has a larger mean free path (λ), as shown in Table 12, indicating that less diffusion will occur and its impact on the Earth will more significant. In contrast, the solar flare with X-ray intensity M4.4 has a smaller mean free path (λ), which means that there will be more diffusion and less impact. Figures 53 and 54 display the data from Table 12 on the best mean free path and injection time for various energy levels.

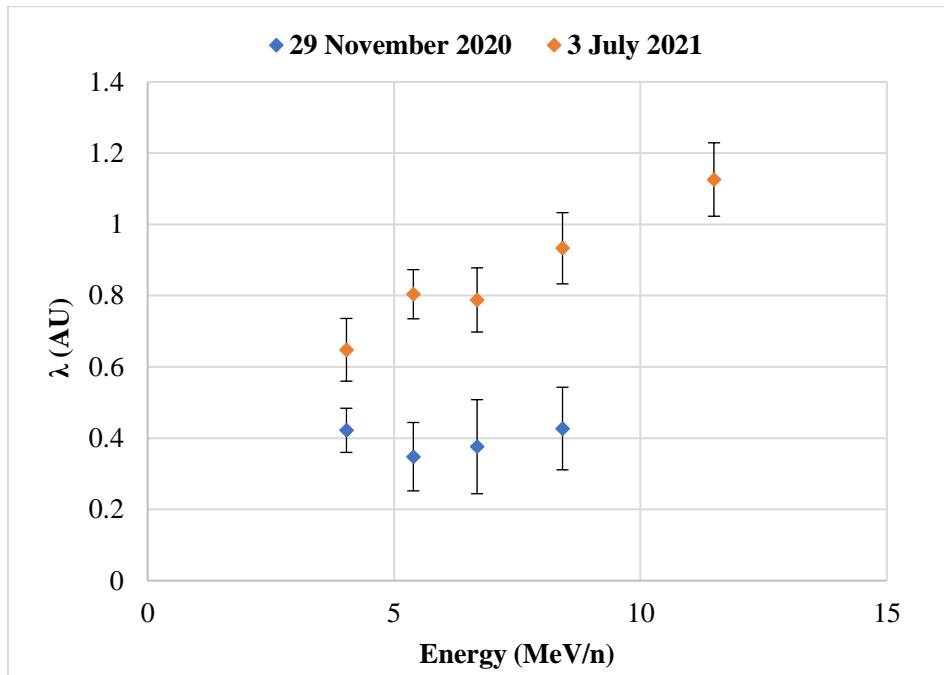


Figure 53 The λ of He at the various energy levels of two events

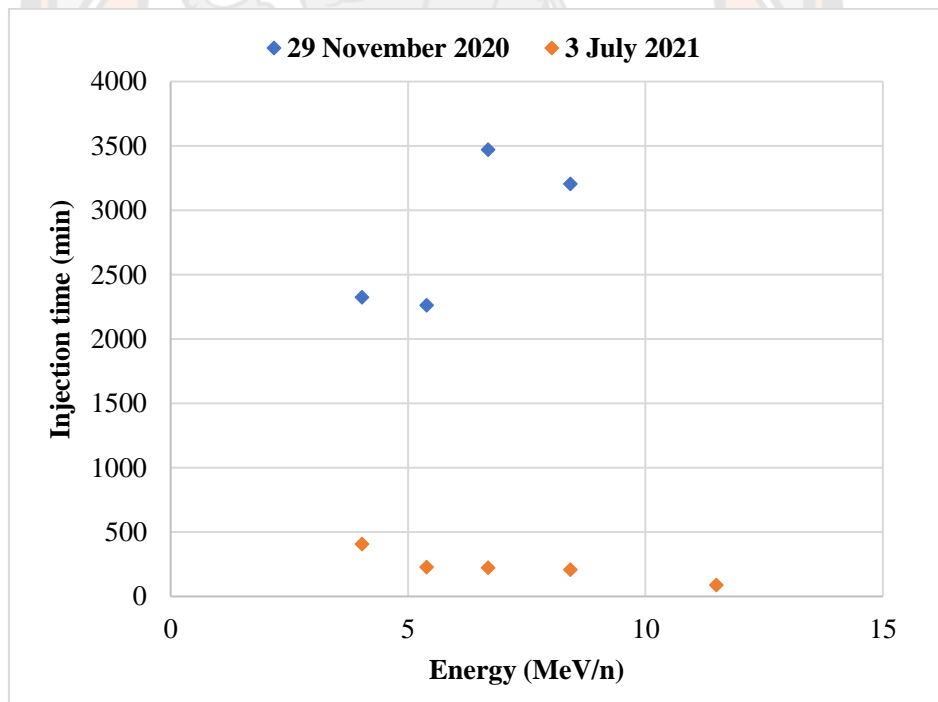


Figure 54 The Injection time of two events at the various energy levels

CHAPTER V

CONCLUSION

This research studied the space weather at the beginning of the 25th solar cycle and physical characteristics, including the outburst from the Sun's surface, by analyzing the motion of high-energy particles using the distribution data obtained from the ACE spacecraft. The propagation of SEPs was studied using Ruffolo's transport equation, which was solved using the finite difference method. We used the piecewise linear least-square fitting to find the best solutions. Further, we compared the simulated solar flare injection time and the X-ray injection on the Sun and analyzed the results with the space environment. This research was focused on the two most powerful solar events, M4.4 on 29 November 2020 and X1.59 on 3 July 2021.

The chapter discusses the significant analysis of the results obtained, and we draw our interpretation of the particle's behavior that propagates toward the Earth from the Sun and the space weather.

5.1 Discussion

The study mainly focused on the two strongest solar events at the beginning of the 25th solar cycle. The current solar cycle started in December 2019, 2020, and 2021 lies in the solar minimum. Generally, studies show that the solar cycle begins with a solar minimum with less solar activity and mild space weather (McGinnis, 2016) (Gorney, 1990) (Hathaway, 2015). But on the other hand, studies also show that the solar flare of X-ray intensity M and X are moderate and violent solar flares and will impact the space weather more (Reep & Knizhnik, 2019) (Masuda et al., 1994). The first strongest solar event erupted on 29 November 2020 with the X-ray intensity M4.4, and the first X-class solar flare erupted on 3 July 2021 with the intensity X1.59. Table 12 shows that the solar flare with the higher X-ray intensity (X1.59) propagated from the Sun to Earth faster than the solar flare with the lower X-ray intensity (M4.4). The X1.59 has a shorter injection time because it propagates along the magnetic field with a greater mean free path, whereas M4.4 propagates with a lower mean free path and longer injection time. This is because particles having a longer mean free path are less scattered (diffusion is less), allowing them to reach the Earth faster. Due to the

abnormalities in the magnetic field lines caused by the effect of the solar wind, particles with a lower mean free path become more scattered (diffusion is more) and take longer to reach Earth.

The solar event on 29 November 2020 erupted at 12.34 UT and finished at 13.41 UT with a 67-minute injection, and the solar event on 3 July 2021 erupted at 14.18 UT and ended at 14.34 UT with a 16-minute injection. However, as seen in table 12, the injection time recorded by the spacecraft was significantly longer than the injection time detected straight from the Sun. The mass difference between the injection time in the simulation and the direct detection result clearly indicates that the particles took longer to reach space, making them weaker and having no effect on space weather.

SOHO and STEREO-A coronagraph imagery revealed a considerable quantity of coronal dimming and type II radio emission, indicating that a massive and fast CME with a velocity of roughly 1,400 km/s was launched during the event on 29 November 2020. Furthermore, the event was linked to a 10 cm radio burst with a peak flux of 240 sfu that lasted 34 minutes, showing that the electromagnetic erupt correlated with a solar flare at the 10 cm wavelength was higher than the original 10 cm radio background. This could represent the substantial radio noise associated with a solar flare, which is usually short-lived but can create interference for sensitive receivers such as radar, GPS, and satellite communications (Koons et al., 1999). Since the solar flare erupted from S23E98, the plasma cloud was pointed away from Earth, and there was no impact on the planet.

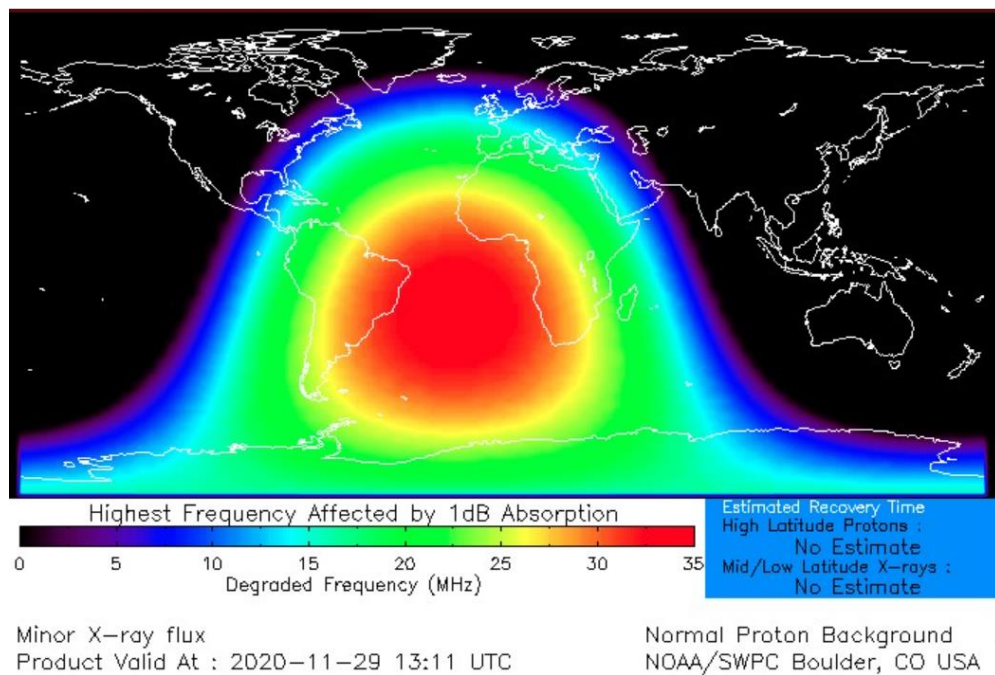


Figure 55 The map showing the impact of the solar flare on the atmosphere

Source: NOAA/ SWPC

Similarly, on 3 July 2021, the first X-class solar flare of the 25th solar cycle and the first X-class solar flare since 10 September 2017 erupted. The X-ray blast hurtled towards Earth at the speed of light, striking the top of the atmosphere and triggering a shortwave radio blackout over the Atlantic Ocean and coastal areas. Figure 55 shows a map of the radio effect around 14.30 UT. According to data from the National Oceanic and Atmospheric Administration (NOAA) and NASA, a modest CME was launched with the flare; however, the sunspot that produced the flare was on the edge of the Sun's face, making it unlikely to be directed towards Earth.

The Kp- index, which ranges from 0 to 9, indicates disturbances in the horizontal component of the Earth's magnetic field, with 1 suggesting calm and ≥ 5 indicating a geomagnetic storm (Wing et al., 2005). However, the Kp-index for both events did not exceed 2; consequently, there was no impact on Earth.

5.2 Conclusion

Our vulnerability to space weather increases as society's reliance on technological systems grows. The goal of studying space weather at the beginning of the 25th solar cycle is to predict events and conditions in the Sun's near-Earth space that will have potentially harmful societal and economic consequences. To do so far enough ahead of time and with enough precision that preventive or mitigation actions can be implemented.

From the above discussion for our solar events of interest, we concluded that the strongest solar events, M4.4 and X1.59, which occurred at the beginning of the 25th solar cycle, had no significant impact on Earth. CMEs cause major geomagnetic storms, which cause powerful currents in the Earth's magnetosphere as well as changes in the radiation belts and ionosphere (Feng et al., 2020). However, although the solar events produced CME, the solar flare erupted from the sun's east limb, and the plasma cloud was aimed away from Earth. The mass difference between the injection time in the simulation and the direct detection result indicates that the particles took longer to reach space, making them weaker and having no effect on space weather. Despite the fact that M-class and X-class solar flares erupted at the beginning of the 25th solar cycle, the position and timing of the eruption resulted in modest space weather and the impact on Earth was mild.

REFERENCES



REFERENCES

- Anastasiadis, A. (2002). Acceleration of solar energetic particles: the case of solar flares. *Journal of Atmospheric and Solar-Terrestrial Physics*, 64(5-6), 481-488.
- Astronomy, L. c. f. E. S. a. (2021). The Sun. <http://www.lesa.biz/astronomy/solar-system/sun>
- Austin, H., & Savani, N. (2018). Skills for forecasting space weather. *Weather*, 73(11), 362-366.
- Baisri, P., Khumlumlert, T., & Aiemsa-Ad, N. (2017). Solar energetic particle propagation from solar flare. *Journal of Physics: Conference Series*,
- Baker, D. (1998). What is space weather? *Advances in Space Research*, 22(1), 7-16.
- Baker, D. N., Li, X., Pulkkinen, A., Ngwira, C., Mays, M., Galvin, A., & Simunac, K. (2013). A major solar eruptive event in July 2012: Defining extreme space weather scenarios. *Space Weather*, 11(10), 585-591.
- Balan, N., Batista, I., Tulasi Ram, S., & Rajesh, P. (2016). A new parameter of geomagnetic storms for the severity of space weather. *Geoscience Letters*, 3(1), 1-5.
- Bhowmik, P., & Nandy, D. (2018). Prediction of the strength and timing of sunspot cycle 25 reveal decadal-scale space environmental conditions. *Nature Communications*, 9(1), 1-10.
- Bhowmik, P., Yeates, A., & Rice, O. (2022). Exploring the Origin of Stealth Coronal Mass Ejections with Magnetofrictional Simulations. *Solar Physics*, 297(3), 1-24.
- Bieber, J. W., Droege, W., Evenson, P. A., Pyle, R., Ruffolo, D., Pinsook, U., Tooprakai, P., Rujiwarodom, M., Khumlumlert, T., & Krucker, S. (2002). Energetic particle observations during the 2000 July 14 solar event. *The Astrophysical Journal*, 567(1), 622.
- Bothmer, V., & Daglis, I. A. (2007). *Space weather: physics and effects*. Springer Science & Business Media.
- Bruevich, E., & Bruevich, V. (2018). Powerful Solar Flares in September 2017. Comparison with the Largest Flares in Cycle 24. *Astrophysics*, 61(2), 241-253.
- Burlaga, L., Klein, L., Sheeley Jr, N., Michels, D., Howard, R., Koomen, M.,

- Schwenn, R., & Rosenbauer, H. (1982). A magnetic cloud and a coronal mass ejection. *Geophysical research letters*, 9(12), 1317-1320.
- Byrne, J. P. (2012). The Kinematics and Morphology of Solar Coronal Mass Ejections. *arXiv preprint arXiv:1202.4005*.
- Camporeale, E., Wing, S., & Johnson, J. (2018). *Machine learning techniques for space weather*. Elsevier.
- Cannon, P., Angling, M., Barclay, L., Curry, C., Dyer, C., Edwards, R., Greene, G., Hapgood, M., Horne, R. B., & Jackson, D. (2013). *Extreme space weather: impacts on engineered systems and infrastructure*. Royal Academy of Engineering.
- Caroll, B. W., & Ostlie, D. A. (2017). *An Introduction to Modern Astrophysics* (2nd Edition ed.). Cambridge University Press.
- Center, A. S. (2013). Advanced Composition Explorer (ACE).
<http://www.srl.caltech.edu/ACE/>
- Cesar. (2016). *General Understanding of the Sun: Magnetic field, Structure and Sunspot cycle*
<https://www.cosmos.esa.int/documents/519784/1185714/booklet/61f849af-0b08-4a01-be80-6e1354fb135f>
- Chen, J. (2017). Physics of erupting solar flux ropes: coronal mass ejections (CMEs)—recent advances in theory and observation. *Physics of Plasmas*, 24(9), 090501.
- Chiu, M., Von-Mehlem, U., Willey, C., Betenbaugh, T., Maynard, J., Krein, J., Conde, R., Gray, W., Hunt, J., & Mosher, L. (1998). ACE spacecraft. *Space Science Reviews*, 86(1), 257-284.
- contributors, W. (2021). *Solar Energetic Particles*,. Wikipedia, The Free Encyclopedia. https://en.wikipedia.org/wiki/Solar_energetic_particles
- contributors, W. (2021, 18 May 2021 09:52 UTC). *Sun*.
<https://en.wikipedia.org/w/index.php?title=Special:CiteThisPage&page=Sun&id=1023784514&wpFormIdentifier=titleform>
- contributors, w. (2021). *Sun*. <https://en.wikipedia.org/wiki/Sun>
- contributors, W. (2021,). *Interplanetary magnetic field*.
https://en.wikipedia.org/wiki/Interplanetary_magnetic_field#:~:text=The%20i

interplanetary%20magnetic%20field%20(IMF,to%20fill%20the%20Solar%20System.

Council, N. R. (1930). *Understanding the Sun and Solar System Plasmas: Future Directions in Solar and Space Physics.*

Cruz-Uribe, D., & Neugebauer, C. J. (2003). An Elementary Proof of Error Estimates for the Trapezoidal Rule. *Mathematics Magazine*, 76.

<https://doi.org/10.2307/3219088>

cycle, S. (2021). *Solar Cycle*. https://en.wikipedia.org/wiki/Solar_cycle

David J. Griffiths. (1999). *Introduction to electrodynamics*. Prentice-Hall International, Inc.

Davis, P. J., & Rabinowitz, P. (2007). *Methods of numerical integration*. Courier Corporation.

Dennis, B. R., & Schwartz, R. A. (1989). Solar flares: The impulsive phase. International Astronomical Union Colloquium,

Desai, M., & Giacalone, J. (2016). Large gradual solar energetic particle events. *Living reviews in solar physics*, 13(1), 1-132.

Dr. David H. Hathaway. (2015). *Solar Physics*.

<https://solarscience.msfc.nasa.gov/interior.shtml>

Dröge, W. (2003). Acceleration and propagation of solar energetic particles. In *Energy Conversion and Particle Acceleration in the Solar Corona* (pp. 193-212). Springer.

Du, Z. (2021). Variations in the Correlations of Acceleration and Force of Slow and Fast CMEs with Solar Activity during Solar Cycles 23–24. *Solar Physics*, 296(2), 1-17.

Eastwood, J., Biffis, E., Hapgood, M., Green, L., Bisi, M., Bentley, R., Wicks, R., McKinnell, L. A., Gibbs, M., & Burnett, C. (2017). The economic impact of space weather: Where do we stand? *Risk Analysis*, 37(2), 206-218.

Eastwood, J., Biffis, E., Hapgood, M., Green, L., Bisi, M., Bentley, R., Wicks, R., McKinnell, L. A., Gibbs, M., & Burnett, C. (2017). The economic impact of space weather: Where do we stand? *Risk Analysis*, 37(2), 206-218.

Eroglu, E. (2019). Modeling the superstorm in the 24th solar cycle. *Earth, Planets and Space*, 71(1), 1-12.

- Feng, L., Gan, W., Liu, S., Wang, H., Li, H., Xu, L., Zong, W., Zhang, X., Zhu, Y., & Wu, H. (2020). Space weather related to solar eruptions with the ASO-S mission. *Frontiers in Physics*, 8, 45.
- Firoz, K., Cho, K. S., Hwang, J., Phani Kumar, D., Lee, J., Oh, S., Kaushik, S. C., Kudela, K., Rybanský, M., & Dorman, L. I. (2010). Characteristics of ground-level enhancement-associated solar flares, coronal mass ejections, and solar energetic particles. *Journal of Geophysical Research: Space Physics*, 115(A9).
- Fisher, D. K. (2021). Solar Wind.
<https://www.jpl.nasa.gov/nmp/st5/SCIENCE/solarwind.html>
- Fry, E. K. (2012). The risks and impacts of space weather: Policy recommendations and initiatives. *Space Policy*, 28(3), 180-184.
- Gan, Z., Xing, X., & Xu, Z. (2012). Effects of image charges, interfacial charge discreteness, and surface roughness on the zeta potential of spherical electric double layers. *The Journal of chemical physics*, 137(3), 034708.
- Georgoulis, M. K., Nindos, A., & Zhang, H. (2019). The source and engine of coronal mass ejections. *Philosophical Transactions of the Royal Society A*, 377(2148), 20180094.
- Golub, L., & Pasachoff, J. M. (2010). *The solar corona*. Cambridge University Press.
- Gonzalez, W. D., Tsurutani, B. T., & Clúa de Gonzalez, A. L. (1999). Interplanetary origin of geomagnetic storms. *Space Science Reviews*, 88(3), 529-562.
- Gopalswamy, N., Yashiro, S., Krucker, S., Stenborg, G., & Howard, R. A. (2004). Intensity variation of large solar energetic particle events associated with coronal mass ejections. *Journal of Geophysical Research: Space Physics*, 109(A12).
- Gorney, D. (1990). Solar cycle effects on the near-Earth space environment. *Reviews of Geophysics*, 28(3), 315-336.
- Gosling, J., Hildner, E., MacQueen, R., Munro, R., Poland, A., & Ross, C. (1976). The speeds of coronal mass ejection events. *Solar Physics*, 48(2), 389-397.
- Gosling, J., McComas, D., Phillips, J., & Bame, S. (1991). Geomagnetic activity associated with Earth passage of interplanetary shock disturbances and coronal mass ejections. *Journal of Geophysical Research: Space Physics*, 96(A5), 7831-7839.

- Gosling, J. T. (1997). Interplanetary magnetic field, In: Encyclopedia of Planetary Science. Encyclopedia of Earth Science., 342-343. https://doi.org/10.1007/1-4020-4520-4_189
- Hanslmeier, A. (2010). The sun and space weather. In *Heliophysical Processes* (pp. 233-249). Springer.
- Hapgood, M. (2018). Societal and economic importance of space weather. In *Machine learning techniques for space weather* (pp. 3-26). Elsevier.
- Harvey, K. L., & White, O. R. (1999). What is solar cycle minimum? *Journal of Geophysical Research: Space Physics*, 104(A9), 19759-19764.
- Hathaway, D. H. (2015). The solar cycle. *Living reviews in solar physics*, 12(1), 1-87.
- Holman, G. D. (2006). The mysterious origins of solar flares. *Scientific American*, 294(4), 38-45.
- Ishkov, V. (2018). Space weather and specific features of the development of current solar cycle. *Geomagnetism and aeronomy*, 58(6), 753-767.
- Joshua, B., Oladipo, O., Adamu, J., Adebisi, S., & Ikubanni, S. (2018). CORRELATION BETWEEN SUNSPOT NUMBER AND GEOMAGNETIC STORM. *Equity Journal of Science and Technology*, 5(1), 157-161.
- Kappenman, J. G. (1996). Geomagnetic storms and their impact on power systems. *IEEE Power Engineering Review*, 16(5).
- Kilcik, A., Yurchyshyn, V., Abramenko, V., Goode, P., Gopalswamy, N., Özgüç, A., & Rozelot, J. Maximum CME speed as an indicator of solar and geomagnetic activities View all abstracts by submitter.
- Klein, K.-L., & Dalla, S. (2017). Acceleration and propagation of solar energetic particles. *Space Science Reviews*, 212(3), 1107-1136.
- Koons, H., Mazur, J., Selesnick, R., Blake, J., & Fennell, J. (1999). *The impact of the space environment on space systems*.
- Kreyszig, E. (2011). *Advanced engineering mathematics* (10 ed.). John Wiley & sons, Inc.
- Kumar, S., & Singh, A. (2012). Effect of solar flares on ionospheric TEC at Varanasi, near EIA crest, during solar minimum period. *94.20. dt; 96.60. qe*.
- Künzel, H. (1962). M. Waldmeier: The sunspot-activity in the years 1610-1960. Zürich 1961: Verlag Schulthess u. Co. AG. In: Wiley Online Library.

- Kutner, M. L. (2012). *Astronomy (A physical Perspective)*. Cambridge University Press.
- Lin, J., & Forbes, T. (2000). Effects of reconnection on the coronal mass ejection process. *Journal of Geophysical Research: Space Physics*, *105*(A2), 2375-2392.
- Liou, K., Wu, C.-C., Dryer, M., Wu, S.-T., Rich, N., Plunkett, S., Simpson, L., Fry, C. D., & Schenk, K. (2014). Global simulation of extremely fast coronal mass ejection on 23 July 2012. *Journal of Atmospheric and Solar-Terrestrial Physics*, *121*, 32-41.
- Liu, J., Wang, W., Qian, L., Lotko, W., Burns, A. G., Pham, K., Lu, G., Solomon, S. C., Liu, L., & Wan, W. (2021). Solar flare effects in the Earth's magnetosphere. *Nature Physics*, *17*(7), 807-812.
- Mann, G., Klassen, A., Aurass, H., & Classen, H.-T. (2003). Formation and development of shock waves in the solar corona and the near-Sun interplanetary space. *Astronomy & Astrophysics*, *400*(1), 329-336.
- Masuda, S., Kosugi, T., Hara, H., Tsuneta, S., & Ogawara, Y. (1994). A loop-top hard X-ray source in a compact solar flare as evidence for magnetic reconnection. *Nature*, *371*(6497), 495-497.
- Matzka, J., Stolle, C., Yamazaki, Y., Bronkalla, O., & Morschhauser, A. (2021). The geomagnetic Kp index and derived indices of geomagnetic activity. *Space Weather*, *19*(5), e2020SW002641.
- McGinnis, J. A. (2016). *Impacts of solar cycle and uncertainty in solar activity predictions on spacecraft in earth orbit*. University of Houston-Clear Lake.
- Messerotti, M., Zuccarello, F., Guglielmino, S. L., Bothmer, V., Lilensten, J., Noci, G., Storini, M., & Lundstedt, H. (2009). Solar weather event modelling and prediction. *Space Science Reviews*, *147*(3), 121-185.
- Meyer-Vernet, N. (2007). *Basics of the solar wind*. Cambridge University Press.
- Mike Hapgood. (2018). Chapter 1-Societal and Economic Importance of Space Weather, . *Elsevier*, 3-26,.
(<https://www.sciencedirect.com/science/article/pii/B9780128117880000019>)
- Morosan, D. E., Carley, E. P., Hayes, L. A., Murray, S. A., Zucca, P., Fallows, R. A., McCauley, J., Kilpua, E. K., Mann, G., & Vocks, C. (2019). Multiple regions

- of shock-accelerated particles during a solar coronal mass ejection. *Nature Astronomy*, 3(5), 452-461.
- Möstl, C., Rollett, T., Frahm, R. A., Liu, Y. D., Long, D. M., Colaninno, R. C., Reiss, M. A., Temmer, M., Farrugia, C. J., & Posner, A. (2015). Strong coronal channelling and interplanetary evolution of a solar storm up to Earth and Mars. *Nature Communications*, 6(1), 1-10.
- NASA. (2021). Space Technology 5.
<https://www.jpl.nasa.gov/nmp/st5/SCIENCE/solarwind.html>
- NASA. (2021). *What is Solar Cycle?* <https://spaceplace.nasa.gov/solar-cycles/en/>
- NASA. (2021). *What is Solar Flare?* <https://hesperia.gsfc.nasa.gov/sftheory/flare.htm>
- NASA. (2013). *Advanced Composition Explorer (ACE)*,
<http://www.srl.caltech.edu/ACE/>
- Ngwira, C. M., Pulkkinen, A., Leila Mays, M., Kuznetsova, M. M., Galvin, A., Simunac, K., Baker, D. N., Li, X., Zheng, Y., & Gloer, A. (2013). Simulation of the 23 July 2012 extreme space weather event: What if this extremely rare CME was Earth directed? *Space Weather*, 11(12), 671-679.
- Nitta, N. V., Mulligan, T., Kilpua, E. K., Lynch, B. J., Mierla, M., O’Kane, J., Pagano, P., Palmerio, E., Pomoell, J., & Richardson, I. G. (2021). Understanding the origins of problem geomagnetic storms associated with “stealth” coronal mass ejections. *Space Science Reviews*, 217(8), 1-53.
- NOAA. (2016). Space Weather: Storms from the Sun.
<https://www.noaa.gov/explainers/space-weather-storms-from-sun>
- NOAA. (2021). *Coronal Mass Ejection*,.
- Owens, M. J., Lockwood, M., & Barnard, L. A. (2020). The value of CME arrival time forecasts for space weather mitigation. *Space Weather*, 18(9), e2020SW002507.
- Owens, M. J., Lockwood, M., Barnard, L. A., Scott, C. J., Haines, C., & Macneil, A. (2021). Extreme space-weather events and the solar cycle. *Solar Physics*, 296(5), 1-19.
- Owoeye, K. Space Weather Effects of the September 6, 2017 Solar Event (March 2018).
- Paluk, & al, e. (2017). The solar energetic particle propagation of solar flare events on

- 24th solar cycle. *Journal of Physics: Conference Series*,
- Pande, B., Pande, S., Chandra, R., & Mathpal, M. C. (2018). Solar flares, CMEs and solar energetic particle events during solar cycle 24. *Advances in Space Research*, 61(2), 777-785.
- Paul, A., Roy, B., Ray, S., Das, A., & DasGupta, A. (2011). Characteristics of intense space weather events as observed from a low latitude station during solar minimum. *Journal of Geophysical Research: Space Physics*, 116(A10).
- Petrovay, K. (2010). Solar cycle prediction. *Living reviews in solar physics*, 7(1), 1-59.
- Petukhova, A., Petukhov, I., Petukhov, S., & Ksenofontov, L. (2017). Solar energetic particle acceleration by a shock wave accompanying a coronal mass ejection in the solar atmosphere. *The Astrophysical Journal*, 836(1), 36.
- Pogorelov, N., Borovikov, S., Kryukov, I., Wu, S., Yalim, M., Colella, P., & Van Straalen, B. (2017). Modeling coronal mass ejections with the multi-scale fluid-kinetic simulation suite. *Journal of Physics: Conference Series*,
- Rathore, B., Kaushik, S., Bhadoria, R., Parashar, K., & Gupta, D. (2012). Sunspots and geomagnetic storms during solar cycle-23. *Indian Journal of Physics*, 86(7), 563-567.
- Reames, D. (2004). Solar energetic particle variations. *Advances in Space Research*, 34(2), 381-390.
- Reames, D. V. (1999). Particle acceleration at the Sun and in the heliosphere. *Space Science Reviews*, 90(3), 413-491.
- Reames, D. V. (2013). The two sources of solar energetic particles. *Space Science Reviews*, 175(1), 53-92.
- Reep, J. W., & Knizhnik, K. J. (2019). What determines the X-ray intensity and duration of a solar flare? *The Astrophysical Journal*, 874(2), 157.
- Reyes, P. I., Pinto, V. A., & Moya, P. S. (2021). Geomagnetic Storm Occurrence and Their Relation With Solar Cycle Phases. *Space Weather*, 19(9), e2021SW002766.
- Ruffolo, D. (1994). Effect of adiabatic deceleration on the focused transport of solar cosmic rays. *arXiv preprint astro-ph/9408056*.
- Ruffolo, D. (2002). Classification of solar energetic particles. *Advances in Space*

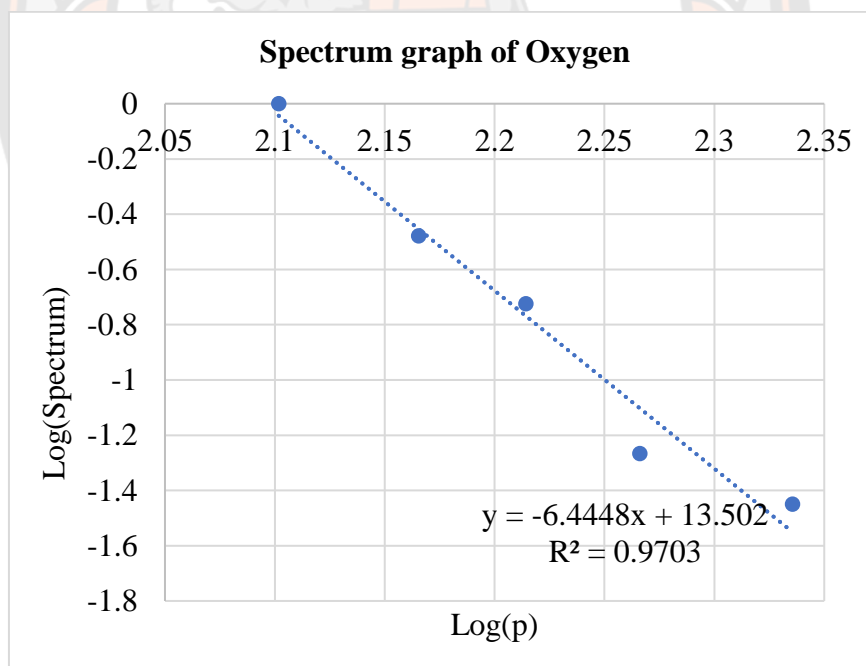
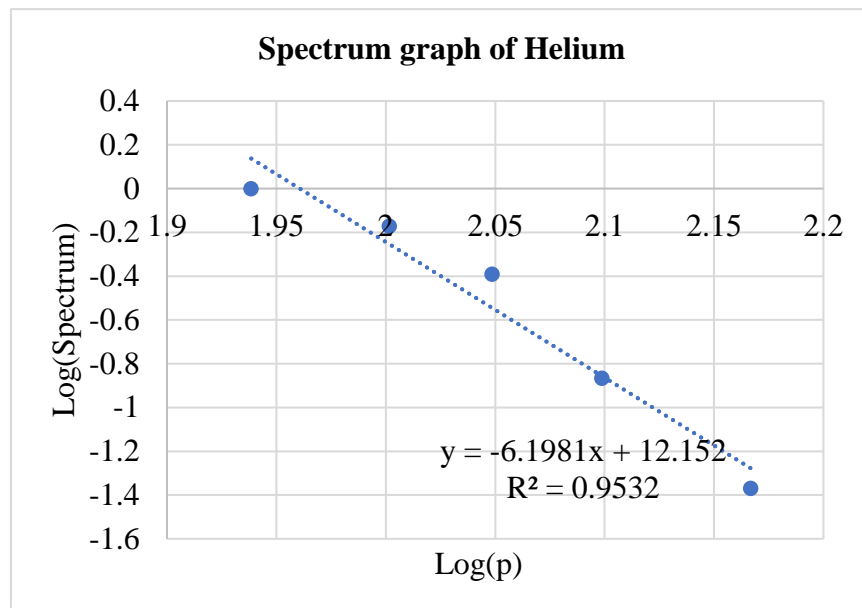
- Research*, 30(1), 45-54.
- Ruffolo, D., Khumlumlert, T., & Youngde, W. (1998). Deconvolution of interplanetary transport of solar energetic particles. *Journal of Geophysical Research: Space Physics*, 103(A9), 20591-20602.
- Ruffolo, d., Pinsook, u., Tooprakai, p., Rujiwarodom, m., & Khumlumlert, t. (2002). Energetic particle observations during the 2000 July 14 solar event john w. Bieber, Wolfgang droége, paul a. Evenson, and roger pyle. *The astrophysical journal*, 567(622), 634.
- Ruffolo, D., Tooprakai, P., Rujiwarodom, M., Khumlumlert, T., Wechakama, M., Bieber, J. W., Evenson, P., & Pyle, R. (2006). Relativistic solar protons on 1989 October 22: Injection and transport along both legs of a closed interplanetary magnetic loop. *The Astrophysical Journal*, 639(2), 1186.
- Ruzmaikin, A., Feynman, J., & Stoev, S. (2011). Distribution and clustering of fast coronal mass ejections. *Journal of Geophysical Research: Space Physics*, 116(A4).
- Sáiz, A., Evenson, P., Ruffolo, D., & Bieber, J. W. (2005). On the estimation of solar energetic particle injection timing from onset times near Earth. *The Astrophysical Journal*, 626(2), 1131.
- Sato, H., Jakowski, N., Berdermann, J., Jiricka, K., Heßelbarth, A., Banyś, D., & Wilken, V. (2019). Solar radio burst events on 6 September 2017 and its impact on GNSS signal frequencies. *Space Weather*, 17(6), 816-826.
- Schrijver, C. J., Kauristie, K., Aylward, A. D., Denardini, C. M., Gibson, S. E., Glover, A., Gopalswamy, N., Grande, M., Hapgood, M., & Heynderickx, D. (2015). Understanding space weather to shield society: A global road map for 2015–2025 commissioned by COSPAR and ILWS. *Advances in Space Research*, 55(12), 2745-2807.
- Schwenn, R., Dal Lago, A., Huttunen, E., & Gonzalez, W. D. (2005). The association of coronal mass ejections with their effects near the Earth. *Annales Geophysicae*,
- Sharma, R., & Mehta, C. (2003). Double-diffusive convection in compressible Walters' B'elastico-viscous fluid in hydromagnetics. *Indian Journal of Physics*, 77, 657-661.

- Singh, A., Siingh, D., & Singh, R. (2010). Space weather: physics, effects and predictability. *Surveys in geophysics*, 31(6), 581-638.
- Singh, A. K., Bhargawa, A., Siingh, D., & Singh, R. P. (2021). Physics of Space Weather Phenomena: A Review. *Geosciences*, 11(7), 286.
- Space. (2021). *What is Solar Wind?* <https://www.space.com/22215-solar-wind.html>
- Spaceweather. (2006). The classification of X-ray solar flares. <https://spaceweather.com/glossary/flareclasses.html>
- Srivastava, N., & Venkatakrisnan, P. (2002). Relationship between CME speed and geomagnetic storm intensity. *Geophysical research letters*, 29(9), 1-1-1-4.
- State key Laboratory of space weather. (2007). What is Interplanetary Magnetic Field (IMF)? <https://www.spaceweather.ac.cn/chinese/knowledge/knowledge1.htm>
- Storini, M., Bazilevskaya, G., Fluckiger, E., Krainev, M., Makhmutov, V., & Sladkova, A. (2003). The Gnevyshev gap: A review for space weather. *Advances in Space Research*, 31(4), 895-900.
- Subedi, P., Sonsrtee, W., Blasi, P., Ruffolo, D., Matthaeus, W., Montgomery, D., Chuychai, P., Dmitruk, P., Wan, M., & Parashar, T. N. (2017). Charged particle diffusion in isotropic random magnetic fields. *The Astrophysical Journal*, 837(2), 140.
- Sun, Y., Xie, Z., Chen, Y., Huang, X., & Hu, Q. (2021). Solar Wind Speed Prediction With Two-Dimensional Attention Mechanism. *Space Weather*, 19(7), e2020SW002707.
- Svestka, Z. (2012). *Solar flares* (Vol. 8). Springer Science & Business Media.
- Tandberg-Hanssen, E., & Emslie, A. G. (1988). *The physics of solar flares* (Vol. 14). Cambridge University Press.
- Tassev, Y., Velinov, P., Tomova, D., & Mateev, L. (2017). Analysis of extreme solar activity in early september 2017: G4–severe geomagnetic storm (07–08.09) and GLE72 (10.09) in solar minimum. *Compt. rend. Acad. bulg. Sci*, 70(10), 1437-1444.
- Thompson, B., Plunkett, S., Gurman, J., Newmark, J., St. Cyr, O., & Michels, D. (1998). SOHO/EIT observations of an Earth-directed coronal mass ejection on May 12, 1997. *Geophysical research letters*, 25(14), 2465-2468.
- Vilmer, N. (2012). Solar flares and energetic particles. *Philosophical Transactions of*

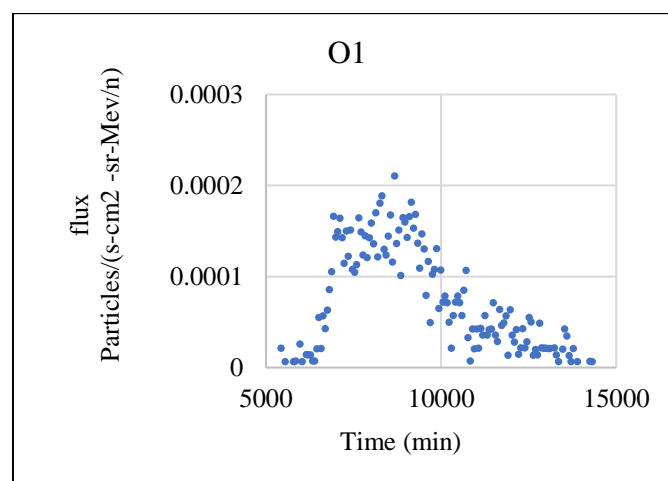
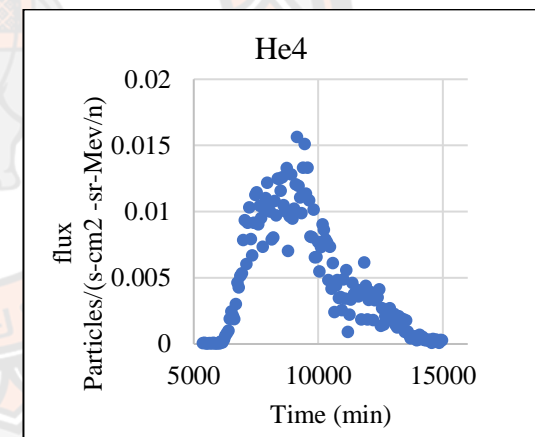
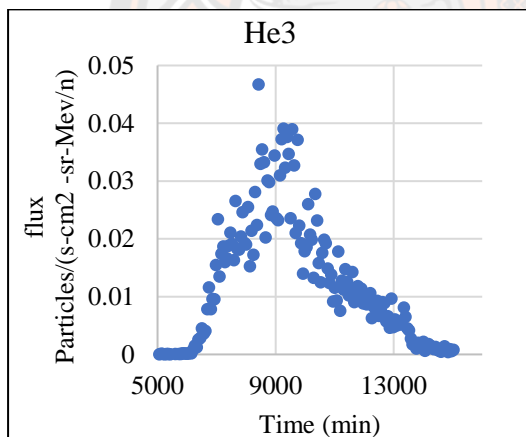
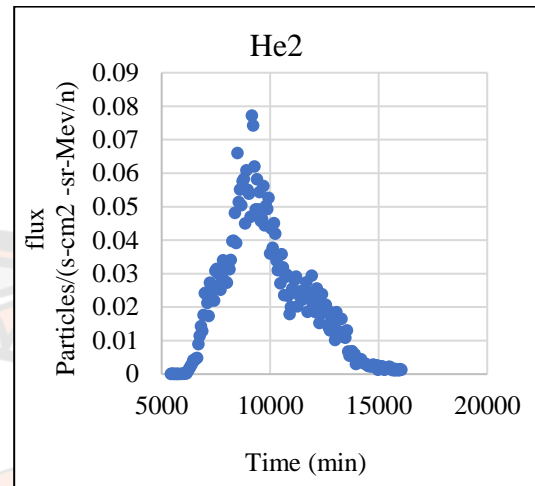
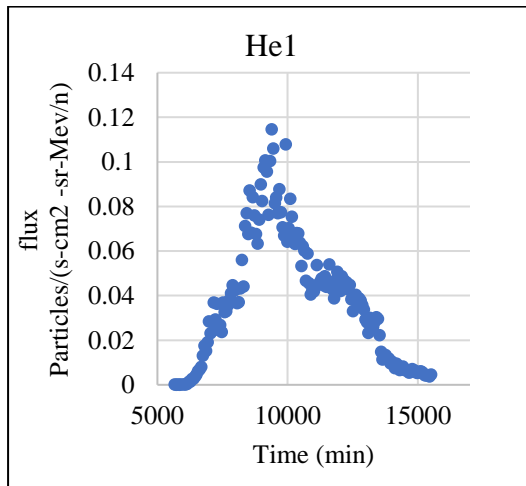
- the Royal Society A: Mathematical, Physical and Engineering Sciences*, 370(1970), 3241-3268.
- Webb, D. F., & Howard, T. A. (2012). Coronal mass ejections: Observations. *Living reviews in solar physics*, 9(1), 1-83.
- Webb, D. F., & Howard, T. A. (2012). Coronal mass ejections: Observations. *Living reviews in solar physics*, 9(1), 1-83.
- Wikipedia, T. F. E. (2021). Coronal mass ejection.
https://en.wikipedia.org/w/index.php?title=Coronal_mass_ejection&oldid=1020572284
- Wikiwand. (2019). Spherical coordinate system.
https://www.wikiwand.com/en/Spherical_coordinate_system#/Plotting
- Wing, S., Johnson, J., Jen, J., Meng, C. I., Sibeck, D., Bechtold, K., Freeman, J., Costello, K., Balikhin, M., & Takahashi, K. (2005). Kp forecast models. *Journal of Geophysical Research: Space Physics*, 110(A4).
- Wu, C. C., & Lepping, R. (2002). Effect of solar wind velocity on magnetic cloud-associated magnetic storm intensity. *Journal of Geophysical Research: Space Physics*, 107(A11), SSH 3-1-SSH 3-4.
- Wyper, P. F., Antiochos, S. K., & DeVore, C. R. (2017). A universal model for solar eruptions. *Nature*, 544(7651), 452-455.
- Yasyukevich, Y., Astafyeva, E., Padokhin, A., Ivanova, V., Syrovatskii, S., & Podlesnyi, A. (2018). The 6 September 2017 X-class solar flares and their impacts on the ionosphere, GNSS, and HF radio wave propagation. *Space Weather*, 16(8), 1013-1027.
- Yeh, S.-T. (2002). Using trapezoidal rule for the area under a curve calculation. *Proceedings of the 27th Annual SAS® User Group International (SUGI'02)*.
- Zhao, X., & Dryer, M. (2014). Current status of CME/shock arrival time prediction. *Space Weather*, 12(7), 448-469.
- Zwaan, C. (1968). The structure of sunspots. *Annual Review of Astronomy and Astrophysics*, 6, 135.



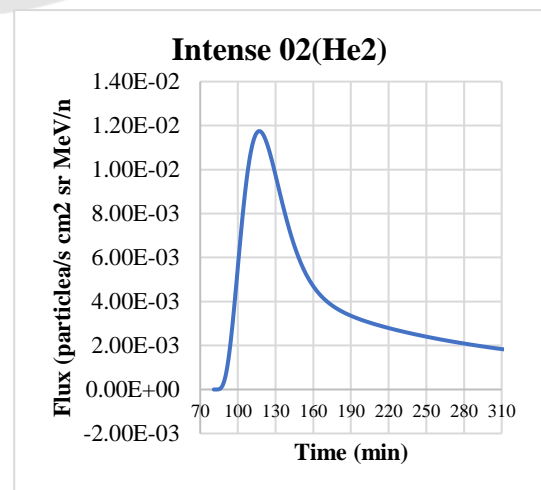
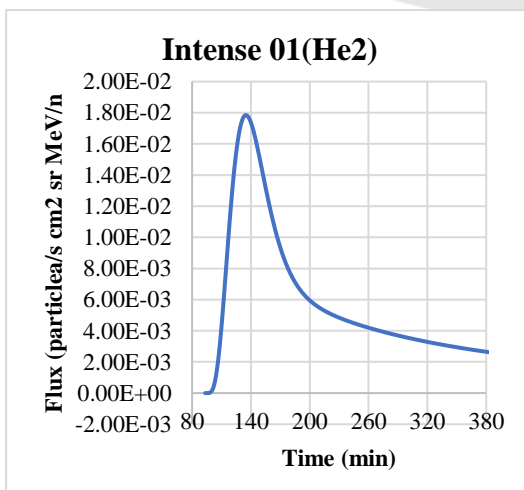
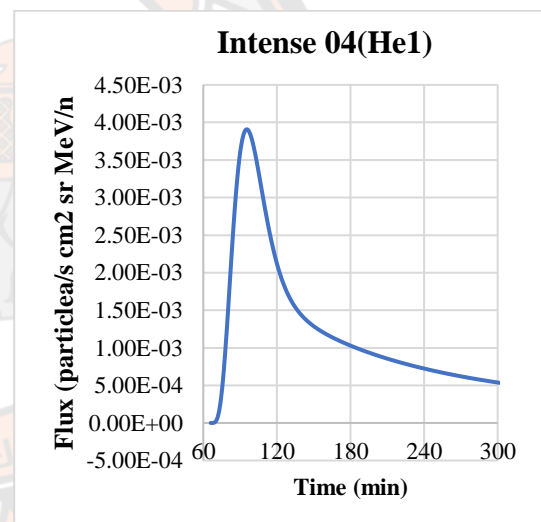
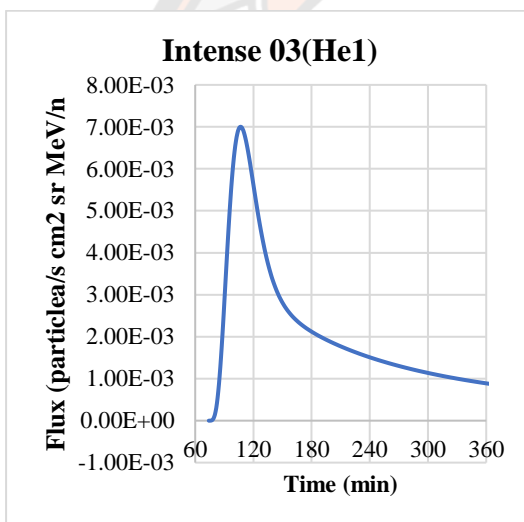
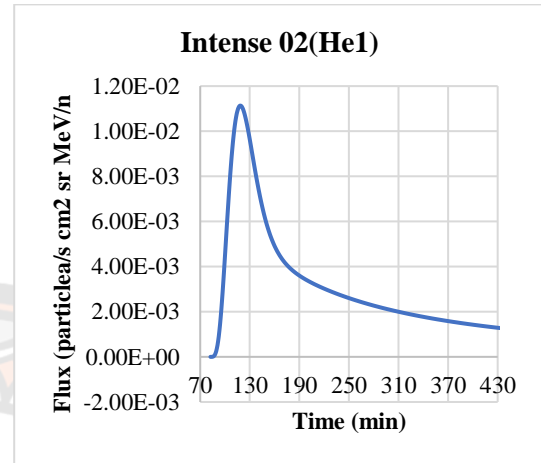
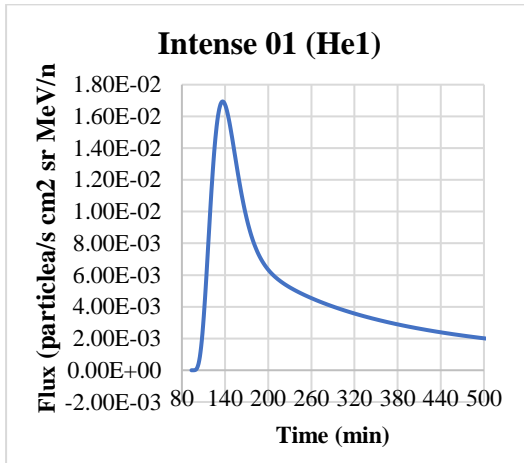
APPENDIX A SPECTRUM GRAPH OF THE PARTICLES



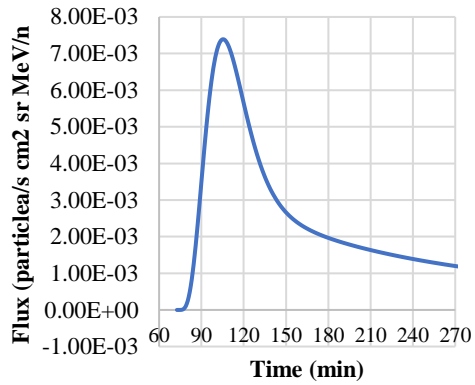
**APPENDIX B PARTICLE DENSITY AND TIME VALUE GRAPHS FOR THE
29 NOVEMBER 2020 EVENT FOR THE DATA COLLECTED
FROM THE SPACECRAFT**



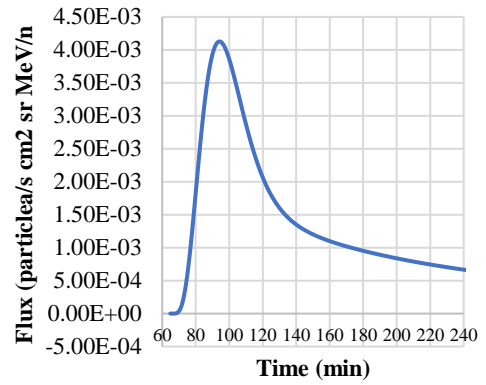
**APPENDIX C INTENSE GRAPH FROM THE SIMULATION OF THE DATA
OF 29 NOVEMBER 2020 EVENT**



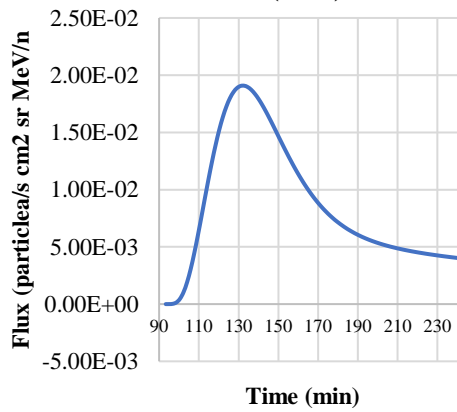
Intense 03 (He2)



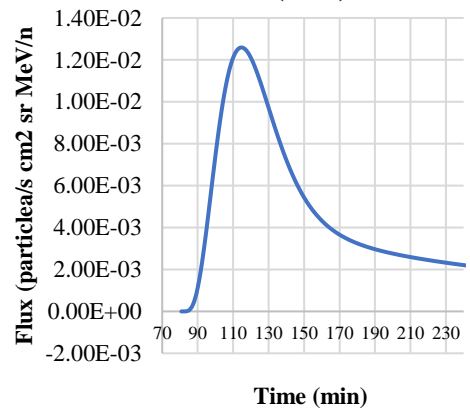
Intense 04 (He2)



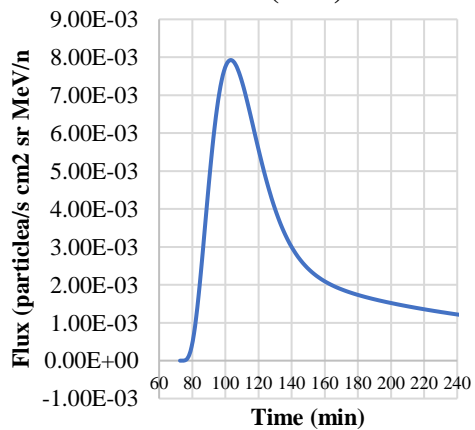
Intense 01(He3)



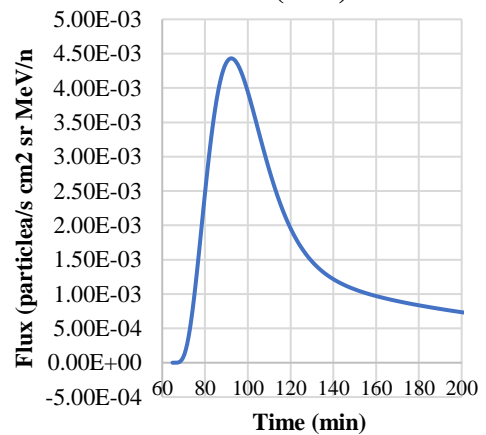
Intense 02(He3)

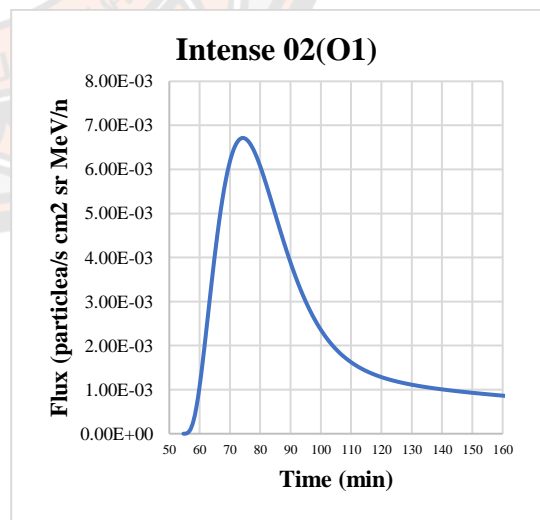
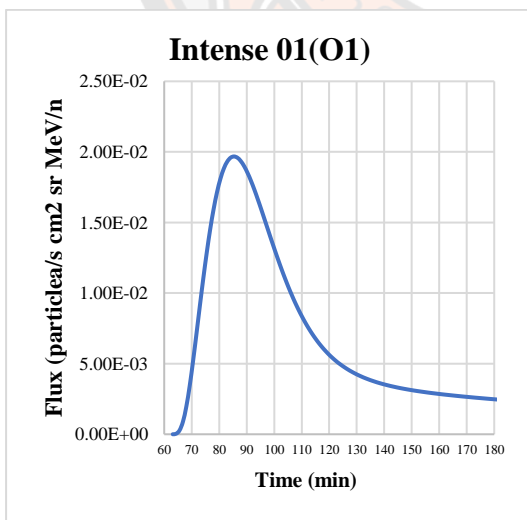
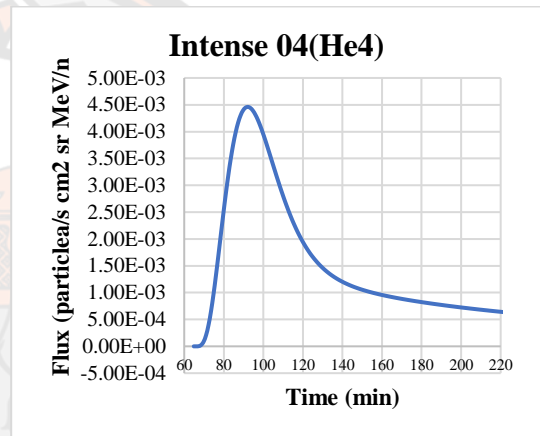
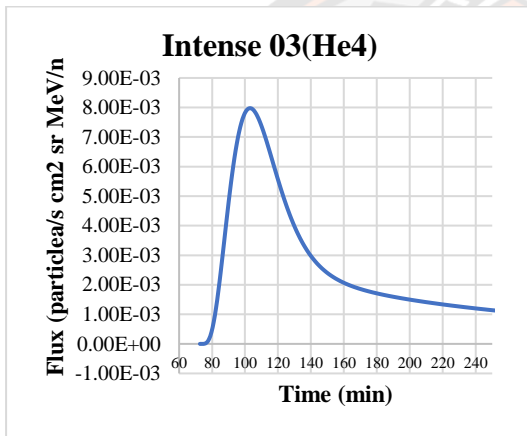
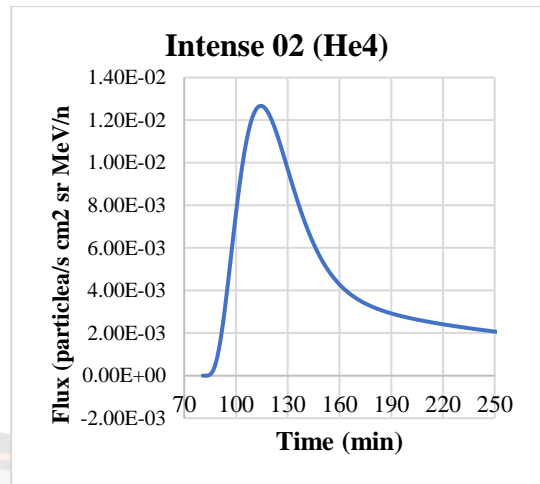
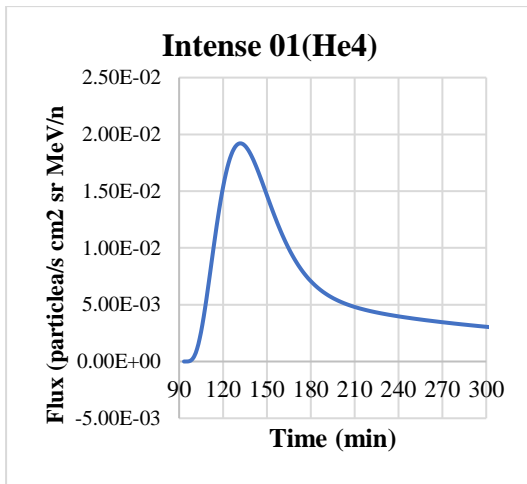


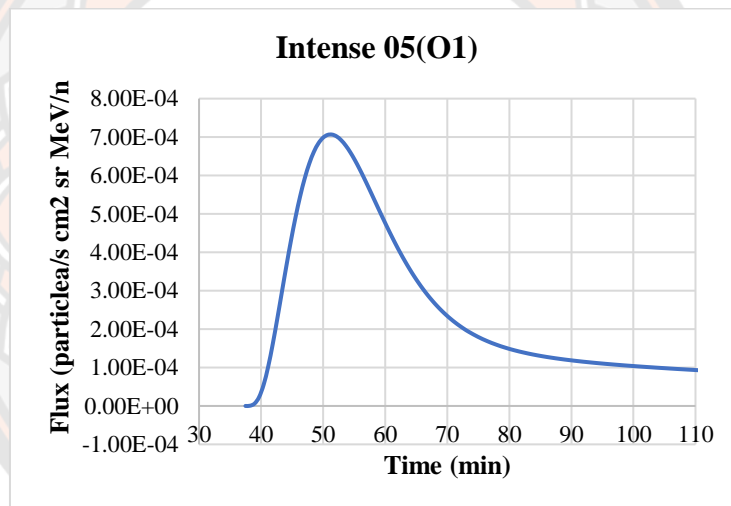
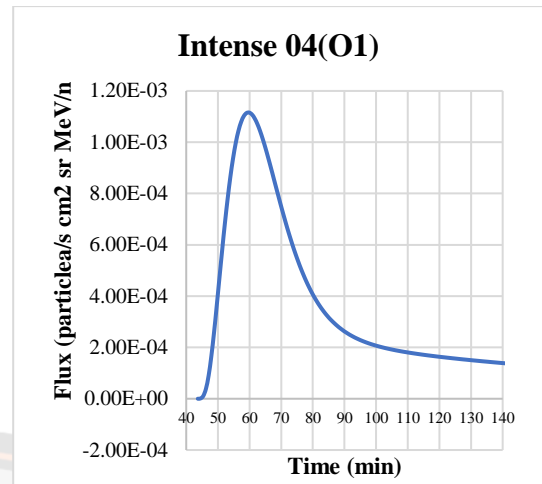
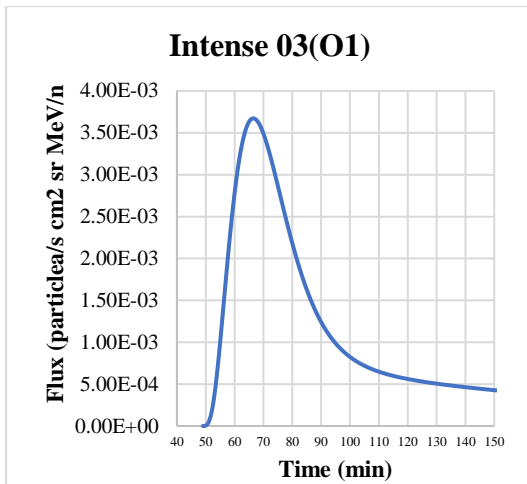
Intense 03(He3)



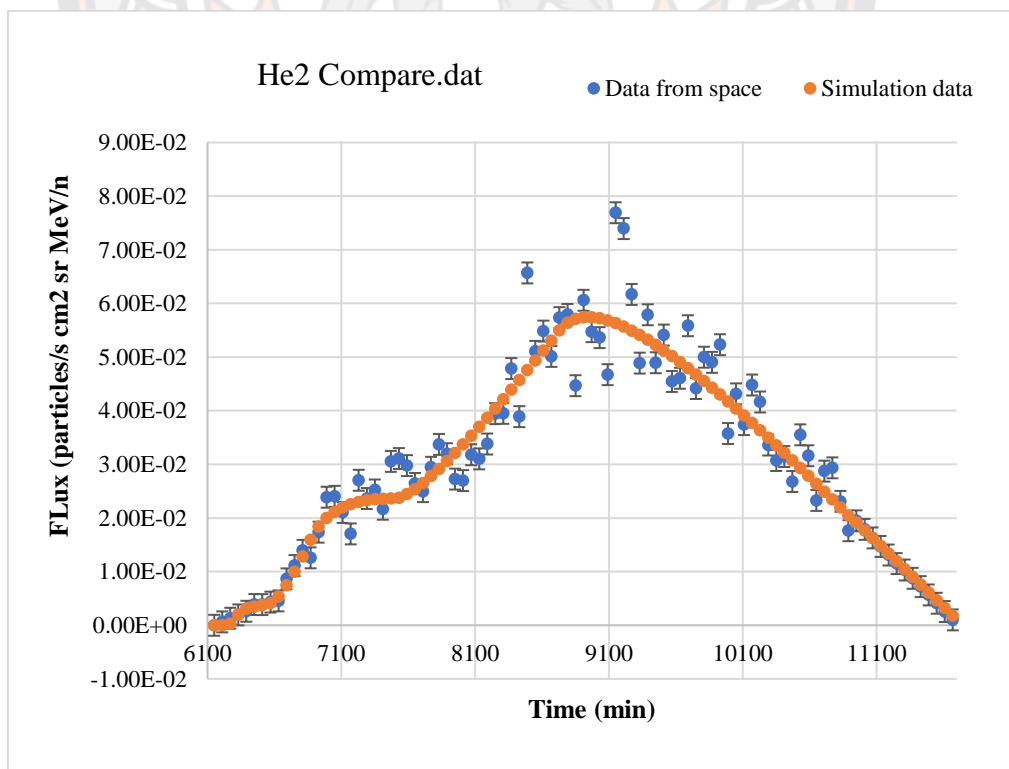
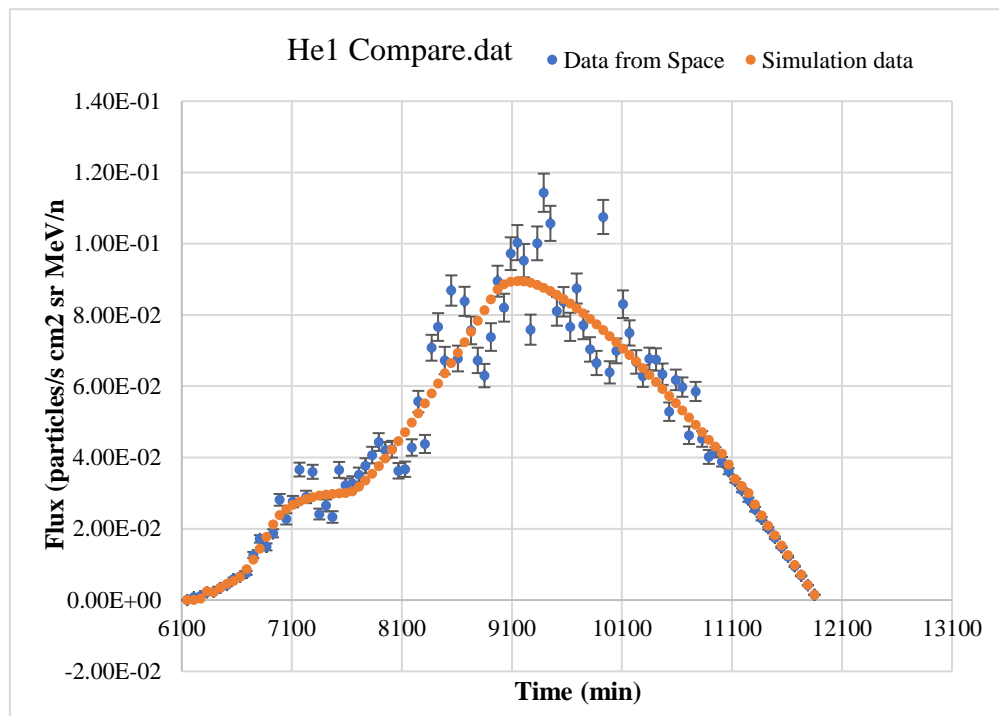
Intense 04(He3)

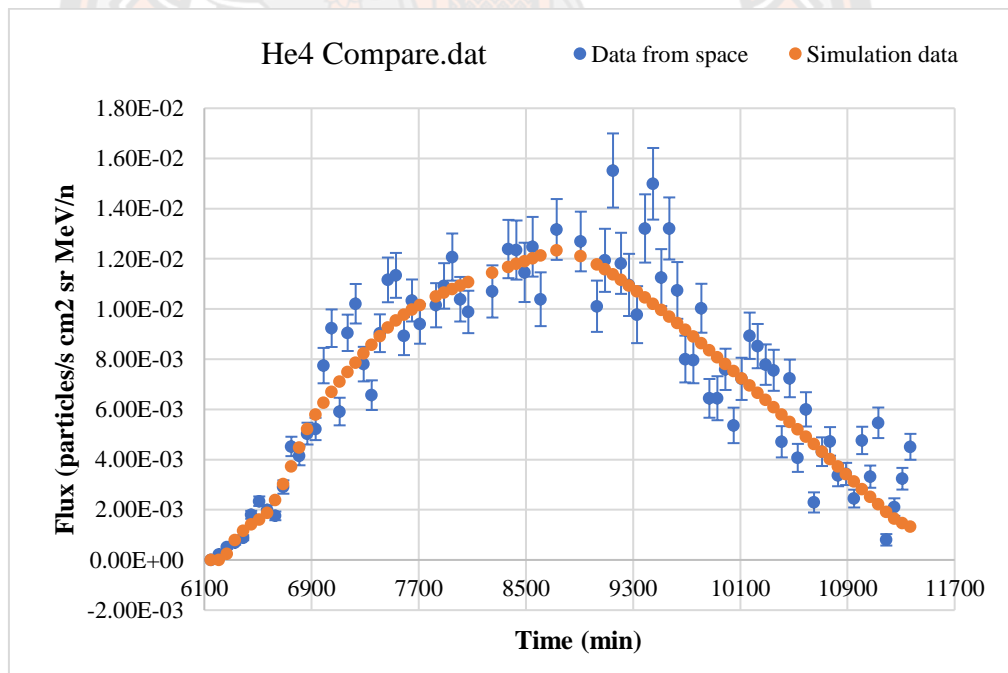
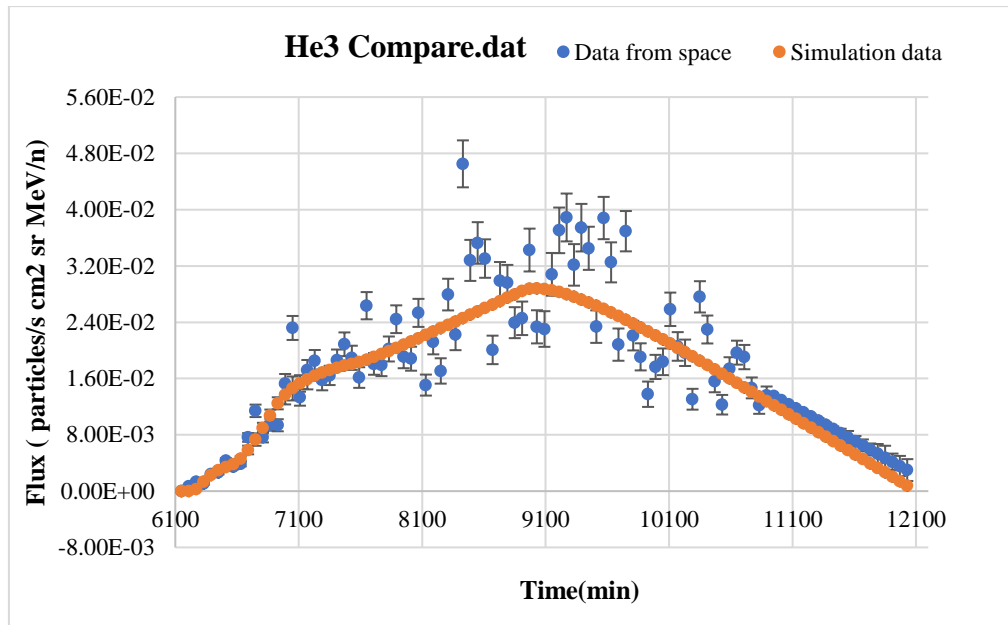


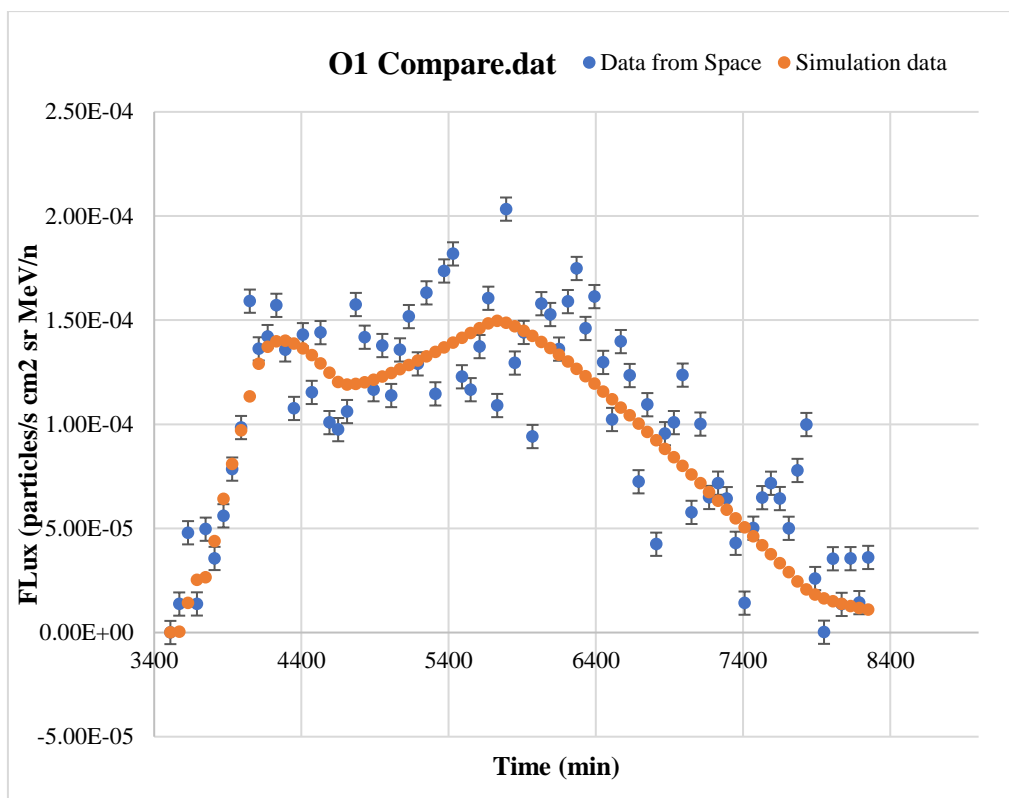




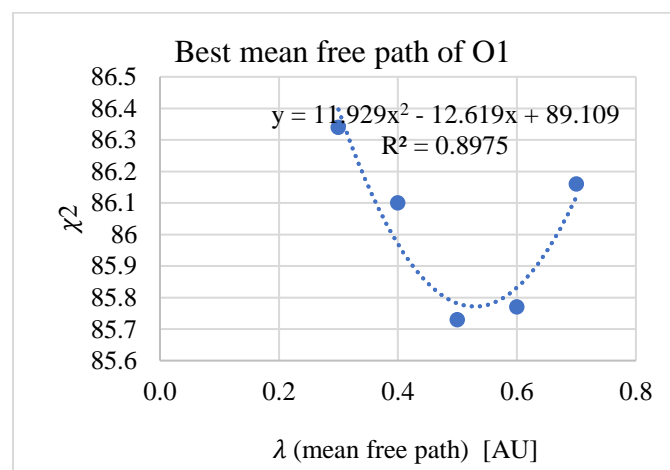
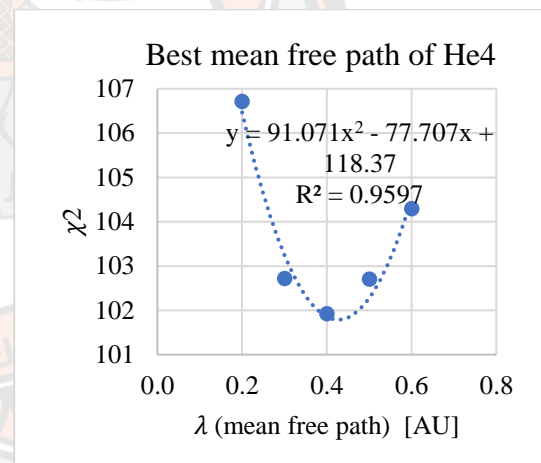
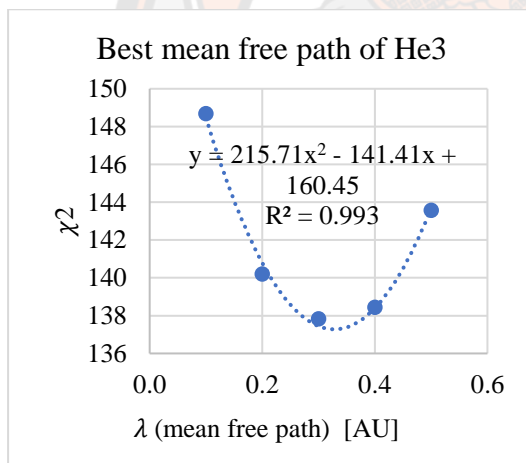
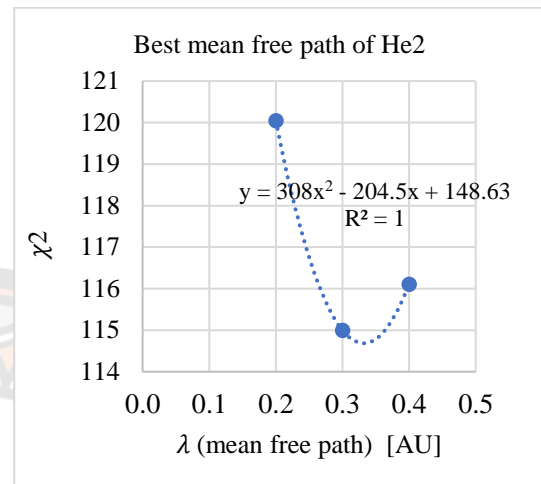
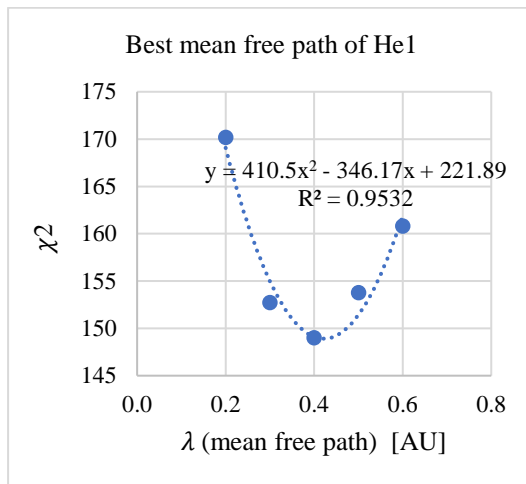
APPENDIX D COMPARE GRAPH FOR THE 29 NOVEMBER 2020 EVENT



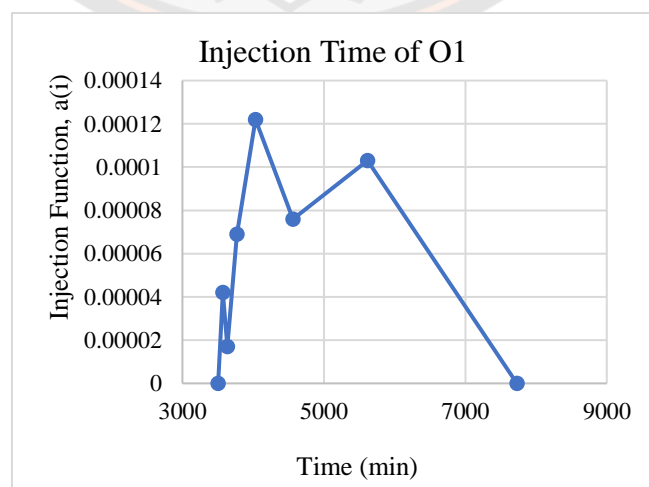
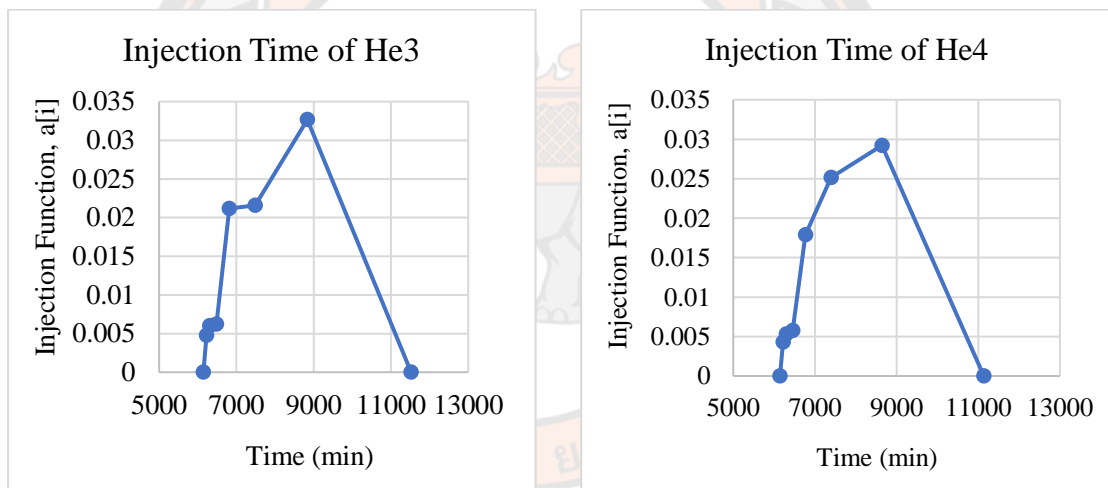
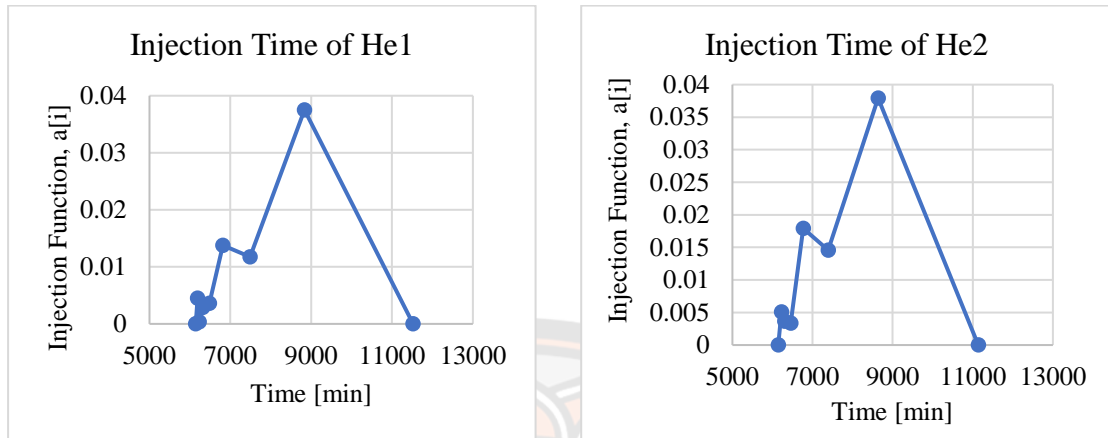




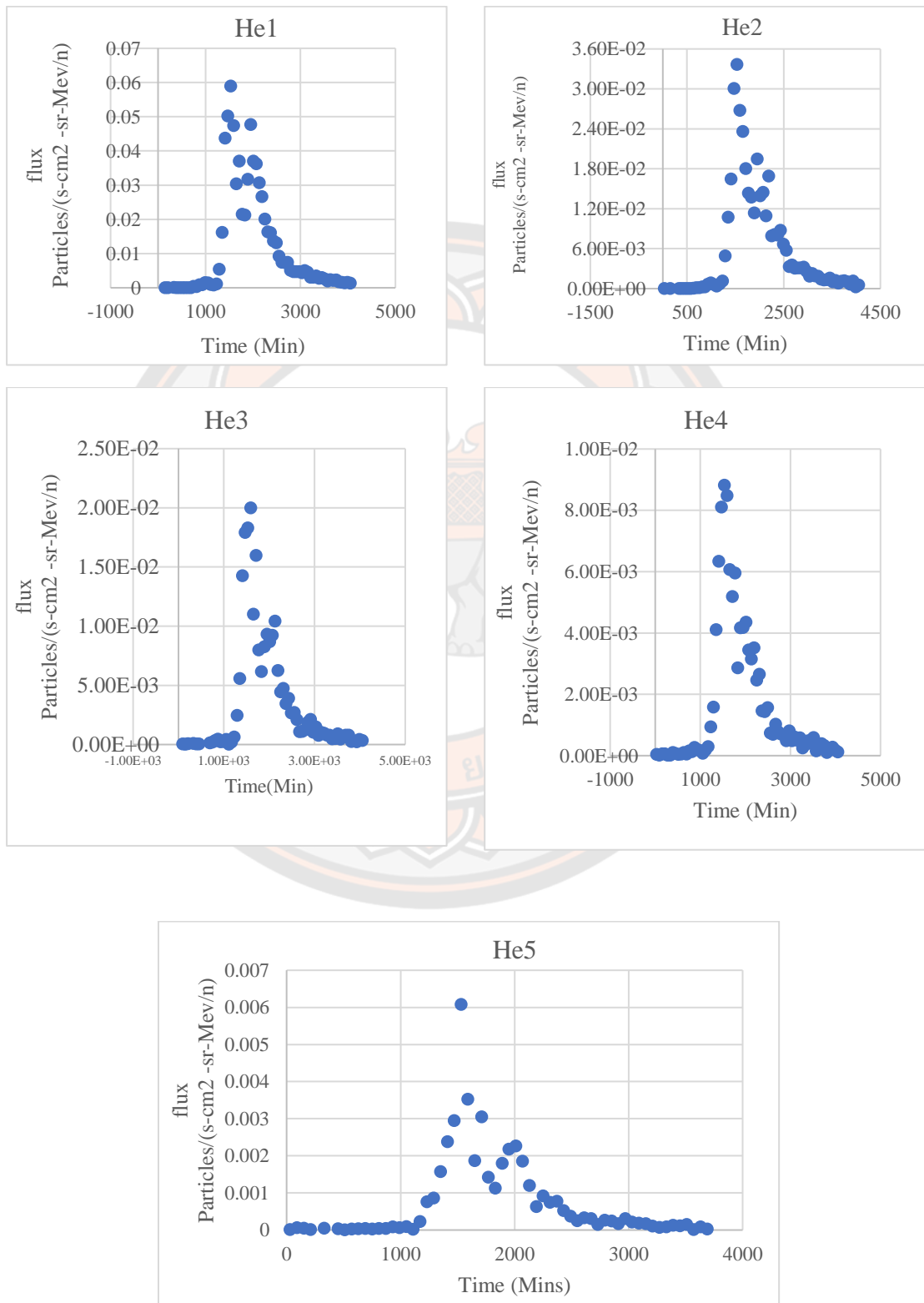
**APPENDIX E GRAPH TO CALCULATE BEST MEAN FREE PATH OF THE
ELEMENTS OF ALL ENERGY LEVELS OF 29 NOVEMBER
2020 EVENT**



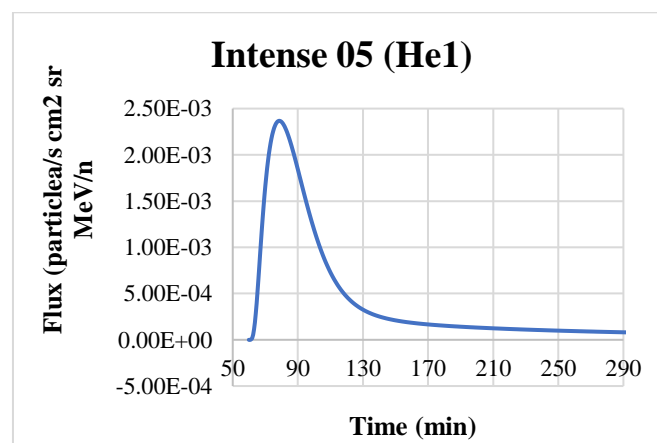
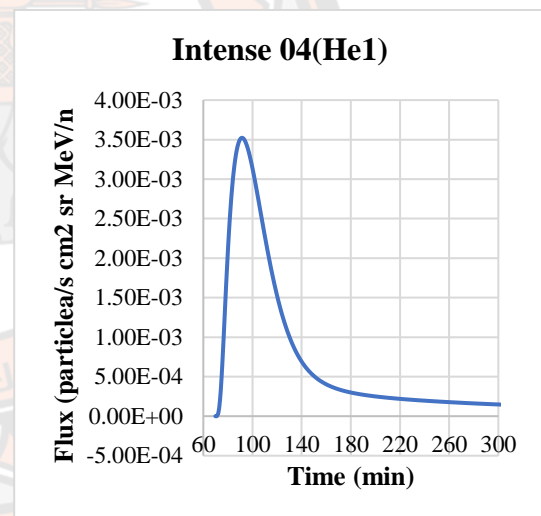
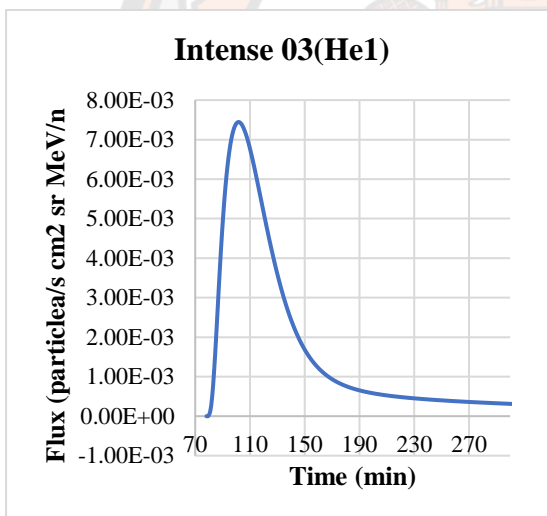
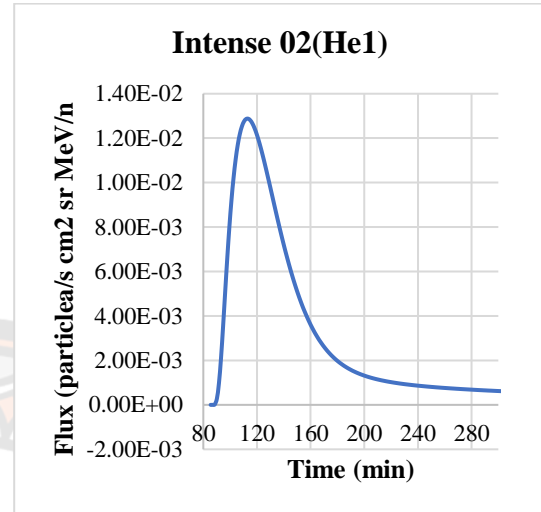
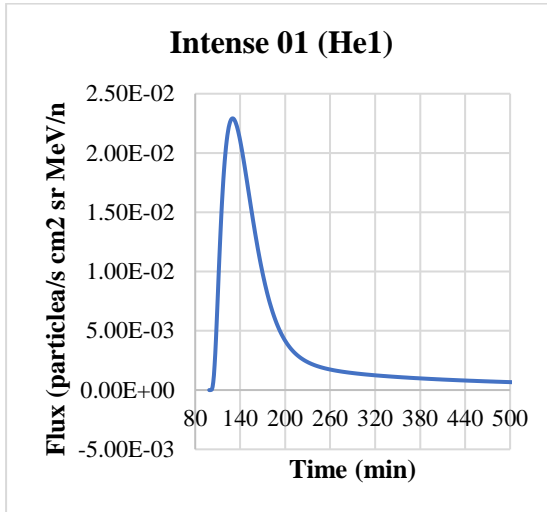
**APPENDIX F GRAPH TO CALCULATE INJECTION TIME USING FWHM
OF THE PARTICLES OF 29 NOVEMBER 20202 EVENT**

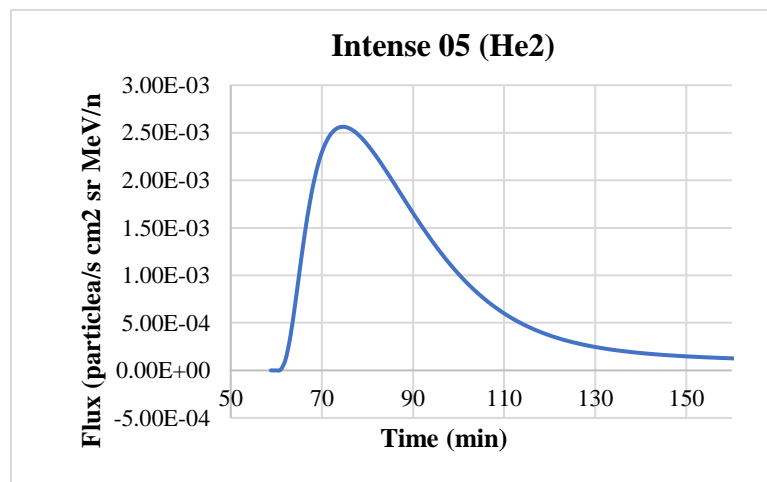
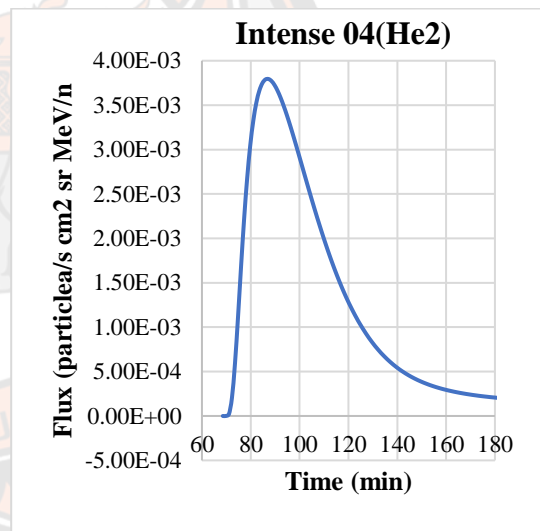
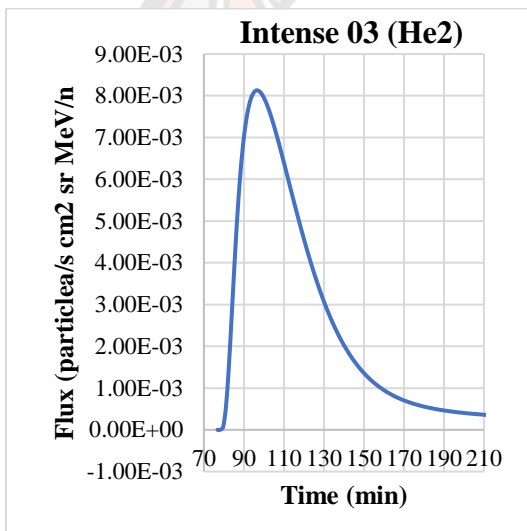
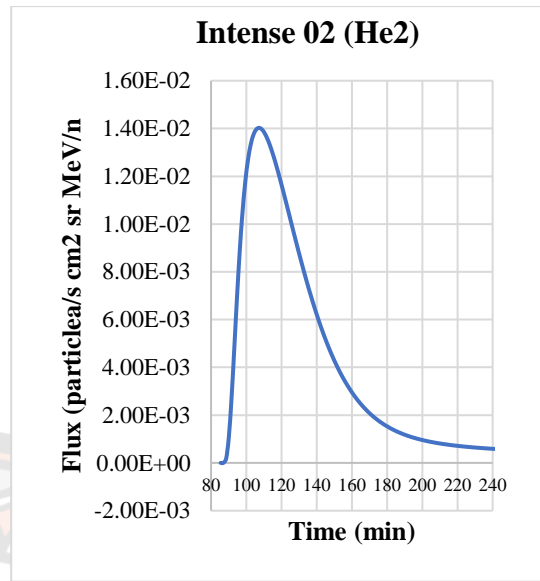
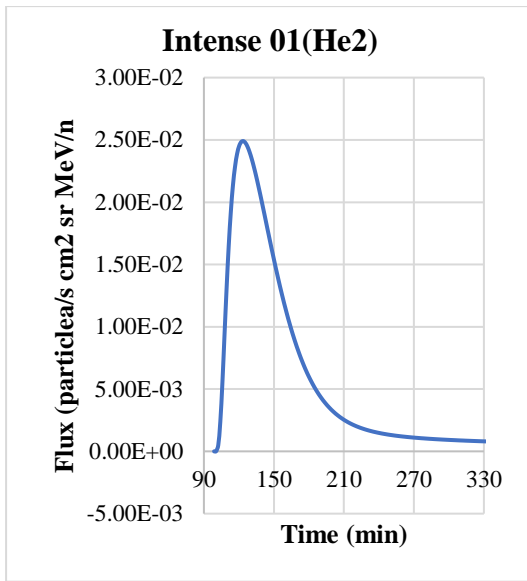


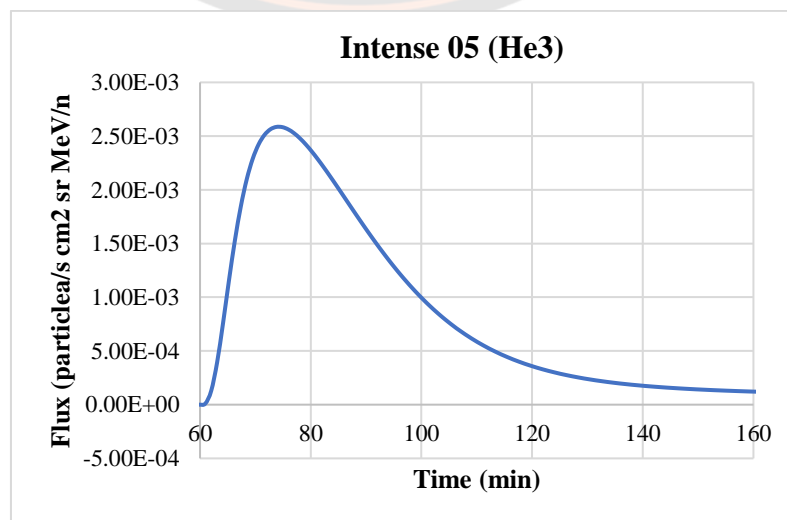
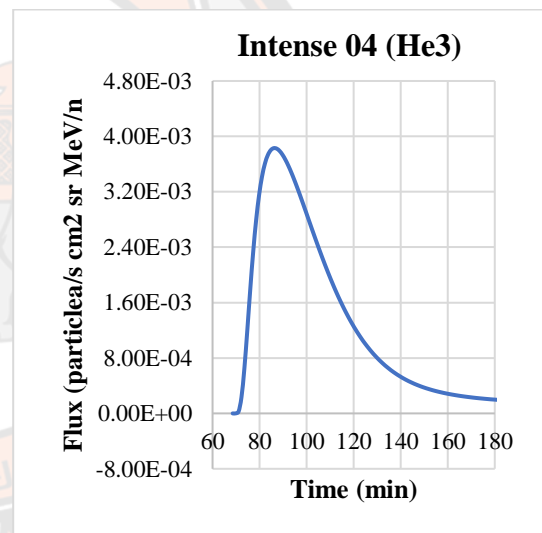
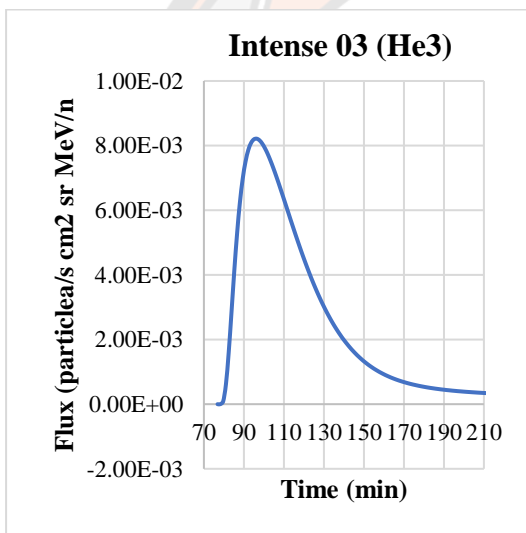
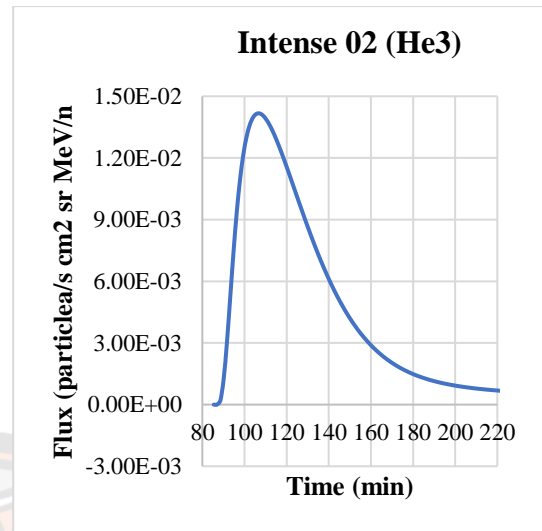
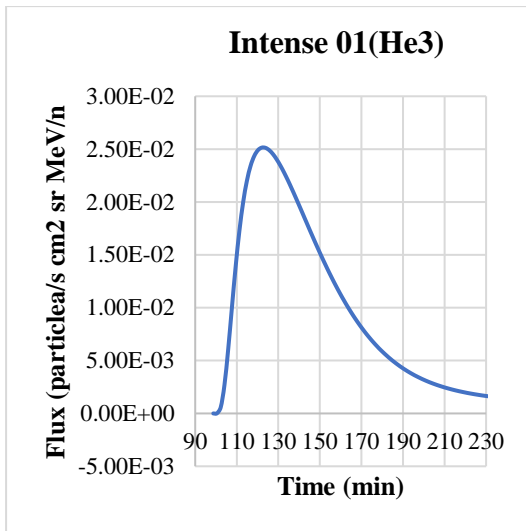
**APPENDIX G PARTICLE DENSITY AND TIME VALUE GRAPHS FOR THE
3 JULY 2021 EVENT FOR THE DATA COLLECTED FROM
THE SPACECRAFT**

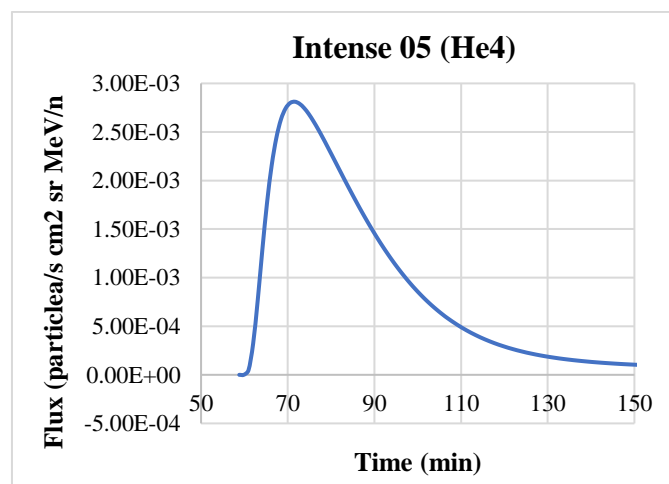
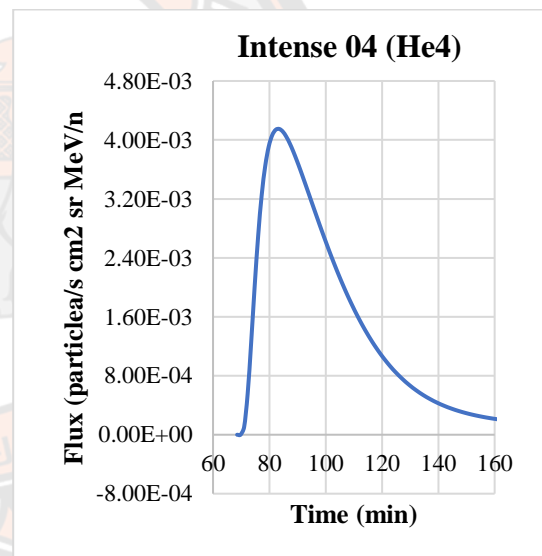
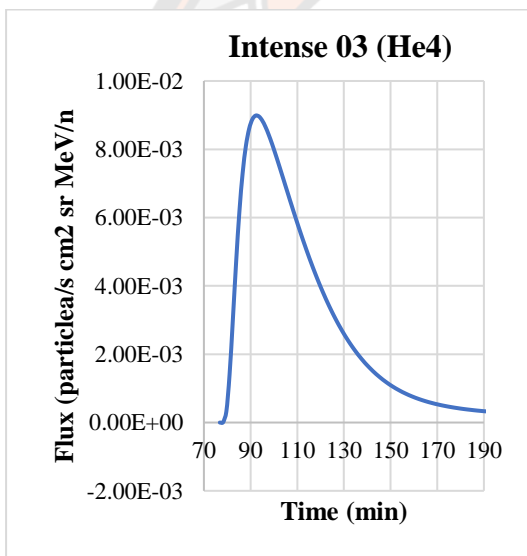
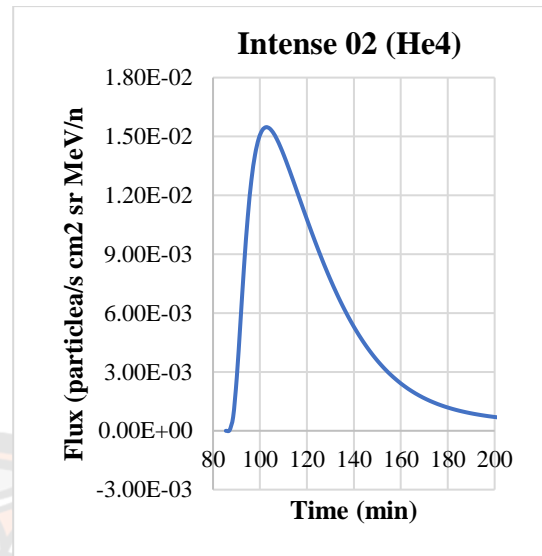
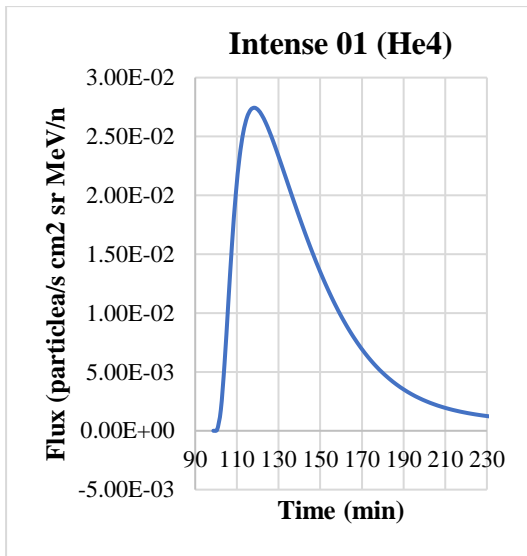


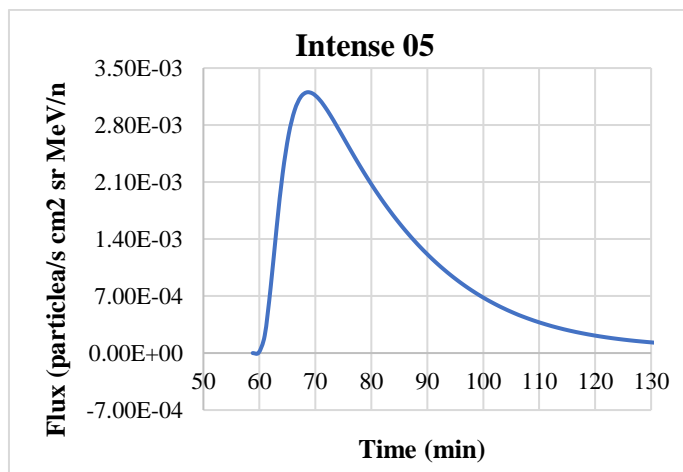
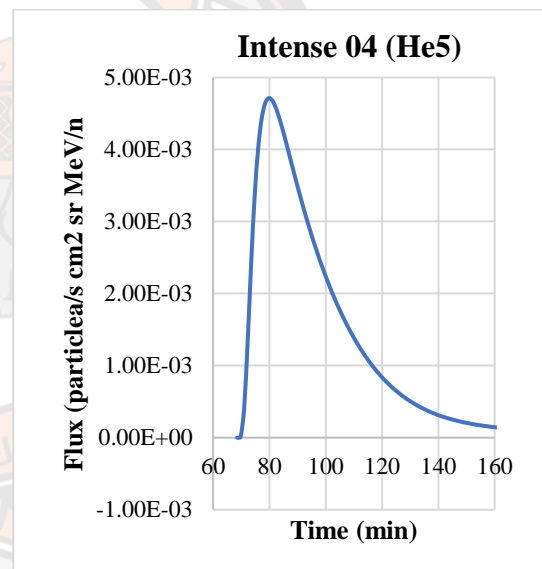
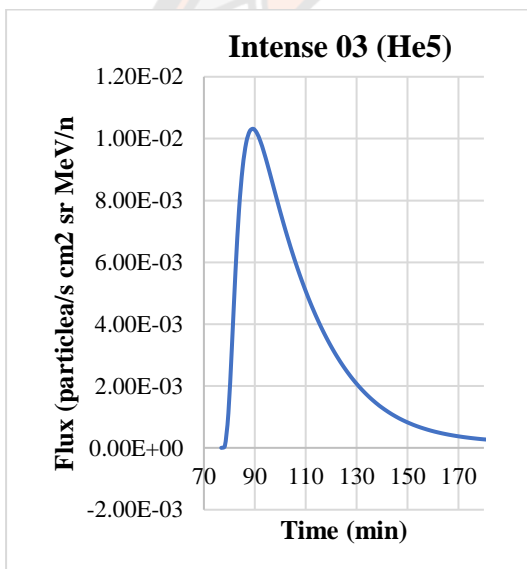
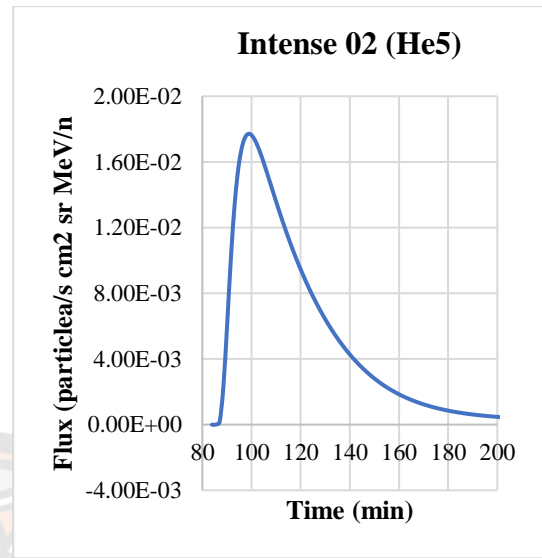
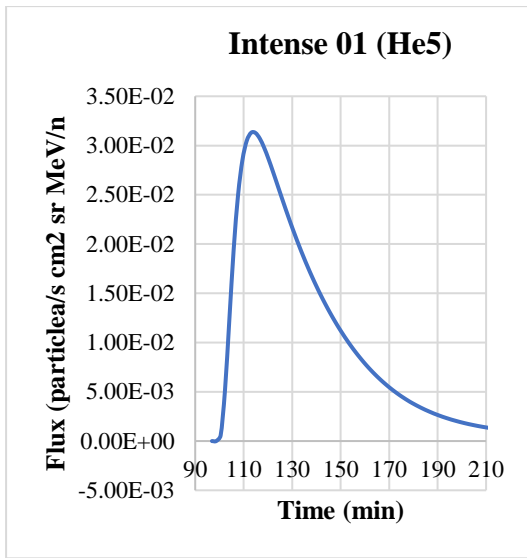
**APPENDIX H INTENSE GRAPH FROM THE SIMULATION OF THE DATA
OF 3 JULY 2021 EVENT**



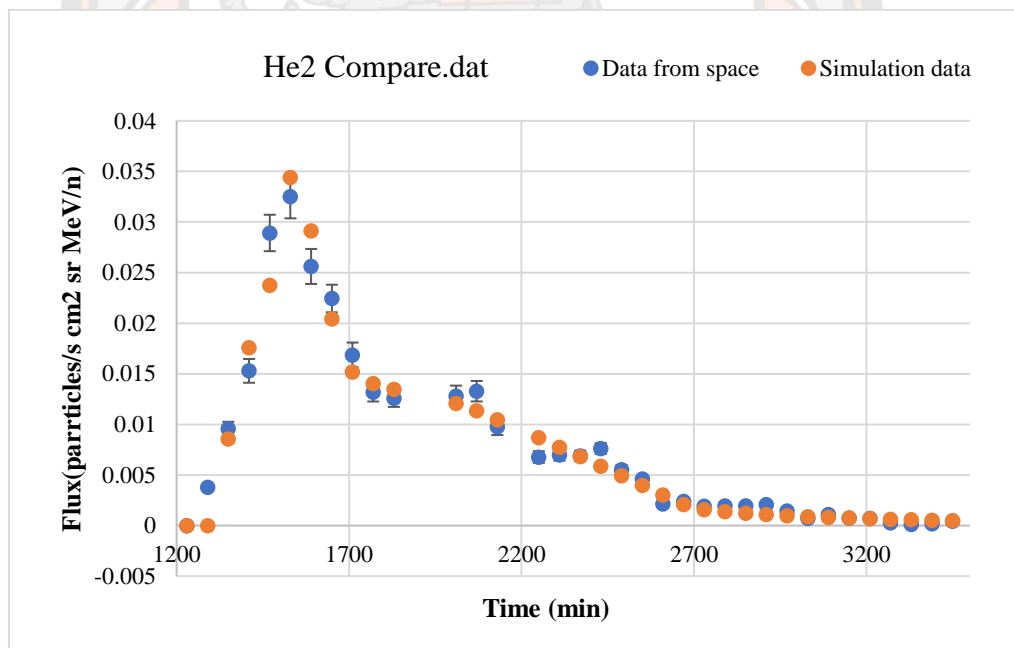
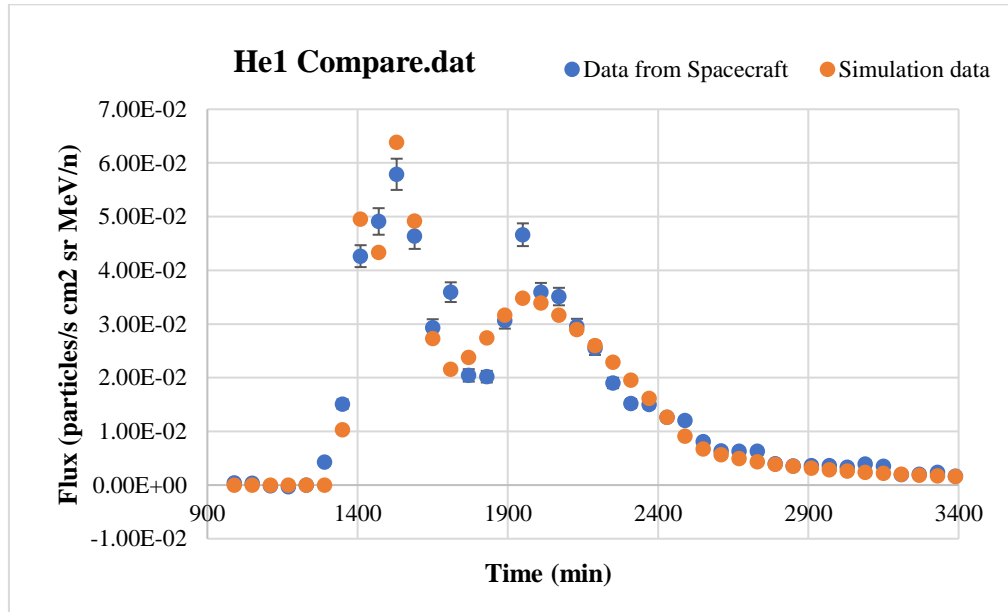


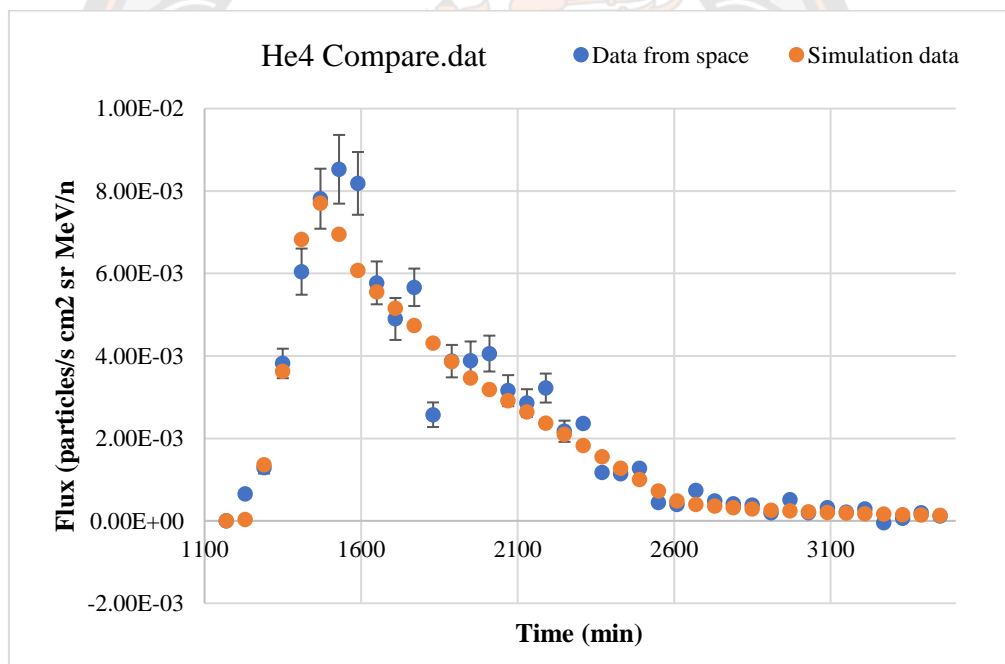
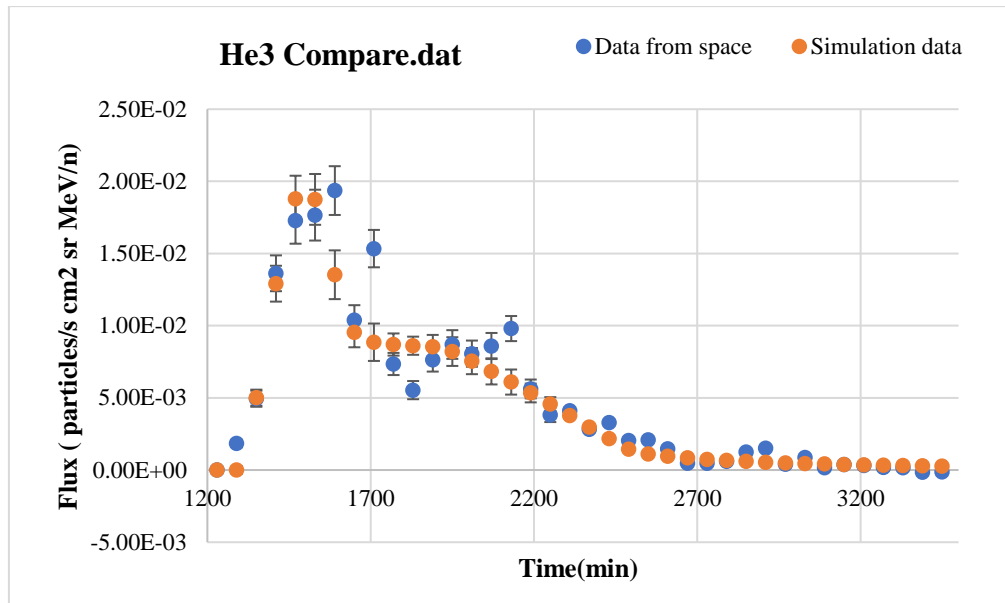


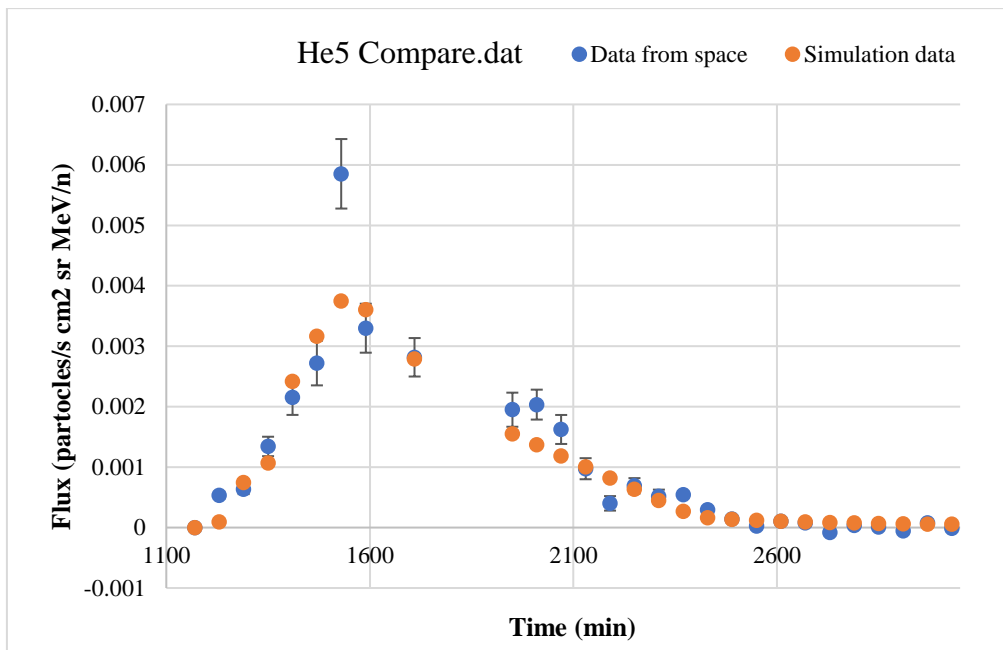




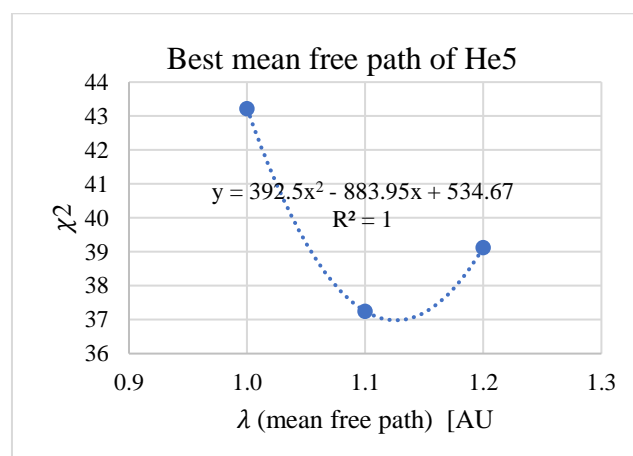
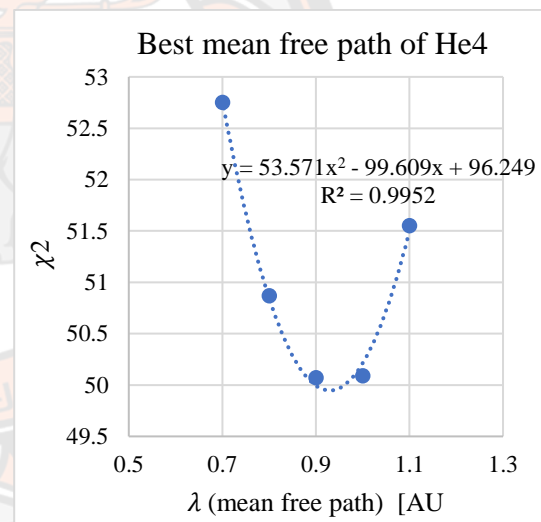
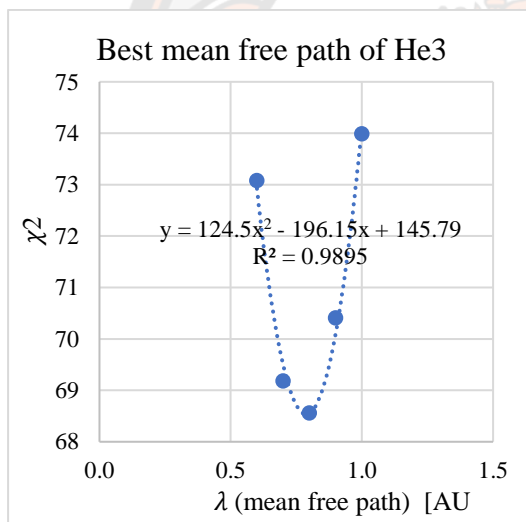
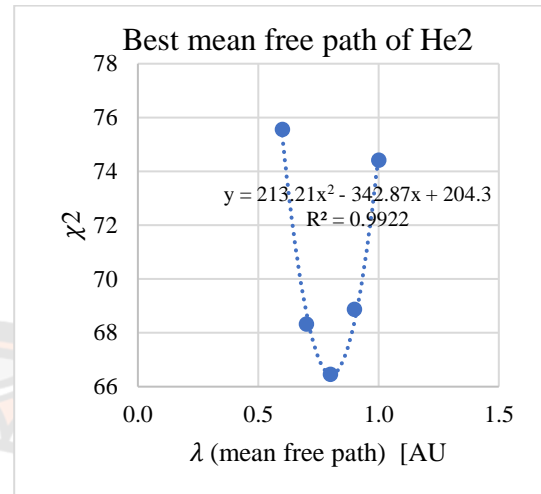
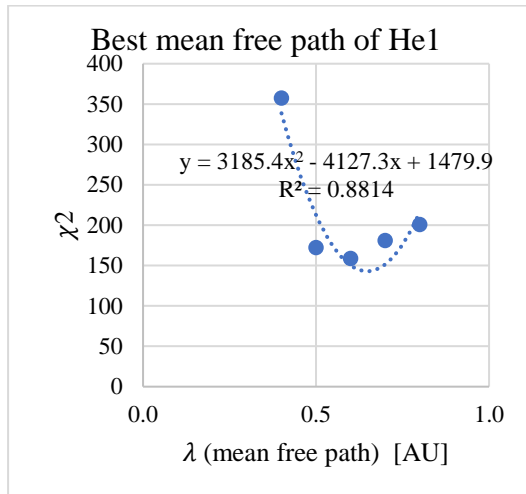
APPENDIX I COMPARE GRAPH FOR THE 3 JULY 2021 EVENT



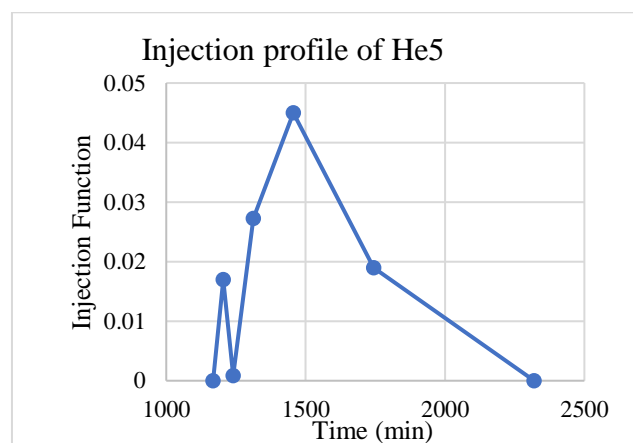
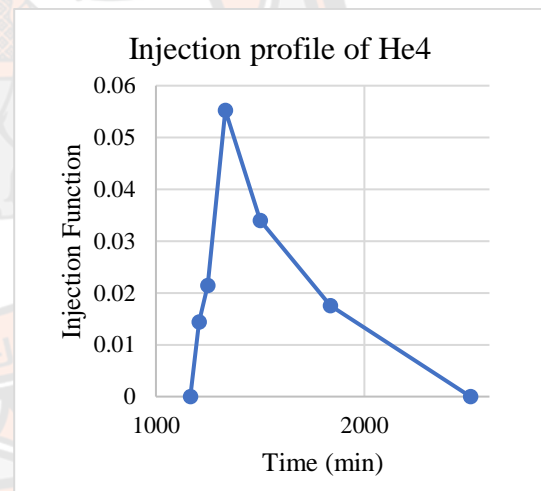
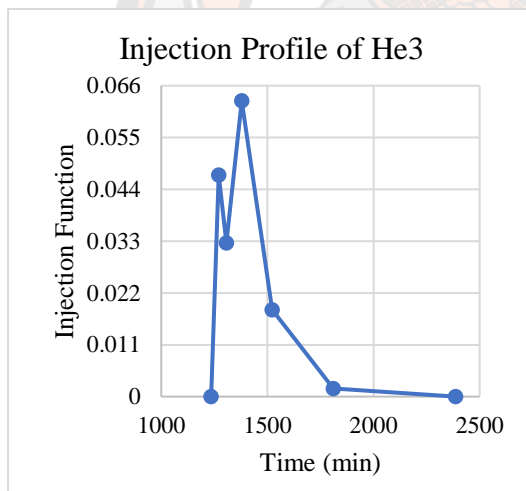
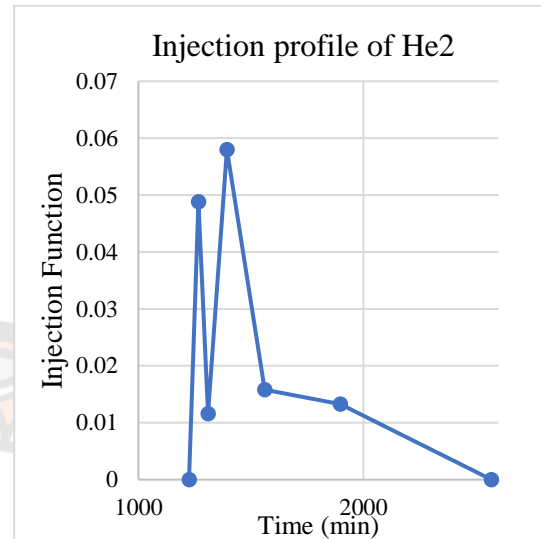
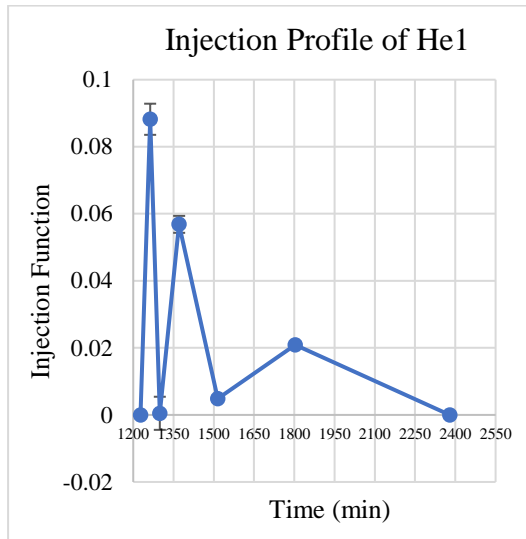




**APPENDIX J GRAPH TO CALCULATE BEST MEAN FREE PATH OF THE
ELEMENTS OF ALL ENERGY LEVELS 3 JULY 2021 EVENT**



**APPENDIX K GRAPH TO CALCULATE INJECTION TIME USING FWHM
OF THE PARTICLES OF 3 JULY 2021 EVENT**



BIOGRAPHY

Name-Surname Dechen Peldon

Date of Birth 7 February 1984

Address Teacher
Drukgyel Higher Secondary School
Paro
Bhutan

Current Workplace Drukgyel Higher Secondary School
Paro
Bhutan

Current Position student

Work Experience 12 years of teaching Physics in Higher Secondary school,
Bhutan

Education Background Bachelors in Education (Secondary) in Physics and
Mathematics

